Thesis concerning

Stimulated Raman Scattering in Silicon Coupled Photonic Crystal Microcavity Arrays

as part of the
Electrical Engineering and Information Technology
program at the
Universität Karlsruhe (TH)

submitted by
cand. el. Benedikt A. H. Stein
May 15, 2006

Supervisors:
Prof. Ulrich Lemmer, *Universität Karlsruhe (TH)*
Dr. Martina Gerken, *Universität Karlsruhe (TH)*
Prof. Jelena Vučković, *Stanford University*

Statutory Declaration

I hereby declare that this thesis is a result of my own work and that no other than the indicated references and resources have been used for its completion.

This work has not previously been submitted to any other examining authority and has not yet been published.

Karlsruhe, May 15, 2006

Benedikt Stein

Acknowledgements

First, I am most grateful to my supervisors, Professor Ulrich Lemmer and Dr. Martina Gerken at the *Universität Karlsruhe* as well as Professor Jelena Vučković at *Stanford University*. Uli and Martina have always supported me with patience and trust from Karlsruhe throughout my stay in the United States. Jelena has welcomed me with open arms and offered me the unique opportunity to participate in the cutting-edge work done at her group on the beautiful Stanford campus.

I am indebted to the *German National Academic Foundation*, the *Stiftung der Deutschen Wirtschaft* and again Jelena Vučković for generously funding my research and thus allowing me to expand my cultural and social horizons.

I express my gratitude to all the members of Stanford's *Nanoscale and Quantum Photonics Lab*. Here I would especially like to thank Ilya Fushman for his time as well as for his helpful advice and opinion which introduced me to the fascinating world of science.

My gratitude is moreover extended to Stanford's new *Bytes Café* which steadily provided me with the indispensable daily paper cup of freshly brewed coffee. For the effort they spend to collect and distribute knowledge all over the world I want to thank all the people who keep LaTeX-forums, *leo.org* and *wikipedia.org* growing and blooming.

Above all, I wish to thank my parents and my girlfriend Judith Rheinbay for their unconditional support and encouragement to pursue my studies in California.

Contents

1 Introduction **1**

2 Fundamentals **3**
2.1 Stimulated Raman Scattering on Silicon . . . 3
2.1.1 Raman Gain in Silicon . . . 3
2.1.2 Properties of Optical Microcavities . . . 5
2.1.3 Lasing Threshold in Optical Microcavities . . . 6
2.2 Photonic Crystals . . . 7
2.2.1 Maxwell's Equations in Periodic Dielectric Media . . . 7
2.2.2 Periodic Structures and the Bloch-Floquet-Formalism . . . 9
2.2.3 The Electromagnetic Variational Theorem . . . 9
2.2.4 Two-Dimensional Photonic Crystals . . . 11
2.3 Two-Dimensional Coupled Photonic Crystal Microcavity Arrays . . . 13
2.4 The Finite-Difference Time-Domain Method . . . 15
2.4.1 The Yee Algorithm . . . 16
2.4.2 Boundary Conditions . . . 18
2.4.3 Quality Factor Calculation . . . 20
2.4.4 Subcell Methods . . . 24

3 Preliminary considerations **25**
3.1 The Relative Modal Frequency Splitting . . . 25
3.2 Optical Setup for Possible Experimental Realization . . . 26

4 Relative Modal Frequency Splitting of the Dipole Modes in a Two-Dimensional CPCRA **29**
4.1 FDTD Simulation Setup . . . 29
4.2 Analysis of Different Parameters . . . 33
4.2.1 Shape of the Air Holes . . . 33
4.2.2 Thickness of the Inter-Cavity Barrier . . . 45
4.2.3 Radius of Circular Holes . . . 49
4.3 Results and Discussion . . . 52
4.3.1 Error Analysis . . . 52
4.3.2 Other Possible Parameters . . . 53

5 Analysis of a Two-Dimensional CPCRA Raman Laser Design **55**
5.1 Decision for one Basic Barrier Splitting . . . 55
5.2 Optimization of Eccentricity . . . 57
5.3 Cavity Quality Factors in a CPCRA Raman Laser . . . 60
5.3.1 Approximation of a CPCRA in a Finite Array . . . 61
5.3.2 Direct Calculation in a CPCRA Simulation with Periodic Boundary Conditions . . . 64
5.4 The Effective Modal Volume . . . 65
5.5 Influence of Free Carriers from Two-Photon Absorption . . . 66

5.6 Results and Discussion 67

6 Conclusions **69**

A FDTD Simulation Files **71**

A.1 Creation of the Structure Files 71
A.2 Three-dimensional Plotting of the Fabricated Structures 73
A.3 FDTD Time Evolution 74
A.4 Spectral Analysis of the Time Evolution Results 76
A.5 Filtering at Modes of Interest 77
A.6 Spatial Analysis of the Time Evolution Results 78

List of Figures

2.1 Simplified scheme of the first-order Stokes and Anti-Stokes scattering processes 3
2.2 Simplified scheme of the two competing processes in a Raman laser 4
2.3 Lorentzian intensity profile of a cavity mode centered at ω_0 6
2.4 Schematic depiction of photonic crystals possessing a periodicity of the dielectric material structure in one, two and three directions [25] 8
2.5 Introducing a periodicity in a one-dimensional photonic crystal (a) leads to a splitting of former degenerate bands (b, gray) into the upper air (red) and the lower dielectric band (green) and thus to the opening of a photonic bandgap (yellow) [27] 10
2.6 Visualization of the square lattice with circular holes, its unit cell and its Brillouin zone; Γ, X and M correspond to the wavevectors $\vec{k_{||}} = (0,0)$, $\vec{k_{||}} = \left(\frac{\pi}{a}, 0\right)$ and $\vec{k_{||}} = \left(\frac{\pi}{a}, \frac{\pi}{a}\right)$, respectively 12
2.7 Two band diagrams of different two-dimensional square lattices 13
2.8 Visualization of a CPCRA, its unit cell and its Brillouin zone; Γ, X and M correspond to the wavevectors $\vec{k_{||}} = (0,0)$, $\vec{k_{||}} = \left(\frac{\pi}{la}, 0\right)$ and $\vec{k_{||}} = \left(\frac{\pi}{la}, \frac{\pi}{la}\right)$, respectively 14
2.9 TE-mode band diagram and defect mode B_z-field patterns of a two dimensional coupled photonic crystal resonator array with a slab thickness of $\frac{d}{a} = 0.55$, an air hole radius of $\frac{r}{a} = 0.4$ in silicon with assumed $n_{Si} = 3.5$ and a number of $l = 3$ unit cell layers in each direction, calculated using the Finite-Difference Time-Domain method [16] 15
2.10 Yee cell containing the spatial positions and orientations of the $\vec{E}$ and $\vec{H}$ components 16
2.11 Energy decay of the x-dipole mode in the single cavity approximation of a CPCRA with $\frac{r_x}{a} = 0.4$ and $\frac{r_y}{a} = 0.3$ at $\frac{a}{\lambda} = 0.26842$ as used in chapter 5.3.1 21
2.12 Illustration of staircasing errors and the principle of a subcell method; the intensity of blue color defines the values of the analyzed refractive index distribution 23

3.1 Experimental setup proposed for the examination of a two-dimensional CPCRA Raman laser 26

4.1 Three dimensional plot of a photonic crystal slab with $l_x = 2$, $l_y = 3$, $a = 60\Delta$, $\frac{d}{a} = 0.65$ and elliptical holes with $\frac{r_x}{a} = 0.25$ and $\frac{r_y}{a} = 0.4$ 30
4.2 *vtk* plots of two lattices of different ellipsis-approximations and a real elliptical lattice, all written with $a = 60\Delta$ and $l_x = l_y = 3$ 34
4.3 Normalized frequencies and relative modal splitting of the x- and y- dipoles versus the eccentricity in a CPCRA with $l_x = l_y = 3$ 35
4.4 Spectra of a CPCRA with $l_x = 3$, $l_y = 3$, $\frac{r_x}{a} = 0.25$ and $\frac{r_y}{a} = 0.45$; note that the difference in frequency of the peaks in (a) compared to (b) and (c) is due to different lengths T of the time evolutions 37
4.5 Visualization of the terminology preferred by the author: we arbitrarily choose a two-dimensional Cartesian coordinate system of x- and y-directions; the values l_x and l_y describe the numbers of unit cell layers of thickness a in each direction; the parameters $\frac{r_x}{a}$ and $\frac{r_y}{a}$ correspond to the two semiaxes of the elliptical holes 38
4.6 Normalized frequencies and relative modal splitting of the x- and y- dipoles versus the length of the semimajor axis $\frac{r_y}{a}$ in a CPCRA with $\frac{r_x}{a} = 0.25$ and a symmetric arrangement of the cavities, i.e., $l_x = l_y$ 39

4.7 B_z-fields of the dipole modes for $l_x = l_y = 3$, $\frac{r_x}{a} = 0.25$ and $\frac{r_y}{a} = 0.4$ in normalized units at the center of the photonic crystal slab . . . 40
4.8 Normalized frequencies and relative modal splitting of the x- and y- dipoles versus the length of the semimajor axis $\frac{r_y}{a}$ in a CPCRA with $\frac{r_x}{a} = 0.25$ and asymmetric arrangements of the cavities, i.e., $l_x \neq l_y$ . . . 41
4.9 Visualization of the square lattice with elliptical holes, its unit cell and the extended irreducible Brillouin zone due to a reduction from four-fold to two-fold rotational symmetry; Γ, X, Y and M correspond to the wavevectors $\vec{k_{||}} = (0,0)$, $\vec{k_{||}} = \left(\frac{\pi}{a}, 0\right)$, $\vec{k_{||}} = \left(0, \frac{\pi}{a}\right)$ and $\vec{k_{||}} = \left(\frac{\pi}{a}, \frac{\pi}{a}\right)$, respectively . . . 42
4.10 Upper (+) and lower (-) bandedges at the X and M point and the Y and M point, respectively, with the resulting bandgaps in the different directions. Here we used $\frac{r_x}{a} = 0.25$, $\frac{r_y}{a}$ varies from $\frac{r_y}{a} = 0.25$ to its maximum value of $\frac{r_y}{a} = 0.45$ . . . 43
4.11 Upper (+) and lower (-) bandedges at the X and M point and the Y and M point, respectively, with the resulting bandgaps in the different directions. While the bandgaps are plotted for each different value $\frac{r_x}{a}$, inside each plot $\frac{r_y}{a}$ varies from the specific $\frac{r_y}{a} = \frac{r_x}{a}$ to its maximum value of $\frac{r_y}{a} = 0.45$ . . . 44
4.12 Normalized frequencies and relative modal splitting of the x- and y- dipoles versus the length of the unit cell in y-direction l_y in a CPCRA with $\frac{r_x}{a} = 0.25$ and $l_x = 2$ . . . 45
4.13 B_z-fields of the y-dipole modes for $\frac{r_x}{a} = \frac{r_y}{a} = 0.25$, $l_x = 2$ and varying l_y in normalized units at the center of the photonic crystal slab . . . 46
4.14 B_z and $|\vec{E}|^2$ of the x-dipole modes for $\frac{r_x}{a} = \frac{r_y}{a} = 0.25$, $l_x = 2$ and varying l_y in normalized units at the center of the photonic crystal slab . . . 47
4.15 Normalized frequencies and relative modal splitting of the x- and y- dipoles versus the length of the unit cell in y-direction l_y in a CPCRA with $\frac{r_x}{a} = 0.25$ and a constant l_x . . . 48
4.16 Normalized frequencies of the x- and y- dipoles versus the radius of the circular holes $\frac{r}{a}$ in a CPCRA with asymmetric arrangements of the cavities, i.e., $l_x \neq l_y$ . . . 50
4.17 Relative modal splitting m of the x- and y- dipoles versus the radius of the circular holes $\frac{r}{a}$ in a CPCRA with asymmetric arrangements of the cavities, i.e., $l_x \neq l_y$ . . . 51
4.18 Upper (+) and lower (-) bandedges at the X and M point with the resulting full bandgap versus varying $\frac{r}{a}$ for the underlying square lattice . . . 51

5.1 Spectra of CPCRAs with $l_x = 2$ and y-dipole excitation; $\frac{r}{a}$ is chosen as $\frac{r}{a} = 0.35$ due to m values closest to the range of desired relative modal splitting (see figure 4.17) . . . 55
5.2 Spectra and B_z-fields of a CPCRA with $l_x = 3$ and $l_y = 4$; $\frac{r}{a}$ is this time chosen as $\frac{r}{a} = 0.30$ due to m values closest to the range of desired relative modal splitting (see figure 4.17) . . . 56
5.3 Optimization of the hole eccentricity in a CPCRA with $(l_x; l_y) = (3; 4)$ . . . 57
5.4 Detailed spectrum of a CPCRA with $l_x = 3$, $l_y = 4$, $\frac{r_x}{a} = 0.4$, $\frac{r_y}{a} = 0.3$ and a time evolution period of $T = 18022$ timesteps . . . 58
5.5 B_z fields of the y-dipole for $\frac{r_x}{a} = 0.4$, $\frac{r_y}{a} = 0.3$ and varying filter depth . . . 59
5.6 Band diagram of a square lattice with $\frac{r_x}{a} = 0.4$ and $\frac{r_y}{a} = 0.3$ along the high symmetry axes of the crystal . . . 60
5.7 Visualization of two finite two-dimensional CPCRA structures with $l_x = 3$, $l_y = 4$, $\frac{r_x}{a} = 0.4$ and $\frac{r_y}{a} = 0.3$ which we used for the approximation of larger arrays . . . 61
5.8 Spectra and B_z-fields of the x- and y-dipole modes in the single-cavity approximation of a CPCRA with $l_x = 3$, $l_y = 4$, $\frac{r_x}{a} = 0.4$ and $\frac{r_y}{a} = 0.3$ . . . 62
5.9 Spectra and B_z-fields of the x-dipole mode in the single-cavity approximation of a CPCRA with $l_x = 3$, $l_y = 4$, $\frac{r_x}{a} = 0.4$ and $\frac{r_y}{a} = 0.3$ . . . 62
5.10 Spectra and B_z-fields of the y-dipole mode in the single-cavity approximation of a CPCRA with $l_x = 3$, $l_y = 4$, $\frac{r_x}{a} = 0.4$ and $\frac{r_y}{a} = 0.3$ . . . 63

5.11 Quality factor calculation by measurement of the spectral FWHM of the modes of interest . . 64

" Μη μου τους κύκλους τάραττε! "
"Do not disturb my circles!", *Archimedes*, 212 B.C. [1]

[1] Uttered by the Greek mathematician and philosopher *Archimedes of Syracuse* to a Roman soldier who, despite being given orders not to, killed him at the conquest of Syracuse [1]

1 Introduction

Increasing needs for low cost production and on-chip integration has made silicon being considered one of the most promising materials for nanophotonic devices. Passive silicon devices such as submicron SOI waveguides, bends, splitters and filters have as well been developed as integrated silicon optical modulators which use two-photon absorption or the thermo-optic effect [2].

As the indirect bandgap of silicon complicates the development of electronically pumped band-to-band electron-hole combination radiation lasers, an all-silicon laser has been demonstrated recently [3] using the effect of stimulated Raman scattering as optical gain technique to achieve the integration of active optical devices. The Raman gain in silicon is approximately 10^4 times larger in silicon than in silica glass, which allows us to have significant amplification at low threshold powers. As a Raman laser is based on a phonon scattering process, usually another pump laser is necessary as pump source, which causes Raman lasers to be especially applicable as wavelength extension of existing lasers and for wavelength-selectable signal amplification.

Most progress in the field of stimulated Raman scattering on silicon has been achieved in submicron SOI waveguide structures [3, 4, 5, 6, 7, 8, 9, 10]. However, the lasing threshold in such waveguides is significantly increased by the process of two-photon absorption and subsequent free carrier absorption [11]. This issue is addressed either using pulsed operation or integration of p-i-n diodes. In the latter case the lifetime of the free carriers is reduced by application of a reverse bias orthogonal to the waveguide structure. Another approach to significantly reduce the free carrier lifetime is the exploitation of Raman scattering in materials with fast surface recombination velocities such as silicon photonic crystal waveguide structures [12].

Photonic crystals, in analogy to a semiconductor crystal, possess a band structure for photons, i.e., photons of special energy and momentum quantum mechanically cannot exist inside the photonic crystal structure. By introduction of crystal defects we can create photonic defect states inside this bandgap which allow the design of extremely lossless resonators. These so called photonic crystal microcavities, likewise microtoroid or microsphere silica cavities [13, 14], can also be used for the implementation of stimulated Raman scattering as proposed in [15]. The lasing threshold of a Raman laser is proportional to the inverse of the quality factors for each, the pump and the lasing mode. This implies that photonic crystal microcavity resonators with high quality factors offer the possibility for the design of ultra low threshold Raman lasers. However, an experimental realization of an all silicon Raman laser in a photonic crystal microcavity has not been achieved, yet.

In this thesis, we want to introduce a new and different structure for the implementation of stimulated Raman scattering on silicon, the so called two-dimensional coupled photonic crystal resonator arrays [16, 17, 18]. Those structures consist of a two-dimensional matrix of coupled photonic crystal microcavities. The coupled resonators possibly allow, for sufficient overall quality factors, lasing at significantly increased output powers compared to the relatively weak output powers of single microcavities. An InP laser in a 100×100-cavity array has been demonstrated recently [19].

In chaper 2 we first discuss fundamentals which are necessary for the understanding of the design process of a 2D coupled photonic crystal microcavity array Raman laser. In detail, we examine the properties of stimulated Raman scattering in optical microcavities, photonic crystals, coupled photonic crystal microcavity arrays and the numerical Finite-Difference Time-Domain simulation method.

Chapter 3 presents some preliminary considerations regarding the design goal and the later experimental realization.

The following chapter 4 discusses the design process itself. After the applied FDTD simulation setup is introduced, the design focuses on the influence of different parameters on the properties of the x- and y-dipole modes in a resonator array. The achieved results are subsequently interpreted, analyzed and summarized.

The analysis of the properties of a Raman laser design is given in chapter 5. After focusing on one distinct laser design we calculate the mode quality factors, the effective modal volume and ultimately an estimate for possible lasing thresholds of an array laser.

Finally, chapter 6 summarizes the achieved results, while in the appendix A a selection of the utilized computational scripts is attached.

2 Fundamentals

An all-silicon Raman laser realized in coupled photonic crystal resonator arrays bases on complicated interactions of different processes and concepts. We therefore want to have a preliminary summary of the fundamentals of the involved topics of stimulated Raman scattering in silicon in section 2.1, photonic crystals in section 2.2 and two-dimensional coupled photonic crystal microcavity arrays in section 2.3. Finally we will conclude the chapter with the necessary principles of the finite-difference time-domain method, the computational simulation method which is used for most of the analysis this thesis deals with.

2.1 Stimulated Raman Scattering on Silicon

The indirect bandgap of silicon had made the development of integrated silicon lasers seem to be improbable for long. Enhanced nonlinear properties and especially Raman scattering in microstructures offer us the possibility to bypass the electronic band structure limitation of silicon. Therefore a short introduction to the properties of stimulated Raman scattering in silicon should be given in this chapter.

2.1.1 Raman Gain in Silicon

Raman Scattering

Although *Raman scattering* is referred to as a third order nonlinearity, it belongs to a class of third-order nonlinearities which is no longer easily describable by means of a third-order susceptibility $\chi^{(3)}$ because it is based on more complicated interactions, but nevertheless proportional to a triple product of the electric field. The subsequent analysis primarily follows the one given by [20] and extended in [21].

There are basically two types of Raman scattering events which are depicted in figure 2.1. In the first and most important case referred to as *First-order Stokes scattering* (figure 2.1(a)) an incident photon of the frequency ω_l is absorbed, yielding the emission of a phonon at frequency ω_ν and a Stokes photon of the difference-frequency $\omega_s = \omega_l - \omega_\nu$.

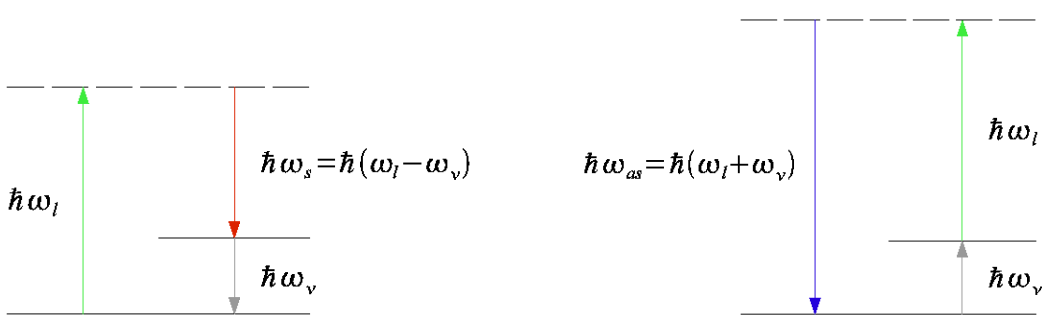

(a) Stokes scattering (b) Anti-Stokes scattering

Figure 2.1: Simplified scheme of the first-order Stokes and Anti-Stokes scattering processes

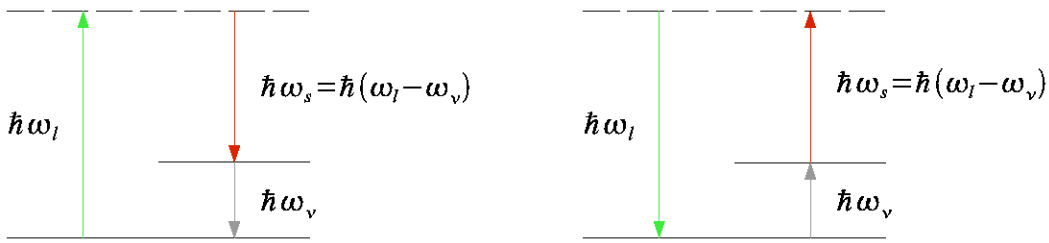

(a) Stokes scattering (b) Inverse Stokes scattering

Figure 2.2: Simplified scheme of the two competing processes in a Raman laser

The other possible scattering process is called *First-order Anti-Stokes scattering* and consists of an incident photon of the frequency ω_l absorbed of a system which is already in the vibrational state of ω_ν, yielding the emission of an Anti-Stokes photon of the higher frequency $\omega_{as} = \omega_l + \omega_\nu$ (figure 2.1(b)). However, as initial excitation is a necessary condition for Anti-Stokes emission, this process is much less probable. Applying the Boltzmann distribution yields an intensity relation of

$$\frac{I_{as}}{I_s} \approx 8\% \tag{2.1}$$

As we are finally aiming at Raman lasing, we wish to achieve the highest possible output and lowest possible lasing threshold powers. Therefore we will subsequently focus on the Stokes beam ω_s as the lasing mode, while using ω_l as the initial pump mode frequency.

For the calculation of a lasing threshold for stimulated Stokes scattering, it is also important to take into account the influences of *inverse Stokes scattering*, which is basically Anti-Stokes scattering with the actual Stokes frequency as its pump mode. This process together with again a scheme of the Stokes scattering process is depicted in figure 2.2.

Quantum Mechanical Derivation of the Raman Gain for the Stokes Beam

To quantitatively describe the Raman gain process, we should start with a quantum mechanical description of the above mentioned scattering processes. As Stokes and inverse Stokes scattering lead to either sum-frequency generation or difference-frequency generation, we can also model these processes as $\chi^{(2)}$ interactions. Taking the term of the interaction Hamiltonian given in [20] which gives rise to Stokes scattering and assuming an electric field composed of the two frequencies ω_l and ω_s results in the Stokes emission rate

$$W_{Stokes} \propto \left|\langle n_l - 1, n_s + 1, 1 | a_\nu^\dagger a_s^\dagger a_l | n_l, n_s, 0\rangle\right|^2 = n_l\,(n_s + 1) \tag{2.2}$$

and the inverse Stokes rate

$$W_{Stokes^{-1}} \propto \left|\langle n_l + 1, n_s - 1, 0 | a_l^\dagger a_\nu a_s | n_l, n_s, 1\rangle\right|^2 = n_s\,(n_l + 1)\,. \tag{2.3}$$

Here $a_{s,l,\nu}^\dagger$ and $a_{s,l,\nu}$ are the phonon (ν), Stokes photon (s) and pump photon (l) creation and annihilation operators, respectively, while the vector $|n_l, n_s, i\rangle$ describes a system in a state with n_l photons at pump frequency, n_s photons at Stokes frequency and i phonons in the vibrational mode [20].

Introducing the probabilities of the system to be initially in the ground vibrational state, P_g, or to be in the excited vibrational state, P_e, leads to the rate equation for photons in the Stokes mode,

$$\frac{dn_s}{dt} = D\,(P_g - P_e)\,n_l n_s + D\,(P_g n_s - P_e n_s)\,, \tag{2.4}$$

where D is a yet to be determined constant. Now by considering the case of *stimulated Raman scattering*, $\langle n_s \rangle >> 1$, we achieve the approximation

$$\frac{dn_s}{dt} \approx D\left(P_g - P_e\right) n_l n_s. \tag{2.5}$$

Expressing the number of Stokes photons for a laser beam propagating along the path r finally yields

$$\frac{dn_s}{dr} = \frac{dn_s}{dt}\frac{dt}{dr} = \frac{D\left(P_g - P_e\right) n_l}{\frac{dr}{dt}} n_s = \gamma_s n_s = g_s I_l n_s \tag{2.6}$$

or in terms of the accumulated Stokes-intensity:

$$I_s(r) = I_s(0) e^{\gamma_s r} = I_s(0) e^{g_s I_l r} \tag{2.7}$$

This expression introduces the important gain factors γ_s, which describes the *Raman gain per interaction length*, and g_s, which quantifies the *gain per incident pump intensity and interaction length*.

In principle the Raman gain for bulk silicon needs to be calculated using the Raman tensor $\bar{g}$ which leads to a value of the Raman gain factor depending on the polarization of both the pump and the Stokes modes with respect to the silicon crystal lattice. However, this calculation for bulk silicon would yield a different g_s-value at each spatial position. Instead, comparing references [4, 8, 22] which observed gain factors in a range of

$$g_s \in \left[20\frac{cm}{GW}; 76\frac{cm}{GW}\right], \tag{2.8}$$

we rather choose $g_s \approx 50\frac{cm}{GW}$ as a conservative averaged estimate for the later calculation of the Raman lasing threshold in coupled photonic crystal resonator arrays.

2.1.2 Properties of Optical Microcavities

As indicated above, the interaction between matter and light can be dramatically increased by the use of electromagnetic resonators operating at optical wavelengths. The modal confinement in these optical microcavities is characterized either in time or in space.

Temporal confinement of a mode at frequency ω_0 is determined by the loss rate of the cavity. Therefore the cavity's modal *quality factor* Q is defined in terms of the energy U stored inside and the power P dissipating from the cavity at a center frequency ω_0 as [23, 24]

$$Q = \omega_0 \frac{U}{P}. \tag{2.9}$$

Taking into account that the power dissipating is the negative of the time rate of energy stored in the resonator we find that

$$\frac{dU}{dt} = -P = -\omega_0 \frac{U}{Q} \tag{2.10}$$

and thus

$$U(t) = U_0 e^{-\frac{\omega_0 t}{Q}}. \tag{2.11}$$

The time dependence of the stored energy implies that oscillations of the field inside the resonator are damped as follows:

$$E(t) = E_0 e^{-\frac{\omega_0 t}{2Q}} e^{i(\omega_0 + \delta\omega)t} \tag{2.12}$$

Assuming that the resonant frequency does not change in presence of the losses, i.e., $\delta\omega \approx 0$, and transforming the time dependent field into frequency space we obtain:

$$E(t) = E_0 e^{-\frac{\omega_0 t}{2Q}} e^{i\omega_0 t} \circ\!\!-\!\!\bullet E(\omega) = E_0 \frac{1}{-i(\omega - \omega_0) + \frac{\omega_0}{2Q}} \tag{2.13}$$

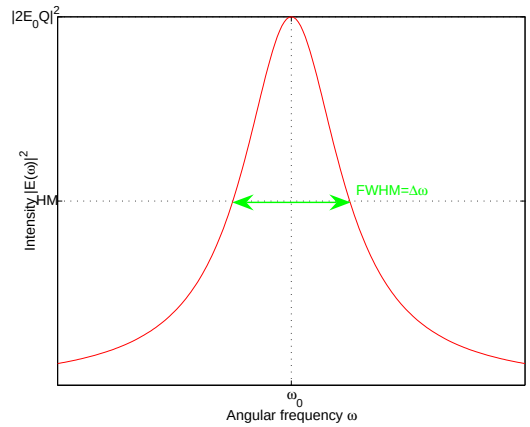

Figure 2.3: Lorentzian intensity profile of a cavity mode centered at ω_0

Therefore an exponentially as $e^{-\frac{\omega_0 t}{2Q}}$ decaying field at the frequency ω_0 has a frequency spectrum of Lorentzian intensity shape centered at ω_0 with the FWHM of $\Delta\omega = \frac{\omega_0}{Q}$, which leads to another expression of the quality factor:

$$Q = \frac{\omega_0}{\Delta\omega} \tag{2.14}$$

This expression can also be interpreted in terms of the Photon lifetime inside the cavity τ_{ph} and the optical period T as:

$$Q = 2\pi \frac{\tau_{ph}}{T} \tag{2.15}$$

To describe the spatial confinement of our field, we moreover need to define its effective volume with respect to the spatial distribution of the dielectric constant $\epsilon(\vec{r})$. This leads to the definition of the *cavity mode volume*:

$$V = \frac{\iiint \epsilon(\vec{r}) \left| E(\vec{r}) \right|^2 d^3\vec{r}}{max\left[\epsilon(\vec{r}) E(\vec{r})\right]} \tag{2.16}$$

2.1.3 Lasing Threshold in Optical Microcavities

High quality factors and small mode volumes in optical microcavities offer the possibility to decrease the lasing threshold in the cavity by several orders of magnitude. Where for spontaneous emission enhancement the figure of merit is the $\frac{Q}{V}$ ratio, for SRS we derive $P_{threshold} \propto \frac{V}{Q^2}$ [24, 13, 15]:

The *effective interaction length* L_{eff} inside a microcavity is given by

$$L_{eff} = \tau_p \frac{c_0}{n_c} = \frac{Q_p}{\omega_p} \frac{c_0}{n_c} = \frac{Q_p \lambda_p}{2\pi n_c} \tag{2.17}$$

where $\tau_p = \frac{Q_p}{\omega_p}$ is the pump photon lifetime with the pump quality factor Q_p and the angular pump frequency ω_p, c_0 is the vacuum speed of light and n_c is the refractive index of the cavity. Without a cavity, the interaction length of vertically incident pump photons with the Raman gain medium is approximately equal to the thickness of the photonic crystal slab:

$$L_0 = d \tag{2.18}$$

The buildup of the pump mode intensity inside the cavity can therefore be described as

$$I_c = I_p \frac{L_{eff}}{L_0} = I_p \frac{Q_p \lambda_p}{2\pi n_c d} = \frac{P_p}{A} \frac{Q_p \lambda_p}{2\pi n_c d} = P_p \frac{Q_p \lambda_p}{2\pi n_c V_m} \tag{2.19}$$

where $I_p = \frac{P_p}{A}$ is the incident pump intensity composed of the incident pump power P_p and the cavity in-plane area A, and $V_m \approx A \cdot d$ is the effective modal volume.

The intensity increase of the Stokes beam is directly coupled to the pump intensity and can therefore be written as a function of time:

$$I_s(t) = I_s(0) e^{g_s \xi I_c r} = I_s(0) e^{g_s \xi I_c \frac{c_0}{n_c} t} \tag{2.20}$$

Here I_s is the intensity of the Stokes beam, g_s the Raman gain coefficient, r the interaction length and ξ the modal intensity overlap. With respect to equation 2.11 the decrease of Stokes signal intensity due to the cavity losses equals

$$I_s(t) = I_s(0) e^{-\frac{\omega_s}{Q_s} t}. \tag{2.21}$$

The lasing threshold occurs when the cavity round-trip gain equals the round-trip loss, i.e., when

$$g_s \xi I_{c,threshold} \frac{c_0}{n_c} = \frac{\omega_s}{Q_s} \tag{2.22}$$

or

$$g_s \xi P_{p,threshold} \frac{\lambda_p}{2\pi n_c} \frac{Q_p}{V_m} \frac{c_0}{n_c} = \frac{2\pi c_0}{\lambda_s Q_s}. \tag{2.23}$$

Separating $P_{p,threshold}$ leads to the desired threshold equation:

$$P_{p,threshold} = \frac{(2\pi n_c)^2 V_m}{\xi g_s \lambda_s \lambda_p Q_s Q_p} \tag{2.24}$$

Note that this derivation neglects all possible other absorption processes. Especially for *free carrier absorption (FCA)* due to preliminary *two photon absorption (TPA)* this assumption could possibly be too optimistic. Therefore a detailed discussion about the influences of FCA and TPA in a silicon photonic crystal slab will be given later in the text.

2.2 Photonic Crystals

A photonic crystal is a periodic arrangement of electromagnetic media. Depending on whether we find a periodicity in one, two or three dimensions we speak of one-dimensional, two-dimensional and three-dimensional photonic crystal, respectively (Figure 2.4). In analogy to the periodicity of the crystalline atomic lattice in semiconductors, where the periodic potential of atoms creates an energetic band-structure for electrons, the 'optical potential', i.e., the varying dielectric constant, leads to the development of a band-structure for photons in photonic crystals. Resulting photonic bandgaps which disallow the propagation of light in the crystal for frequencies inside the gap and artificially introduced defects can be applied on the development of for example mirror, waveguide, or microcavity structures. To prepare the fundamentals which are necessary for our analysis of coupled photonic crystal resonator arrays we give a short introduction into the basic concepts of photonic crystals, thereby mainly following [25] and [26].

2.2.1 Maxwell's Equations in Periodic Dielectric Media

Assuming that each part of our structure is source-free, linear dielectric, macroscopic, isotropic and free of propagation losses and moreover possesses a magnetic permeability which is very close to unity and a

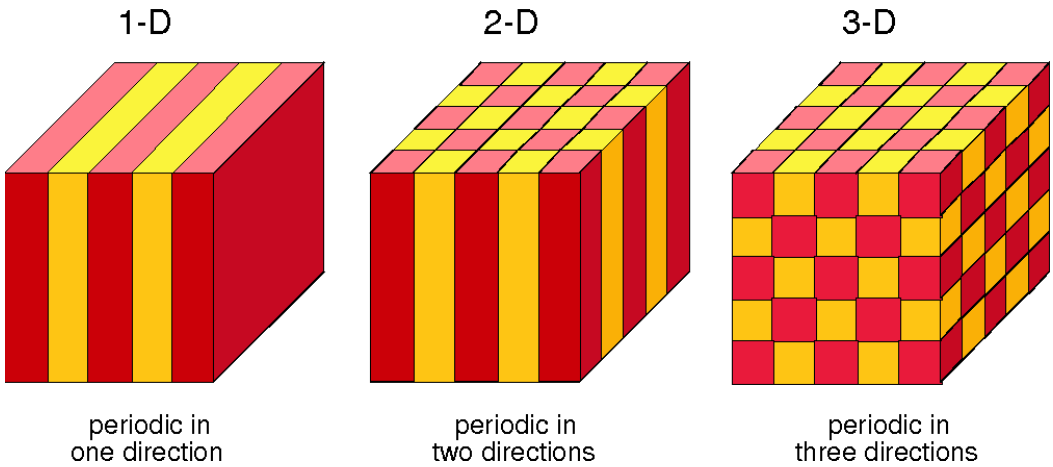

Figure 2.4: Schematic depiction of photonic crystals possessing a periodicity of the dielectric material structure in one, two and three directions [25]

dielectric constant which is not frequency dependent, we can combine Faraday's and Ampere's law to one equation in $\vec{H}$:

$$\vec{\nabla} \times \left(\frac{1}{\epsilon\left(\vec{r}\right)} \vec{\nabla} \times \vec{H}\left(\vec{r}\right) \right) = \left(\frac{\omega}{c_0} \right)^2 \vec{H}\left(\vec{r}\right) \tag{2.25}$$

Here $\epsilon\left(\vec{r}\right)$ is the dielectric function and c_0 is the vacuum speed of light. The equation holds for harmonic modes and is written in *cgs* units. When presuming a source free material, Maxwell's equations moreover predict $\vec{\nabla}\vec{H}(\vec{r}) = \vec{\nabla}\vec{D}(\vec{r}) = 0$ an thus a transversality constraint for the fields.

Equation (2.25) can be interpreted as an eigenvalue equation with the operator $\Theta = \vec{\nabla} \times \frac{1}{\epsilon(\vec{r})}\vec{\nabla}\times$ and the eigenvalues $(\frac{\omega}{c_0})^2$. Because Θ is *Hermitian* under the inner product $\int \vec{H}^* \vec{H}$ and ϵ is assumed to be positive and real everywhere, we find that ω^2 is positive and real, ω is real and that two different non-degenerate modes must be orthogonal.

An important property of Maxwell's equations is their *scalability*: Introducing a compressed or expanded version of $\epsilon(\vec{r})$,

$$\epsilon'(\vec{r}) = \epsilon(\frac{\vec{r}}{s}), \tag{2.26}$$

we, by insertion of $\vec{r}' = s\vec{r}$ in equation 2.25, easily find the expressions

$$\vec{H}'(\vec{r}') = \vec{H}(\frac{\vec{r}'}{s}) \text{ and } \omega' = \frac{\omega}{s}. \tag{2.27}$$

Thus if we want to find the new mode profile and frequency of a mode after stretching the structure, we just need to scale both by the same factor. Mathematically speaking, we find that geometrically similar structures possess similar electrodynamic properties. Keeping this in mind it is obviously too specific to analyze photonic crystal structures in an absolute length scale, but it is rather useful to describe the structure in a unified system. The common approach takes the periodicity of the basic square or triangular lattice, a, and thus determines all other parameters of the lattice in terms of this length scale as for example described for two-dimensional photonic crystal slabs in section 2.2.4.

2.2.2 Periodic Structures and the Bloch-Floquet-Formalism

A photonic crystal possesses discrete translational symmetry because of it's periodic dielectric function,

$$\epsilon(\vec{r}) = \epsilon(\vec{r} + \vec{R}), \tag{2.28}$$

where $\vec{R}$ is a *lattice vector* of the periodic structure. All possible lattice vectors can be expressed by a set of *primitive lattice vectors* $\{\vec{a_1}, \vec{a_2}, \vec{a_3}\}$ which are the smallest vectors pointing from one lattice point to another:

$$\vec{R} = \alpha\vec{a_1} + \beta\vec{a_2} + \gamma\vec{a_3} \tag{2.29}$$

Applying the *Bloch-Floquet formalism* for periodic eigenproblems, the solutions for such a periodic dielectric need to be of the form

$$\vec{H}\left(\vec{r}\right) = e^{i\vec{k}\vec{r}}\vec{H}_{n,\vec{k}}(\vec{r}) \tag{2.30}$$

where $\vec{H}_{n,\vec{k}}(\vec{r})$ is a periodic function with $\vec{H}_{n,\vec{k}}(\vec{r}) = \vec{H}_{n,\vec{k}}(\vec{r} + \vec{R})$ for all lattice vectors $\vec{R}$.

The eigenvalues $\omega_n(\vec{k})$ are continuous functions of $\vec{k}$ and can thus be plotted against $\vec{k}$ in a *dispersion diagram*. Moreover, as a result of the properties of the Fourier transform, the periodicity of $\vec{H}\left(\vec{r}\right)$ in real-space also leads to a periodicity in $\vec{k}$-space with the period $\vec{G}$. This fact causes the formation of bands indexed by n, i.e., we can find different frequency eigenvalues for every $\vec{k}$. Here $\vec{G}$ is a *reciprocal lattice vector* composed of a set of *primitive reciprocal lattice vector* $\{\vec{b_1}, \vec{b_2}, \vec{b_3}\}$ where the $\vec{b_j}$ must fulfill

$$\vec{a_i} \cdot \vec{b_j} = 2\pi\delta_{ij}. \tag{2.31}$$

To completely describe the properties of a lattice we only need to plot the band diagram along the smallest zone of inequivalent wavevectors closest to $\vec{k} = \vec{0}$, the first *Brillouin zone*.

If besides the discrete translational symmetry the lattice possesses other symmetries like mirror, inverse or rotational symmetry, there might be even more redundancies in the Brillouin zone allowing us to reduce it furthermore to the then *irreducible Brillouin zone*. This is exemplarily done for the two-dimensional square lattice in chapter 2.2.4.

2.2.3 The Electromagnetic Variational Theorem

For the understanding of bandgaps and defect states, a closer look at the variational principle is indispensable. We therefore need to define the *electromagnetic energy functional*:

$$E_f\left(\vec{H}_{n,\vec{k}}\right) = \frac{1}{2}\frac{\left(\vec{H}_{n,\vec{k}}, \Theta\vec{H}_{n,\vec{k}}\right)}{\left(\vec{H}_{n,\vec{k}}, \vec{H}_{n,\vec{k}}\right)} \tag{2.32}$$

The electromagnetic variational theorem states inductively that

- the lowest frequency mode minimizes this electromagnetic energy functional

and that

- the next higher order mode again minimizes the energy functional, but under the constraint of being orthogonal to all lower order modes:

$$\int \vec{H}^*_{n,\vec{k}}\vec{H}_{n,\vec{k}} = 0 \tag{2.33}$$

If we look more carefully at the energy functional [26], we arrive at

$$E_f\left(\vec{H}_{n,\vec{k}}\right) = \frac{1}{2\left(\vec{H}_{n,\vec{k}}, \vec{H}_{n,\vec{k}}\right)} \int d\vec{r} \frac{1}{\epsilon} \left|\vec{\nabla} \times \vec{H}_{n,\vec{k}}\right|^2 = \frac{1}{2\left(\vec{H}_{n,\vec{k}}, \vec{H}_{n,\vec{k}}\right)} \int d\vec{r} \frac{1}{\epsilon} \left|\frac{\omega}{c_0} \vec{D}_{n,\vec{k}}\right|^2 . \tag{2.34}$$

This equation, and thus the energy in the analyzed mode, is therefore minimized when the displacement field $\vec{D}_{n,\vec{k}}$ is concentrated in high dielectric index regions.

Opening of a Photonic Bandgap

Inversely applying relation 2.34, we can see that by forcing two equally symmetric, but with respect to the lattice shifted modes, for example $sin(\frac{\pi}{a}x)$ and $cos(\frac{\pi}{a}x)$ in a one-dimensional photonic crystal, to concentrate their displacement fields in regions of different dielectric indices, the former degenerate modes split into a higher energy air mode and a lower energy dielectric mode. This origin of the so called *bandgap* between the upper *dielectric band* and the lower *air band* is visualized for a one dimensional photonic crystal in figure 2.5.

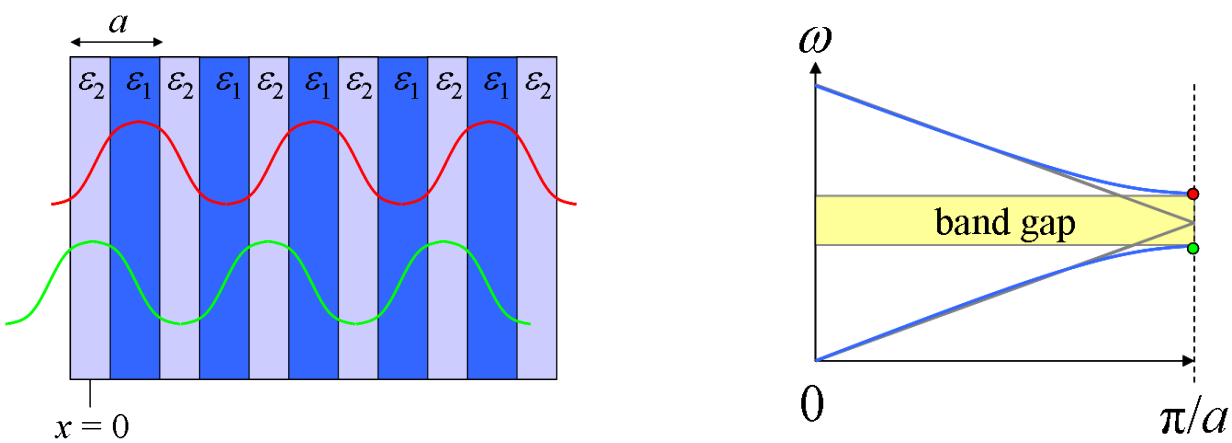

(a) The only two symmetrically possible $|\vec{D}|^2$ distributions at $k = \frac{\pi}{a}$: $f_1 = A_1 \sin(\frac{\pi}{a}x)$ (red) and $f_2 = A_2 \cos(\frac{\pi}{a}x)$ (green)

(b) Dispersion diagram of the periodic structure in (a)

Figure 2.5: Introducing a periodicity in a one-dimensional photonic crystal (a) leads to a splitting of former degenerate bands (b, gray) into the upper air (red) and the lower dielectric band (green) and thus to the opening of a photonic bandgap (yellow) [27]

Perturbation Theory

The variational theorem is closely related to perturbation theory approaches, a class of techniques to find the effect of small changes on known solutions to a set of equations. Writing Maxwell's equations, instead of equation (2.25), as a generalized eigenproblem in terms of the electric field, we achieve:

$$\vec{\nabla} \times \vec{\nabla} \times \vec{E}_{n,\vec{k}}\left(\vec{r}\right) = \left(\frac{\omega}{c_0}\right)^2 \epsilon\left(\vec{r}\right) \vec{E}_{n,\vec{k}}\left(\vec{r}\right) \tag{2.35}$$

To later understand the appearance of defect states we focus on small changes $\Delta\epsilon$ in the dielectric. Expanding the new eigensolutions $\vec{E}_{n,\vec{k}}$ and ω_n in powers of n, one arrives [28] at the first order correction

$$\Delta\omega_n^{(1)} = -\frac{\omega_n(\vec{k})}{2}\frac{\int \Delta\epsilon \left|\vec{E}_{n,\vec{k}}\right|^2}{\int \epsilon \left|\vec{E}_{n,\vec{k}}\right|^2} \tag{2.36}$$

where the integral is calculated over the primitive cell of the lattice.

However, if we try to apply this first order expression on structures with sudden changes of the dielectric constant, i.e., ϵ is a step function in space and $\Delta\epsilon$ is a small shift Δh of a dielectric boundary between ϵ_1 and ϵ_2, the integral in the numerator of equation (2.36) becomes ill defined because the normal component $E_\perp$ to the interface is discontinuous at the boundary. This problem is solved in [28] by an anisotropicly smoothed system, yielding the surface integral

$$\Delta\omega_n^{(1)} = -\frac{\omega_n(\vec{k})}{2}\frac{\iint \Delta h \left((\epsilon_1-\epsilon_2)\left|\vec{E}_{||}\right|^2 - \left(\epsilon_1^{-1}-\epsilon_2^{-1}\right)|D_\perp|^2\right)}{\int \epsilon \left|\vec{E}_{n,\vec{k}}\right|^2}. \tag{2.37}$$

2.2.4 Two-Dimensional Photonic Crystals

A two dimensional photonic crystal possesses periodicity in two directions which we here arbitrarily want to label as $\hat{e_x}$ and $\hat{e_y}$. To achieve a complete photonic bandgap we need to fulfill two basic conditions:

First we need overlapping bandgaps for each $\vec{k}$ point in each direction of the irreducible Brillouin zone. This means that for a given ω_0' inside the gap there exists no possible real value of $\vec{k}_{||}$, the mode is evanescent inside the crystal.

Second in a two-dimensional photonic crystal there are basically two types of polarization: transverse electrical (TE) modes with the electric field in plane and the magnetic field in $\hat{e_z}$-direction and transverse magnetic (TM) modes with the magnetic field in plane and the electric field perpendicular in $\hat{e_z}$-direction. To achieve a complete bandgap, both of the bandgaps of these two polarizations which possess entirely different band-structures need to overlap. Taking into account the vectorial boundary conditions of the electric field we can analytically find a heuristic of the topology of a lattice which possesses this behavior [25]: the dielectric structure should consist of dielectric veins which contain an electric field oriented parallel to them.

Note that structures with low index holes and high index dielectric are better suited for TE-modes, while structures composed of dielectric rods surrounded by air possess a larger TM-bandgap. Especially the later analyzed lattice of air holes in a silicon slab usually does not posses a TM bandgap at all.

The Two-Dimensional Square Lattice

The simplest two-dimensional lattice is the square lattice which will also be the basis for the coupled photonic crystal resonator arrays discussed in chapter 2.3. The lattice itself and its lattice vectors are depicted in figure 2.6(a), its unit cell in figure 2.6(b) and its irreducible Brillouin zone in figure 2.6(c). The primitive lattice vectors are $\vec{a}_1 = a\hat{e_x}$ and $\vec{a}_2 = a\hat{e_y}$, its primitive reciprocal lattice vectors are $\vec{b}_1 = \frac{2\pi}{a}\hat{e_y}$ and $\vec{b}_2 = \frac{2\pi}{a}\hat{e_x}$.

An example of a band diagram of a two dimensional square-lattice with dielectric rods in air is presented in figure 2.7(a). The dispersion relation is plotted along the edges of the irreducible Brillouin zone, the high symmetry points Γ, X and M correspond to the wavevectors $\vec{k}_{||} = 0$, $\vec{k}_{||} = \frac{\pi}{a}\hat{e_x}$ and $\vec{k}_{||} = \frac{\pi}{a}\hat{e_x} + \frac{\pi}{a}\hat{e_y}$, respectively.

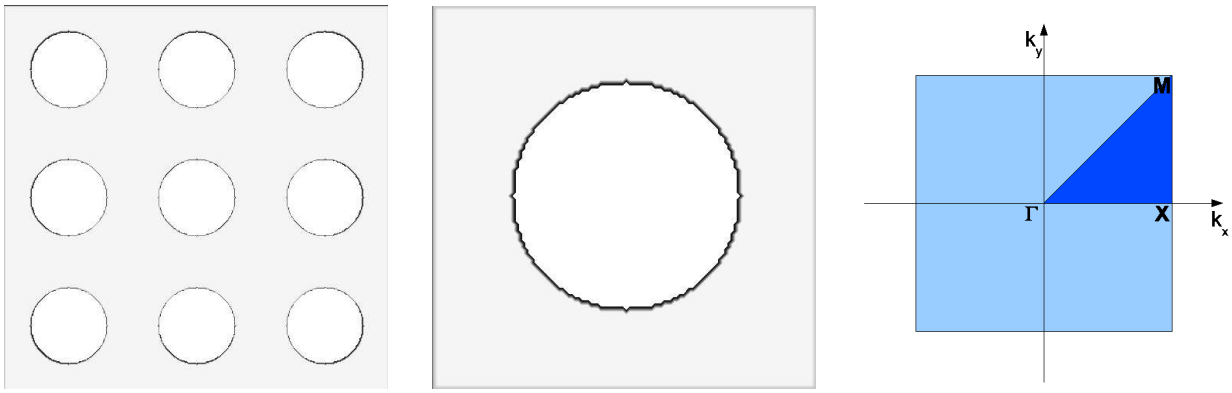

(a) Lattice section (dimensions $3a \times 3a$)

(b) Unit cell (dimensions $a \times a$)

(c) Brillouin zone (light blue) and irreducible Brillouin zone (dark blue)

Figure 2.6: Visualization of the square lattice with circular holes, its unit cell and its Brillouin zone; Γ, X and M correspond to the wavevectors $\vec{k_{||}} = (0,0)$, $\vec{k_{||}} = \left(\frac{\pi}{a}, 0\right)$ and $\vec{k_{||}} = \left(\frac{\pi}{a}, \frac{\pi}{a}\right)$, respectively

Photonic Crystal Slabs

A real 2D photonic crystal will always be finite in the $\hat{e_z}$-direction. Light confinement in this direction is then achieved by *index guiding*, a generalization of total internal reflection. Therefore *guided modes* can just be found below the *light line*

$$\omega = c_0 \left|\vec{k}_{||}\right| . \tag{2.38}$$

Assuming that our slab possesses mirror symmetry we again will find just two categories of modes: *TE-like* (even) and *TM-like* (odd) modes. These have the properties of ideal TE and TM modes at the center of the slab, but contain all field components at $z \neq 0$.

With respect to possible applications and our later focus on coupled photonic crystal resonator arrays we will from now on focus on 2D photonic crystal slabs with air holes in silicon which are arranged in a basic square lattice. A band diagram along the axes of high symmetry of a photonic crystal slab with a slab thickness of $\frac{d}{a} = 0.55$ and air holes with a radius $\frac{r}{a} = 0.4$ in $n = 3.6$ dielectric is depicted in figure 2.7(b). The light line $\omega = c_0|\vec{k}_{||}|$ is plotted in red. Because of the slopes of the bands the TE-band edge in a square lattice slab is determined only by the values of the lower band edge at M and the upper band edge at X.

Note that besides the usual four parameters of a two-dimensional photonic crystal lattice, the *lattice type*, the *refractive index* of the materials, the *periodicity* a and the *hole radius* $\frac{r}{a}$, the band structure of photonic crystal slabs is moreover highly sensitive to the *slab thickness* $\frac{d}{a}$.

Defect Modes in Two-Dimensional Photonic Crystals

In the discussion above we have seen that a photonic crystal slab of air holes in silicon can exhibit a bandgap disallowing in-plane propagation of electromagnetic waves inside the bandgap, i.e., the density of states of frequencies inside the bandgap is zero. However, remembering the results of equations (2.36) and (2.37), we see that an increase $\Delta\epsilon$ in the dielectric constant, for example by slightly decreasing the hole radius of one hole, leads to a decrease in frequency. It is important to note that this decrease happens locally while the surrounding lattice still works as a mirror with approximately the calculated band structure.

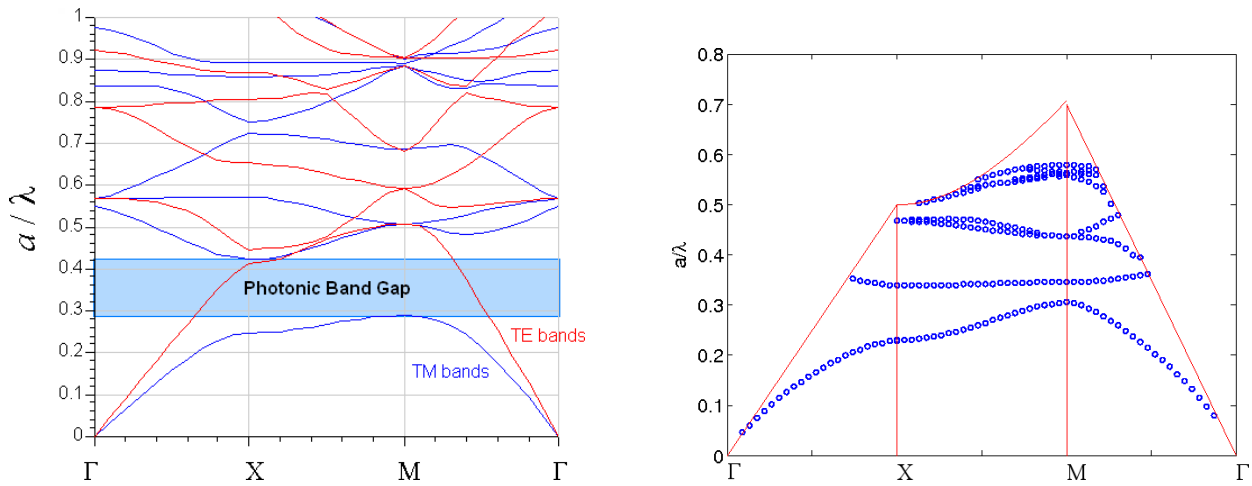

(a) Example of TE (red) and TM (blue) band diagrams of an ideal infinite two-dimensional square lattice of dielectric rods [27]

(b) TE band diagram of a photonic crystal square lattice slab with a slab thickness of $\frac{d}{a} = 0.55$ and air holes with a radius $\frac{r}{a} = 0.4$ in $n = 3.6$ dielectric [29]

Figure 2.7: Two band diagrams of different two-dimensional square lattices

If we now focus on a state which before the perturbation was part of the lower edge of the air band, this state is now pulled into the bandgap of the surrounding lattice. We achieve a localized *defect state*. Of course, by increasing the hole radius it is also possible to push states from the dielectric band into the bandgap. It shall be mentioned that, strictly speaking, the discrete translational symmetry of the lattice is already broken by one defect and the crystal could no longer be characterized by the concept of a $\vec{k}$-vector. But, as the periodic remainder of the ideally infinite lattice still works effectively as a perfect mirror, we can interpret our defect state as a single state in front of the background of the basic band structure.

As we can imagine different types of crystal defects, for example single defects, linear defects and group defects, there are various possible applications. For the integration of Raman scattering, we need a resonator with high quality factors and the support of two defect modes with a desired modal splitting of $f = 15.6THz$. Approaches to realize this in photonic crystals would be the usage of a single or a linear defect cavity as proposed in [15] or realization in photonic crystal waveguides as analyzed in [12]. However, recent results have made another structure seem much more promising for the achievement of high output powers, namely two-dimensional coupled photonic crystal resonator arrays which will be discussed in the following chapter.

2.3 Two-Dimensional Coupled Photonic Crystal Microcavity Arrays

In 2003 H. Altug and J. Vučković presented a new photonic crystal structure referred to as *Two-dimensional coupled photonic crystal resonator arrays (CPCRA)* [16]. Instead of perturbing a photonic bandgap structure with a single defect, they introduced a periodic perturbance by removing every for example third hole in a square lattice slab as depicted in figure 2.8(a). The size of the CPCRA unit cell therefore increases according to the numbers of layers between the cavities as visualized in figure 2.8(b). This increase of the unitcell conversely induces a decrease of the irreducible Brillouin zone of the underlying square lattice. Introducing a number of $\tilde{l}$ layers between the cavities in each direction, i.e., increasing the size of the unit cell to a square with $l = \tilde{l} + 1$ layers in each direction, one achieves again a triangular irreducible Brillouin

zone with the corners Γ, X and M (figure 2.8(c)), but which in this case correspond to

$$\vec{k}_{||,\Gamma} = (0,0)\,,\ \vec{k}_{||,X} = \left(0, \frac{\pi}{la}\right) \text{ and } \vec{k}_{||,M} = \left(\frac{\pi}{la}, \frac{\pi}{la}\right), \tag{2.39}$$

respectively.

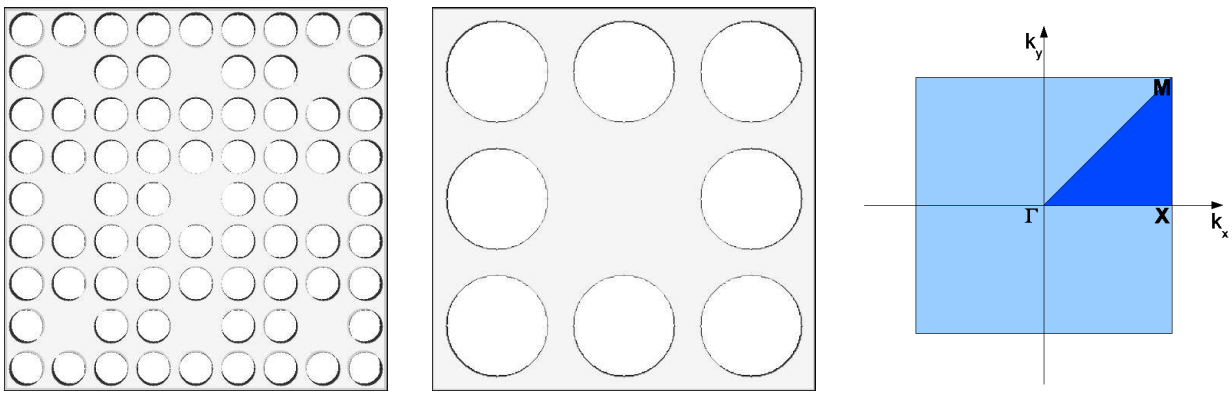

(a) Lattice section (dimensions $3la \times 3la$)

(b) Unit cell (dimensions $la \times la$)

(c) Brillouin zone (light blue) and irreducible Brillouin zone (dark blue)

Figure 2.8: Visualization of a CPCRA, its unit cell and its Brillouin zone; Γ, X and M correspond to the wavevectors $\vec{k}_{||} = (0,0)$, $\vec{k}_{||} = \left(\frac{\pi}{la}, 0\right)$ and $\vec{k}_{||} = \left(\frac{\pi}{la}, \frac{\pi}{la}\right)$, respectively

In the previous section we described how reducing the radius of just one hole pulls modes from the air band into the bandgap. For the case of a completely removed hole such a single cavity supports basically three types of confined modes: a nondegenerate monopole, two degenerate dipole modes and a nondegenerate quadrupole mode. Following the analysis in [16], tiling an array of such cavities together leads to the formation of coupled cavity bands as depicted in figure 2.9(a). Similar to the case of single cavities we here again assume as an approximation that the basic band structure of the underlying square lattice remains unaffected. Note that because of the increased unit cell the shaded plots of these basic bands need to be l times folded along each direction of high symmetry and thus only contain the minimum of the air band and the maximum of the dielectric band of the original undisturbed square lattice.

The formed defect bands consist of the expected three different modes:

- A coupled *monopole band* exhibits low quality factors and is not located inside the full photonic bandgap of the underlying square lattice. The monopole modes are the partly confined modes of highest frequency. However, there is no direction of preferential coupling or polarization of the monopole modes. The B_z field of a monopole mode at the Γ point is depicted in the lower left corner of figure 2.9(b).

- The coupled *quadrupole band* possesses good lateral confinement and the band itself is very flat, which implies very slow group velocities at around $c_{quadrupole} \approx 10^{-2} c_0$ as reported in [17]. Again, we observe no distinct direction of preferential coupling or polarization. The high quality factors of the quadrupole modes suggest possible usage for laser arrays as recently reported in [19]. A major difficulty in this case is the fact that it is very difficult to couple and therefore excite the quadrupole mode in a perpendicular angle of impinging light. Quadrupole modes at the X and M points are depicted in the upper left and right images of figure 2.9(b).

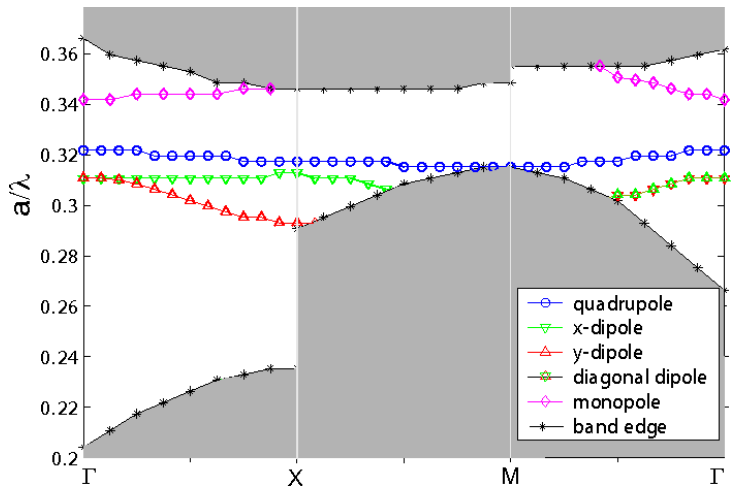

(a) Banddiagram of the three different defect modes in front of the folded band diagram of the underlying photonic crystal lattice

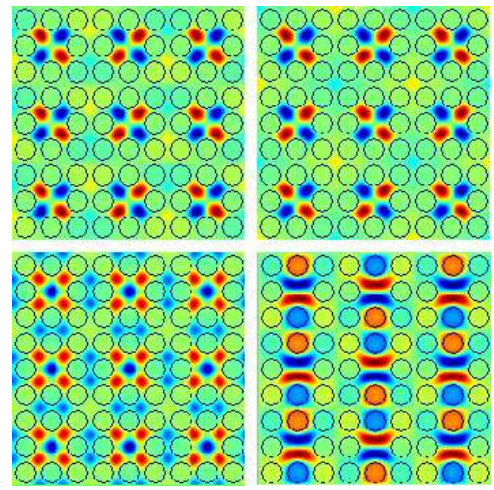

(b) B_z-field patterns of the quadrupole mode at X (top left), the quadrupole mode at M (top right), the monopole mode at Γ (bottom left) and the x-dipole mode at X (bottom right)

Figure 2.9: TE-mode band diagram and defect mode B_z-field patterns of a two dimensional coupled photonic crystal resonator array with a slab thickness of $\frac{d}{a} = 0.55$, an air hole radius of $\frac{r}{a} = 0.4$ in silicon with assumed $n_{Si} = 3.5$ and a number of $l = 3$ unit cell layers in each direction, calculated using the Finite-Difference Time-Domain method [16]

- The third band is the doubly degenerate *dipole band*. The degeneracy of the x- and y-dipole modes is broken as soon as the fourfold rotational symmetry of the structure and the incident light is reduced to a twofold one by impinging slightly apart from the Γ point. The dipole modes exhibit generally good, but still lower quality factors than the quadrupole modes and moreover slightly higher group velocities. However, these disadvantages come with one important other property: only twofold rotational intensity symmetry of each of the modes.

  This is for example embodied in preferential polarization of the two modes: while the $\vec{E}$-fields of the x-dipole predominantly consist of E_x components, the y-dipole exhibits mostly E_y. Moreover, both modes posses quite distinct directions of coupling comparable to the propagation directions of Hertz's dipole antenna. These properties and especially their application and manipulation in CPCRA structures designed to achieve stimulated Raman scattering will be discussed in detail later in the text.

All the above mentioned properties of CPCRAs suggests them as highly applicable on various problems. The theoretical analyses and also the experimental realizations of slow group velocities in CPCRAs [17], polarization control [18], highly sensitive refractive index sensing [18] and a photonic crystal nanocavity array laser on InP [19] have thus been reported recently.

2.4 The Finite-Difference Time-Domain Method

The Finite-Difference Time-Domain is an electromagnetic modeling technique generally belonging to the class of differential time-domain modeling methods [30]. It is based directly on Maxwell's equations which makes it very well applicable on for example photonic crystals with their sharp discontinuities of dielectric

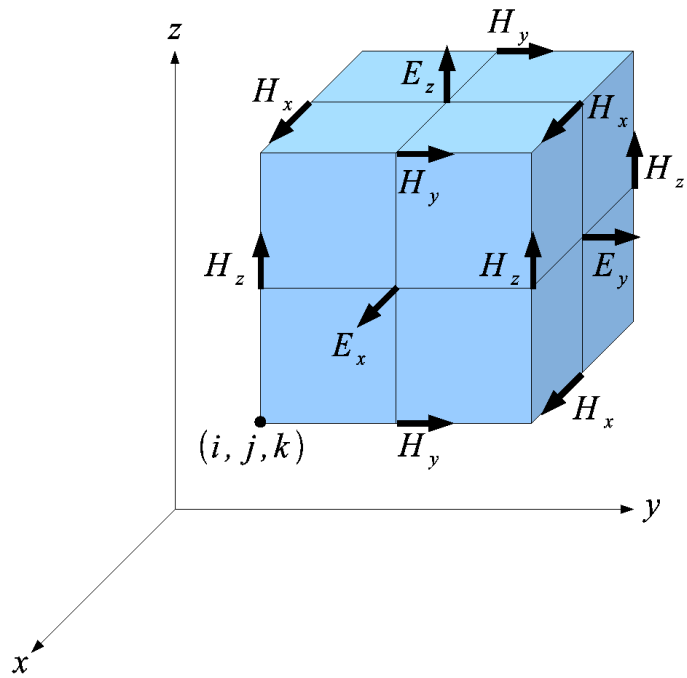

Figure 2.10: Yee cell containing the spatial positions and orientations of the $\vec{E}$ and $\vec{H}$ components

materials. As most of our later results are based on FDTD simulations, this chapter summarizes the basic concepts of FDTD with respect to its application on photonic crystal simulations.

2.4.1 The Yee Algorithm

In 1966 Kane S. Yee came up with the idea of replacing Maxwell's equations by a set of finite difference equations [31]. The Yee algorithm solves the coupled Maxwell's curl equations, repeated here for convenience in MKS units as used in [32]

$$\frac{\partial \vec{H}}{\partial t} = -\frac{1}{\mu}\vec{\nabla} \times \vec{E} - \frac{1}{\mu}\left(\vec{M}_{source} + \sigma^* \vec{H}\right) \tag{2.40}$$

$$\frac{\partial \vec{E}}{\partial t} = \frac{1}{\epsilon}\vec{\nabla} \times \vec{H} - \frac{1}{\epsilon}\left(\vec{J}_{source} + \sigma \vec{E}\right), \tag{2.41}$$

for both the $\vec{E}$ and $\vec{H}$ field in time. The simulated volume is therefore discretized into so called *Yee cells* as depicted in figure 2.10. The $\vec{E}$- and $\vec{H}$-field components are distributed in a way that every $\vec{E}$ component is surrounded by four circulating $\vec{H}$ components and every $\vec{H}$ component is surrounded by four circulating $\vec{E}$ components, respectively.

This staggered spatial grid of $\vec{E}$ and $\vec{H}$ is updated at discrete timesteps Δt in a *leapfrog* manner: At times $t = (n + \frac{1}{2})\Delta t$ the new $\vec{E}$ field components are calculated using the spatial derivatives of the surrounding $\vec{H}$ vectors at times $t = n\Delta t$ and the former electric field at time $t = (n - \frac{1}{2})\Delta t$, while at times $t = (n+1)\Delta t$ the new $\vec{H}$ field components are calculated using the spatial derivatives of the surrounding $\vec{E}$ vectors at times $t = (n + \frac{1}{2})\Delta t$ and the former magnetic field at times $t = n\Delta t$.

The space and time derivatives of equation (2.40) are expressed by second-order accurate centered finite-differences of the form [32]:

$$\frac{\partial u}{\partial x}(i\Delta x, j\Delta y, k\Delta z, n\Delta t) = \frac{u\left((i+\frac{1}{2})\Delta x, j\Delta y, k\Delta z, n\Delta t\right) - u\left((i-\frac{1}{2})\Delta x, j\Delta y, k\Delta z, n\Delta t\right)}{\Delta x} + O\left[(\Delta x)^2\right] \quad (2.42)$$

Without loss of generality, following the derivation of [32] and using it's terminology, we now focus on the component $E_x|^{n+\frac{1}{2}}_{i,j+\frac{1}{2},k+\frac{1}{2}}$.

Using the semi-implicit approximation

$$E_x|^{n}_{i,j+\frac{1}{2},k+\frac{1}{2}} = \frac{E_x|^{n+\frac{1}{2}}_{i,j+\frac{1}{2},k+\frac{1}{2}} + E_x|^{n-\frac{1}{2}}_{i,j+\frac{1}{2},k+\frac{1}{2}}}{2} \quad (2.43)$$

for the in the leapfrog-timestepping jumped over component $E_x|^{n}_{i,j+\frac{1}{2},k+\frac{1}{2}}$, we find:

$$E_x|^{n+\frac{1}{2}}_{i,j+\frac{1}{2},k+\frac{1}{2}} = C_a(m)\, E_x|^{n-\frac{1}{2}}_{i,j+\frac{1}{2},k+\frac{1}{2}} + C_b(m)\cdot(H_z|^{n}_{i,j+1,k+\frac{1}{2}} - H_z|^{n}_{i,j,k+\frac{1}{2}} + H_y|^{n}_{i,j+\frac{1}{2},k} - H_y|^{n}_{i,j+\frac{1}{2},k+1} - J_{source_x}|^{n}_{i,j+\frac{1}{2},k+\frac{1}{2}}\Delta) \quad (2.44)$$

Here $C_a(m)$ and $C_b(m)$ are the values of the material coefficient arrays C_a and C_b at the point $m = MEDIA_{E_x}|_{i,j+\frac{1}{2},k+\frac{1}{2}}$ where $MEDIA_u|_{i,j,k}$ are different integer pointer arrays for each field component u.

This expression for $E_x|^{n+\frac{1}{2}}_{i,j+\frac{1}{2},k+\frac{1}{2}}$ can easily be converted for the other five field components of the Yee cell, which yields an *explicit* expression for evolving our field one timestep Δt in time.

Note that after each Δt every field component in every cell of our grid is updated. For other possible discretization grids like unstaggered, hexagonal or nonuniform structures the interested reader is referred to for example [32].

Although the Yee algorithm was originally derived from Maxwell's curl equations, our results also directly represent Faraday's and Ampere's law in integral form, which is of importance for modeling fine geometrical features. Moreover, equation (2.44) and its analogues also imply a divergence free nature, i.e., they implicitly enforce Maxwell's

$$\vec{\nabla}\cdot\vec{D} = 0 \quad (2.45)$$

$$\text{and } \vec{\nabla}\cdot\vec{B} = 0. \quad (2.46)$$

Numerical Dispersion

The Yee algorithm causes nonphysical anisotropic dispersion because of numerical errors. The ideal dispersion relation for a physical plane wave propagating in three dimensions in a homogeneous lossless medium should be:

$$\left(\frac{w}{c_0}\right)^2 = k_x^2 + k_y^2 + k_z^2 \quad (2.47)$$

However, for a cubic grid with $\Delta x = \Delta y = \Delta z =: \Delta$ we obtain for the numerical wavevectors $\tilde{k_x}$, $\tilde{k_y}$ and $\tilde{k_z}$ the following general form of the numerical dispersion relation in a cubic cell-grid:

$$\left(\frac{1}{c\Delta t} sin\left(\frac{\omega\Delta t}{2}\right)\right)^2 = \left(\frac{1}{\Delta} sin\left(\frac{\tilde{k_x}\Delta}{2}\right)\right)^2 + \left(\frac{1}{\Delta} sin\left(\frac{\tilde{k_y}\Delta}{2}\right)\right)^2 + \left(\frac{1}{\Delta} sin\left(\frac{\tilde{k_z}\Delta}{2}\right)\right)^2 \quad (2.48)$$

This result implies errors in the phase-velocity compared to its physical value as well as anisotropy errors for different angles of wave propagation depending on the *Courant number*

$$S \equiv \frac{c_0 \Delta t}{\Delta} \tag{2.49}$$

and on the *grid-sampling density*

$$N_\lambda \equiv \frac{\lambda_0}{\Delta}. \tag{2.50}$$

Moreover, a small grid sampling density cannot handle small spatial structures accurately. However, these are essential for photonic crystals. One way to overcome this weakness is to apply effective ϵ values to smoothen the edges of a coarsely discretized structure as we will see in section 2.4.4.

Numerical Stability

As mentioned in [31] and derived in [32], numerical instability of the Yee algorithm with a rectangular grid occurs for

$$\Delta t > \frac{1}{c_0 \sqrt{\frac{1}{(\Delta x)^2} + \frac{1}{(\Delta y)^2} + \frac{1}{(\Delta z)^2}}}. \tag{2.51}$$

Using definition (2.49) we find the *Courant stability limit* for the three-dimensional cubic-cell space lattice:

$$S_{stablein3D} < \frac{1}{\sqrt{3}} \tag{2.52}$$

Note that stability of the overall FDTD method not only requires stability of the basic Yee algorithm, but is moreover influenced by uncertainties like for example absorbing boundary conditions, variable or unstructured meshing and lossy, nonlinear or amplifying materials.

2.4.2 Boundary Conditions

As for FDTD all field components are updated in one timestep Δt the whole amount of spatial components needs to be stored in the computational memory. Unfortunately any kind of memory is limited in size, which enforces us to reduce any FDTD simulation to a *computational domain* which indeed is limited in size, but large enough to enclose the structure of interest. To simulate the behavior and to calculate the spatial derivatives at the edges $\delta\Omega$ of this domain Ω, we need to apply suitable *boundary conditions*.

Absorbing Boundary Conditions

If we desire only outward propagating numerical waves at the edge $\delta\Omega$, the boundary conditions must suppress reflections at $\delta\Omega$ to an acceptable level. These *absorbing boundary conditions (ABC)* are still a subject of ongoing research and can today basically be divided into *analytical absorbing boundary conditions* and *perfectly matched layer (PML) absorbing boundary conditions*.

PML absorbing boundary conditions were introduced by Berenger in 1994 [33]. They embed the basic computational domain in a perfectly matched additional medium which is just a few lattice cells thick, reflectionless to all incident waves and highly absorbing. By introducing a split-field formulation of Maxwell's equations which leads to twelve coupled first-order partial differential equations and by choosing loss parameters consistent with a dispersionless medium, Berenger derives a PML matching plane waves of arbitrary incidence, polarization and frequency. PML absorbers are able to handle inhomogeneous, dispersive, anisotropic and nonlinear media, but may suffer from possible instabilities. Following Berenger's work,

further improvements were made introducing *convolutional perfectly matched layers (CPML)* and *uniaxial perfectly matched layers (UPML)* as presented in [32].

Analytical absorbing boundary conditions, however, suppress reflections by analytical means like radiation operators, application of one-way wave equations, extrapolation methods or complementary operators.

One important case for our later application of FDTD simulations is the *Mur finite difference-scheme* of the *Engquist-Majda one-way wave equations*. One way wave equations permit propagation of waves just in one direction, which applied at the edge $\delta\Omega$ numerically absorbs impinging waves. Considering a wave function U and the three dimensional wave equation

$$GU = 0 \tag{2.53}$$

with

$$G \equiv \frac{\partial^2}{\partial x^2} + \frac{\partial^2}{\partial y^2} + \frac{\partial^2}{\partial z^2} - \frac{1}{c_0^2}\frac{\partial^2}{\partial t^2} \equiv D_x^2 + D_y^2 + D_z^2 - \frac{1}{c_0^2}D_t^2 \tag{2.54}$$

and moreover factoring G as $GU = G^+G^-U$ with

$$G^+ \equiv D_x + \frac{D_t}{c_0}\sqrt{1-s^2}, \tag{2.55}$$

$$G^- \equiv D_x - \frac{D_t}{c_0}\sqrt{1-s^2} \text{ and} \tag{2.56}$$

$$s \equiv \sqrt{\left(\frac{D_y}{\frac{D_t}{c_0}}\right)^2 + \left(\frac{D_z}{\frac{D_t}{c_0}}\right)^2} \tag{2.57}$$

we find that the conditions

$$G^-U|_{x=0} = 0 \text{ and } G^+U|_{x=l} = 0 \tag{2.58}$$

hold at the borders $x = 0$ and $x = l$ of our computational domain as proved by Engquist and Majda. That means that for example G^- applied to a scalar wavefunction U at the $x = 0$ boundary exactly absorbs a plane wave impinging to this boundary at an arbitrary angle. Without loss of generality we now want to focus on this $x = 0$ boundary:

Writing $\sqrt{1-s^2}$ as a second-order accurate approximation

$$\sqrt{1-s^2} \cong 1 - \frac{s^2}{2} \tag{2.59}$$

yields the second-order accurate approximation for G^-

$$\left(D_x - \frac{D_t}{c_0} + \frac{c_0 D_y^2}{2D_t} + \frac{c_0 D_z^2}{2D_t}\right)U = 0 \tag{2.60}$$

and thus the desired second-order accurate absorbing boundary condition at $x = 0$:

$$\frac{\partial^2 U}{\partial x \partial t} - \frac{1}{c_0}\frac{\partial^2 U}{\partial t^2} + \frac{c_0}{2}\frac{\partial^2 U}{\partial y^2} + \frac{c_0}{2}\frac{\partial^2 U}{\partial z^2} = 0 \tag{2.61}$$

The *Mur finite difference expression* for this boundary condition is achieved by implementing the partial derivatives of equation (2.61) as numerical central differences expanded around the auxiliary gridpoint

$(\frac{1}{2}, j, k)$. Letting $W|^n_{0,j,k}$ represent a component of $\vec{H}$ or $\vec{E}$ tangential to our boundary $x = 0$ we achieve for the cubic lattice the following time-stepping algorithm:

$$\begin{aligned} W|^{n+1}_{0,j,k} = &- W|^{n-1}_{1,j,k} + \frac{c_0\Delta t - \Delta}{c_0\Delta t + \Delta}\left(W|^{n+1}_{1,j,k} + W|^{n-1}_{0,j,k}\right) + \frac{2\Delta}{c_0\Delta t + \Delta}\left(W|^n_{0,j,k} + W|^n_{1,j,k}\right) \\ &+ \frac{(c_0\Delta t)^2}{2\Delta(c_0\Delta t + \Delta)}(W|^n_{0,j+1,k} - 4W|^n_{0,j,k} + W|^n_{0,j-1,k} + W|^n_{1,j+1,k} - 4W|^n_{1,j,k} \\ &+ W|^n_{1,j-1,k} + W|^n_{0,j,k+1} + W|^n_{0,j,k-1} + W|^n_{1,j,k+1} + W|^n_{1,j,k-1}) \end{aligned} \tag{2.62}$$

Periodic Boundary Conditions

Although we are bound to a finite computational domain, it is possible to simulate infinite structures as long as they are periodic. We therefore use the Bloch-Floquet formalism discussed in chapter 2.2.2:

$$\vec{E}\left(\vec{r} + \vec{R}\right) = \vec{E}\left(\vec{r}\right) e^{i\vec{k}\vec{R}} \text{ and } \vec{H}\left(\vec{r} + \vec{R}\right) = \vec{H}\left(\vec{r}\right) e^{i\vec{k}\vec{R}} \tag{2.63}$$

To implement this in FDTD, we restrict the computational domain to the unit cell of the periodic structure. One now only needs to assure that a field component outgoing of the structure at one side appears phase-shifted at the inverse point of the unit cell by defining one special $\vec{k}$. Note that different from the common FDTD schemes we therefore need to use complex-valued $\vec{E}$ and $\vec{H}$ fields.

Mirror Boundary Conditions

An effective and accurate method to reduce the computational domain and at the same time to become able to distinguish between TE- and TM-like modes is the use of symmetries. One therefore needs to find a mirror plane of the analyzed structure, for example the center plane of a photonic crystal slab, and to reduce the simulated volume to one unique half of the structure.

For TE-like (TM-like) modes this is achieved by applying a *perfect magnetic conductor (PMC) (perfect electric conductor (PEC))* boundary at the actual center x-y-plane of the photonic crystal slab. This PMC (PEC) boundary is realized by enforcing $B_x = B_y = 0$ ($E_x = E_y = 0$) and thus odd mirror symmetry of the in-plane $\vec{B}$- ($\vec{E}$-) field components. Gauss', Faraday's and Ampere's law moreover yield even, odd and even symmetry for the B_z, E_z and $E_{x,y}$ (E_z, B_z and $B_{x,y}$) field components, respectively.

Note that in FDTD simulations the enforced in-plane $\vec{B}$- ($\vec{E}$-) field components are actually shifted in $\hat{z}$ by half the length of a unit cell $\frac{\Delta z}{2}$. However, the simulated center of the slab exactly belongs to the spatial position of this plane. As the later used unit cell is also shifted by $\frac{\Delta z}{2}$ compared to the Yee cell depicted in figure 2.10, the in-plane $\vec{E}$-field components are situated at the bottom of the unit cell, which implies that in the case of TM-like modes, i.e., PEC boundary conditions, we can simulate a real slab thickness of $d_{slab,real,TM} = 2d_{slab,FDTD,TM}$. For the realization of TE-like modes we instead add an artificial additional half-cell below the lowest real lattice cells and apply PMC boundary conditions on the in-plane $\vec{B}$-field components, which results in a simulated slab thickness of $d_{slab,real,TE} = 2d_{slab,FDTD,TE} + 1$.

2.4.3 Quality Factor Calculation

The finite-difference time-domain method offers various approaches to calculate the quality factor of photonic crystal microcavities. We here want to highlight the three most common ones which will later be applied on an analyzed CPCRA Raman laser. For convenience, we in this section consider a single cavity in a photonic crystal slab.

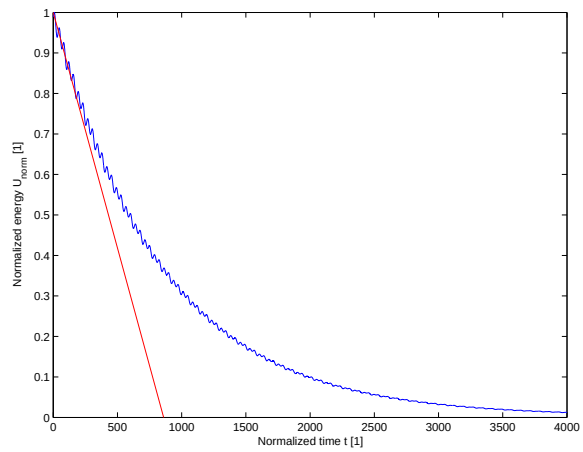

Figure 2.11: Energy decay of the x-dipole mode in the single cavity approximation of a CPCRA with $\frac{r_x}{a} = 0.4$ and $\frac{r_y}{a} = 0.3$ at $\frac{a}{\lambda} = 0.26842$ as used in chapter 5.3.1

The definition of the quality factor given in equation 2.9,

$$Q = \omega_0 \frac{U}{P}, \tag{2.64}$$

is written in terms of the stored energy U and the dissipating power P, time-averaged over one optical cycle. As we can distinguish between power which leaves the cavity in the photonic crystal plane and the power dissipating through the bottom and the top of the slab, we can rewrite this equation as

$$\frac{1}{Q_{total}} = \frac{1}{\omega_0} \frac{P_\perp + P_{||}}{U} = \frac{1}{\omega_0} \frac{P_\perp}{U} + \frac{1}{\omega_0} \frac{P_{||}}{U} = \frac{1}{Q_\perp} + \frac{1}{Q_{||}} \tag{2.65}$$

with the *out-of-plane quality factor* $Q_\perp$ and the *in-plane quality factor* $Q_{||}$.

As discussed in chapter 2.1.2, the Q-factor of an optical microcavity can generally be expressed in a variety of ways. The realization of these different expressions in FDTD straightly leads to the following calculation schemes:

Analysis of the Cavity Frequency Spectrum

Assuming a Lorentzian shape of the peak of the analyzed mode in the frequency spectrum of the cavity, we can apply equation 2.14:

$$Q = \frac{\omega_0}{\Delta\omega} \tag{2.66}$$

Thus the quality factor can be estimated by dividing the mode frequency by the full-width half-maximum of the spectral Lorentzian. However, the measured Q is equal to Q_{total}, a separation into $Q_\perp$ and $Q_{||}$ is not possible.

Measurement of the Energy Decay

Equation 2.11,

$$U(t) = U_0 e^{-\frac{\omega_0 t}{Q}}, \tag{2.67}$$

suggests the calculation of the quality factor by measurement of the energy decay in a photonic crystal cavity and subsequent exponential fitting of the curve as depicted in figure 2.11. The energy is therefore composed as a sum of the energies in the electric and magnetic fields and calculated as

$$U = \frac{1}{2}\iiint_V \epsilon\left(\vec{r}\right)\left|\vec{E}\left(\vec{r},t_0\right)\right|^2 d^3\vec{r} + \frac{1}{2}\iiint_V \mu\left(\vec{r}\right)\left|\vec{H}\left(\vec{r},t_0\right)\right|^2 d^3\vec{r}, \tag{2.68}$$

where V is the volume of the cavity. This quality factor estimate is supposed to be more accurate than the one before as we do not need to just assume a Lorentzian shape and inaccurately determine the FWHM. However, it again does not allow us to distinguish between the quality factors in vertical and horizontal direction.

Measurement of the Energy and the Losses of the Cavity in Real Space

The third approach is the direct application of equations 2.9 and 2.65

$$Q_\perp = \omega_0 \frac{U}{P_\perp} \text{ and } Q_{||} = \omega_0 \frac{U}{P_{||}}. \tag{2.69}$$

These equations now enable us to determine an estimate for the quality factor at each optical cycle as no further time averaging is included in the calculation.

We therefore on the one hand again need to integrate the energy in the cavity at $t = t_0$ using equation 2.68. On the other hand, we also need to calculate the power dissipating from the cavity. In real space we apply the Poynting theorem, which yields

$$P = \iiint_V \vec{E}\left(\vec{r},t_0\right)\cdot\vec{J}\left(\vec{r},t_0\right) d^3\vec{r} + \oint_{\delta V} \vec{E}\left(\vec{r},t_0\right)\times\vec{H}\left(\vec{r},t_0\right) d^2\vec{r} \tag{2.70}$$

where δV describes the edge of the cavity volume. Assuming possible current densities $\vec{J}$ to be negligible, the power leaving the cavity can be calculated for each surface, where $d^2\vec{r}$ describes the vectorial area element normal to the cavity surface and pointing out of the cavity volume. Therefore this method also enables us to calculate the specific part that each surface contributes to the total quality factor, i.e., we can separate the calculated Q values into $Q_\perp$ and $Q_{||}$.

Measurement of the Energy and the Losses of the Cavity in Momentum Space

Any arbitrary plane parallel to and above the surface of a photonic crystal slab contains all the information about the power flow through this surface and the $\vec{k}$-space distribution of the field. Thus it is possible to calculate the loss in vertical direction by integrating over the leaky field components inside the light-cone, i.e., we can directly calculate $Q_\perp$ in momentum space. We therefore want to apply a formalism familiar from the calculation of far-field antenna radiation as described for example in [34] and applied on photonic crystal cavities in [35].

In general the total time-averaged power radiated into the half-space above the surface A can be written as an integral over the radiated power per unit solid angle $K(\theta,\phi)$ as follows:

$$P = \int_0^{\frac{\pi}{2}}\int_0^{2\pi} \sin\left(\theta\right) K\left(\theta,\phi\right) d\theta d\phi \tag{2.71}$$

Expressing K in terms of the radiation vectors $\vec{N}$ and $\vec{L}$ as described in [35] yields

$$K(\theta,\phi) = \frac{\sqrt{\frac{\mu_0}{\epsilon_0}}}{8\lambda^2}\left(\left|N_\theta + \frac{L_\phi}{\sqrt{\frac{\mu_0}{\epsilon_0}}}\right|^2 + \left|N_\phi - \frac{L_\theta}{\sqrt{\frac{\mu_0}{\epsilon_0}}}\right|^2\right) \tag{2.72}$$

where N_θ, N_ϕ, L_θ and L_ϕ are the radiation vector components in spherical coordinates with respect to a coordinate system centered at the center of the analyzed photonic crystal slab and the z-direction chosen in the direction of vertical loss. Rewriting these equations in Cartesian coordinates and using the fact that the in-plane components of the radiation vectors correspond to the two-dimensional Fourier transforms of the involved in-plane field components at the surface of interest as

$$\begin{aligned} N_x(k_x,k_y) &= -FT_2\left(H_y(x,y)\right)|_{\vec{k}_{||}}, \\ N_y(k_x,k_y) &= FT_2\left(H_x(x,y)\right)|_{\vec{k}_{||}}, \\ L_x(k_x,k_y) &= FT_2\left(E_y(x,y)\right)|_{\vec{k}_{||}} \\ \text{and } L_y(k_x,k_y) &= -FT_2\left(E_x(x,y)\right)|_{\vec{k}_{||}} \end{aligned} \tag{2.73}$$

with $\vec{k}_{||}$ values inside the light cone,

$$\vec{k}_{||} = |\vec{k}|\sin(\theta)\left(\cos(\phi)\hat{x} + \sin(\phi)\hat{y}\right), \tag{2.74}$$

we achieve [29]:

$$K(k_x,k_y) = \frac{\sqrt{\frac{\mu_0}{\epsilon_0}}k_z^2}{2\lambda^2|\vec{k}_{||}|^2}\left(\frac{\epsilon_0}{\mu_0}|FT_2(E_z(x,y))|^2 + |FT_2(H_z(x,y))|^2\right) \tag{2.75}$$

Here the two-dimensional Fourier transform of the function $f(x,y)$ is defined as

$$FT_2\left(f\left(x,y\right)\right) = \iint f\left(x,y\right)e^{i\vec{k}_{||}\vec{r}_{||}}d_xd_y = \iint f\left(x,y\right)e^{i(k_xx+k_yy)}d_xd_y. \tag{2.76}$$

This yields the desired equation for the calculation of the time-averaged vertically dissipating power by integration of the 2D Fourier transform of the E_z and H_z field components over the momentum-space area inside the light-cone:

$$P = \frac{\sqrt{\frac{\mu_0}{\epsilon_0}}}{2\lambda^2|\vec{k}|}\int_{|\vec{k}_{||}|\leq|\vec{k}|}\frac{k_z}{|\vec{k}_{||}|^2}\left(\frac{\epsilon_0}{\mu_0}|FT_2(E_z(x,y))|^2 + |FT_2(H_z(x,y))|^2\right)dk_xdk_y \tag{2.77}$$

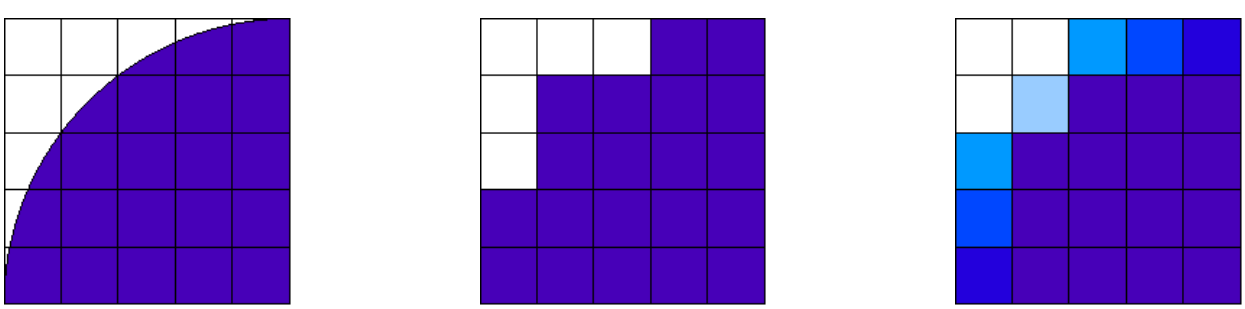

(a) Ideal structure (b) Staircasing (c) Subcell method

Figure 2.12: Illustration of staircasing errors and the principle of a subcell method; the intensity of blue color defines the values of the analyzed refractive index distribution

2.4.4 Subcell Methods

A problem one is concerned with when simulating small dielectric structures is spatial quantization or *staircasing*. The especially for photonic crystals important case of a circular rod is depicted in figure 2.12(a).

Obviously a rectangular grid will never be able to ideally model a circle as we assign one special dielectric index to each Yee cell. Using the refractive indices of the two involved materials leads to the staircased approximation in figure 2.12(b). This coarse grid of two different dielectric materials would lead to artificial numerical reflections on the surface.

One approach to avoid these errors is to assign a special dielectric constant to each $\vec{E}$-field component. The ϵ values are averaged over the hole Yee cell with respect to the assigned field-component. Without loss of generality for a component E_x located at (x_0, y_0, z_0) this is done using the following scheme [32, 36]:

$$(\epsilon_{x,eff})^{-1} = \frac{1}{\Delta x} \int_{x_0-\frac{\Delta x}{2}}^{x_0+\frac{\Delta x}{2}} \left(\frac{\Delta y \Delta z}{\int_{y_0-\frac{\Delta y}{2}}^{y_0+\frac{\Delta y}{2}} \int_{z_0-\frac{\Delta z}{2}}^{z_0+\frac{\Delta z}{2}} \epsilon(x,y,z) dy dz} \right) dx \tag{2.78}$$

A two-dimensional example neglecting the influence of the different field components is illustrated in figure 2.12(c).

3 Preliminary considerations

Before we can begin a parameter analysis and the work on a design of a silicon Raman laser, we first need to specify our later experimental setup and develop a general design idea. This shall be done in this preparatory chapter.

3.1 The Relative Modal Frequency Splitting

As discussed in chapter 2.1, we need to design a microcavity, or in our case an array of coupled microcavities, which posses high quality factors for the pump laser mode ω_p as well as for the Stokes mode ω_s. For silicon, these modes moreover need to fulfill the condition:

$$\Delta f = f_p - f_s = 15.6THz$$

Since we are working with photonic crystals which are generally arbitrarily scalable over almost the whole frequency spectrum, we should be able to achieve this Δf with any structure that offers two frequentially well distinct modes. However, arising from the experimental setup discussed in the following chapter 3.2, a restriction we haven't mentioned yet is to be taken into account:

The pump laser source which is planned to be used is an *erbium doped fiber amplifier (EDFA)* energized by another tunable semiconductor laser. The output of the EDFA is tunable in a range of

$$\begin{aligned} \lambda_{EDFA} = \lambda_p &\in [1.51\mu m; 1.56\mu m] \\ \text{or equivalently } f_p &\in [192.2THz; 198.5THz] \end{aligned} \tag{3.1}$$

which implies a restriction to the possible Stokes mode range of

$$\lambda_s \in [1.639\mu m; 1.698\mu m]\,. \tag{3.2}$$

On the other hand the detector for the Stokes output signal is a modified Agilent 86140B optical spectrum analyzer with a sensitive range of:

$$\lambda_{OSA} = \lambda_s \in [0.60\mu m; 1.70\mu m] \tag{3.3}$$

The intersection of these intervals yields the *effective output operating range*:

$$\begin{aligned} \lambda_s &\in [1.639\mu m; 1.698\mu m] \\ \text{or equivalently } f_s &\in [176.6THz; 182.9THz] \end{aligned} \tag{3.4}$$

Thus being bound to fix Δf as well as to a finite operating range for f_p and keeping in mind the scalability of photonic crystals we define our figure of merit as the *relative modal frequency splitting*:

$$m \equiv \frac{f_p - f_s}{f_p} = \frac{\Delta f}{f_p} \tag{3.5}$$

Applying definition (3.5) on the effectively restricting input range, (3.1) yields our major design goal, the interval of desired relative modal splitting:

$$m_{desired} \in [0.0786; 0.0812] \tag{3.6}$$

3.2 Optical Setup for Possible Experimental Realization

After specializing a design goal in terms of the relative modal splitting, we furthermore need to discuss a possible experimental setup which will allow the later verification of the computational analysis.

Remembering that we intend to examine photonic crystal structures and especially coupled photonic crystal microcavity arrays, in plane pumping of the lasing cavities would on the one hand be difficult to realize because of the underlying photonic band gap structure, but on the other hand also inefficient because of the spatial distribution of the pumped cavities. Instead, we should indeed pump the whole area of the CPCRA by exciting it with a perpendicularly incident lasing beam, which allows a much higher percentage of input power coupling to the cavity array compared to a single cavity. However, this advantage of the CPCRA restricts us to excitation at $\vec{k}_{||} \approx \vec{0}$, that is around the Γ point of the photonic band structure. Moreover, we plan to implement the CPCRA in a silicon slab structured with air holes which generally only possesses a band gap for TE-modes. Thus the upcoming analysis will in principle be restricted to TE modes with a periodic boundary condition in the x-y-plane of $\vec{k}_{||} = \vec{0}$.

As explained in chapter 2.3 we expect to observe a monopole, two dipole and a quadrupole mode as the fundamental resonances in a CPCRA. To really achieve Raman scattering and in the end Raman lasing at low threshold and high output powers, the pump and Stokes modes should possess the right relative frequency splitting, high quality factors, a small modal volume and a high spatial intensity overlap, and should in addition be efficiently pumpable and easily separable. Besides the necessary and unavoidable correct m value, the most critical point of the aforementioned for a pre-analysis decision between different modes is the excitability of the pump mode, which in fact suggests the usage of a dipole mode. Choosing these modes as pump and Stokes modes, respectively, moreover offers two other conveniences:

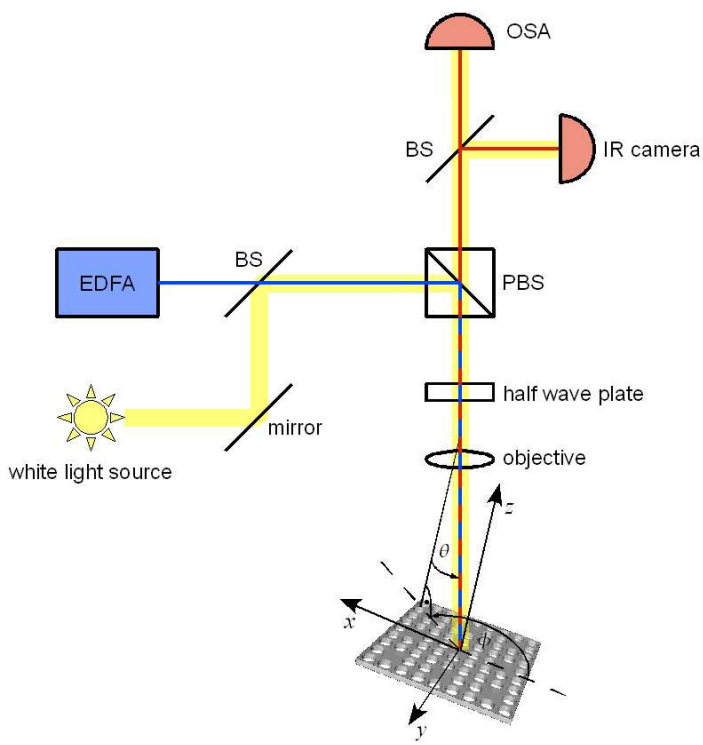

Figure 3.1: Experimental setup proposed for the examination of a two-dimensional CPCRA Raman laser

First we could expect the most precise tunability of the frequency splitting between the modes. This is due to the fact, that in a fourfold rotational symmetric structure at $\vec{k}_{||} = \vec{0}$ we first will observe degenerate modes, which we could then nicely shift in frequency by breaking the symmetry of the photonic crystal square lattice with perturbations in either the x- or the y-direction.

Second, both dipole modes basically possess perpendicular polarizations which makes them comfortably separable, for example by introducing a partial beam splitter.

One possible disadvantage of the dipole modes would be a smaller intensity overlap of the pump and Stokes modes, because most of the E-field intensity is distributed along the central x- and y-axes of the cavity, respectively. Nevertheless we could expect acceptable levels for ξ, as the $\vec{E}_{max}$-values of each mode are both still located in the center of the cavity. Note that this leads to a restriction of a cavity design which indeed possesses dielectric in its center, i.e. the hole radius of the hole inside the cavity is $\frac{r_{cavity}}{a} = 0$.

After weighing these advantages and disadvantages against one another, we chose to focus our analysis especially on the splitting of the x- and y-dipole modes as discussed in chapter 4.

A proposal for the optical setup is depicted in figure 3.1. We source the experiment with an *erbium doped fiber amplifier (EDFA)* at the pump wavelength λ_p. The laser beam is linear polarized in a way that it is reflected by the central *polarizing beam splitter (PBS)* and redirected to the actual lasing cavity array. For the purpose of polarization adjustment we include a $\frac{\lambda}{2}$*-plate*, which allows us to rotate the polarization of the incident beam to fit it to the position of the photonic crystal structure, and of course an *objective* to slightly focus the beam onto the area of the lasing CPCRA. The polarization optics should be configured in such a way that we preferentially just excite the TE pump dipole mode. According to the perpendicular polarization of the cavity dipoles, the scattered Raman beam is also polarized in a direction rotated 90°along the axis of the incident beam. As the $\frac{\lambda}{2}$-plate just annihilates the rotation it added to the incoming beam, the Raman signal hits the partial beam splitter also polarized perpendicular to the pump beam. The signal is therefore transmitted by the PBS, split by a *non-polarizing beam splitter (BS)* and afterwards collected by either an *infrared camera (IR camera)* or by the *optical spectrum analyzer(OSA)* mentioned in section 3.1.

Note that the introduced objective needs to possess a very low numerical aperture because a tight focus would blur the incident $\vec{k}_{||}$-distribution. An as well defined $\vec{k}_{||}$ as possible, however, is necessary to enforce the desired frequency splitting which will be designed for the Γ-point. Nevertheless, adjustment of small fabrication errors could be achieved by mounting the silicon slab on a stage rotatable around the z-direction and a perpendicular in-plane direction. The $\vec{k}_{||}$ value thus varies as:

$$\vec{k}_{||} = \frac{2\pi}{\lambda} \sin(\theta) \left(\cos(\phi)\hat{e_x} + \sin(\phi)\hat{e_y}\right)$$

where ϕ and θ are the angles of the incident beam in-plane with respect to the x-axis of the structure and out-of-plane with respect to the slab-normal, respectively. This possible manipulation of the in plane wavevector leads to a small shift of the x- and y-dipole frequencies as reported in [16] and depicted in 2.9(a) and therefore allows post-fabrication correction of the relative modal splitting.

For the purpose of experimental alignment we moreover added a white light source which propagates along the same path and helps visualizing and controlling the analyzed structure.

4 Relative Modal Frequency Splitting of the Dipole Modes in a Two-Dimensional CPCRA

As discussed in the previous chapter 3.2 the non-degenerate x- and y-dipole modes in a CPCRA are promising candidates for the pump- and Stokes modes of the desired Raman laser. Therefore subsequently a detailed description of the experimental FDTD setup is given, followed by the actual core of this thesis, the analysis of different parameters influencing the relative modal splitting of the CPCRA dipole modes.

4.1 FDTD Simulation Setup

The three-dimensional Finite-Difference Time-Domain method constitutes an important tool for computer-experimental analysis of photonic crystals. To get an understanding of the reaction which the basically degenerate dipole modes show to different manipulations of the CPCRA structure, we process the following operation sequence:

1. Creation of the Structure Files

In a first step we need to create data files which contain the necessary information about the structure that we intend to simulate:

If subsequently not mentioned differently, we define a silicon photonic crystal slab with $n_{Si} = 3.4$ and a slab thickness of $\tilde{d} = 7\Delta$ where Δ is the unit length of the used cubic Yee grid. Because of the later application of even mirror boundary conditions (chapter 2.4.2) in the (z=0)-plane, this $\tilde{d}$ is equivalent to a real slab-thickness of $d = 15\Delta$. On top of the slab we define a volume filled with air of $n_{Air} = 1.0$ and delimited with Mur absorbing boundary conditions at the maximum value of z. To keep the disturbing influences of this boundary relatively small, we choose the thickness of this air volume as $\tilde{d}_{Air} = 80\Delta$. The length of the crystal unit cell in z-direction thus yields $n_z = \tilde{d} + \tilde{d}_{Air} = 87\Delta$.

In the x-y-plane the size of this unit cell depends on three parameters: The lattice constant a of the underlying square lattice which we want to choose as $a = 20\Delta$, the number of columns l_x of square lattice holes in the x-direction and the number of rows l_y of square lattice holes in the y-direction. The latter two values are determined by the number of layers between two adjacent cavities $\tilde{l}_x = l_x - 1$ and $\tilde{l}_y = l_y - 1$ which are the equivalent parameters used in [16]. Thus the length of the unit cell is determined by the dimensions $n_x = l_x a$ and $n_y = l_y a$ in x- and y-directions, respectively.

The slab itself, of course, contains holes of different shape and size. The details of such parameters as r for circular holes or r_x and r_y for elliptical holes will be discussed in chapter 4.2. Note that because of the scalability of the Maxwell equations the characteristics of the structure are determined just by its proportions. We therefore subsequently will refer to these parameters in the fractions $\frac{d}{a}$ and $\frac{r}{a}$ rather than in terms of the absolute values of d and r.

Besides the structure, in this first step of the FDTD simulation we also need to define the incident field. Keeping in mind the preliminary considerations of chapter 3, we excite temporally with a δ_t-pulse in order to excite all possible mode energies. Spatially, this pulse contains just B_z components at the center of the slab and thus supports the applied TE-mirror boundary conditions. The in-plane spatial field pattern equals either a slightly off-centered Gaussian distribution or one of the dipole modes. The first is useful for the

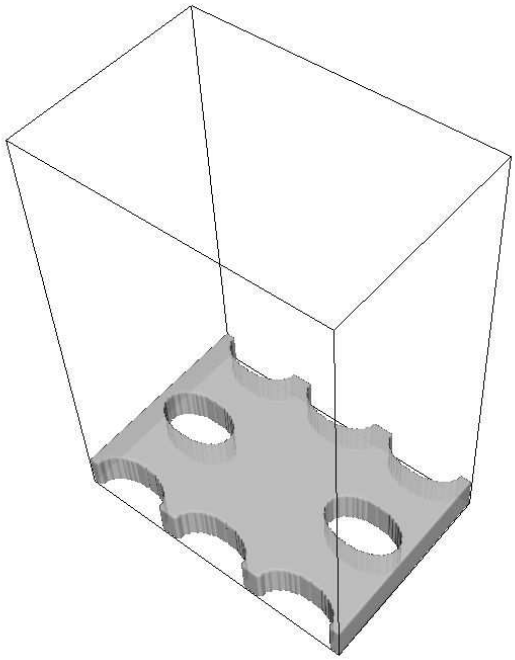

Figure 4.1: Three dimensional plot of a photonic crystal slab with $l_x = 2$, $l_y = 3$, $a = 60\Delta$, $\frac{d}{a} = 0.65$ and elliptical holes with $\frac{r_x}{a} = 0.25$ and $\frac{r_y}{a} = 0.4$

calculation of band-diagrams or a general analysis because all possible modes are excited, while the latter is preferred for the analysis of the reaction of the dipole modes to different manipulations. This is due to the fact that an incident dipole-like field just excites modes also showing the same non-orthogonal dipole symmetry, which makes the spectral identification of the dipole modes much easier.

The creation of the structure and the definition of the desired parameter setup are controlled and adjusted by TCL scripts which can be found in appendix A.1. These scripts call the *"fabrication"* source which is written in *C*.

The structure as well as the field files are saved on the one hand in ASCII format readable by the FDTD algorithm, on the other hand also in a vtk-file which is necessary to create three-dimensional plots of the structures and fields for control purposes as discussed in the next section. An example of the generated structures its presented in figure 4.1.

2. Three-Dimensional Plotting of the Fabricated Structures

A helpful tool for error detection in the design of different structures is visualization. To plot the written structures we again use TCL scripts, but this time to control *The Visualization ToolKit (VTK)* [37], an open source software system for three-dimensional computer graphics. One result of these structure plots is depicted in figure (4.1), the controlling TCL script is attached in appendix A.2.

3. FDTD Time Evolution

After preparing all the necessary structural data the actual FDTD simulation is started. The setup of each simulation is therefore again implemented in a TCL script (appendix A.3) which then calls the simulation algorithms. The FDTD algorithm itself is written in *C* by Brian D'Urso and Jelena Vučković. It basically uses the second-order accurate Yee algorithm described in chapter 2.4.

In the setup files we first need to define the desired boundary conditions: As mentioned previously we apply absorbing Mur boundary conditions in the (z=n_z)-plane, while in the (z=0)-plane we simulate the lower half of our structure by application of mirror boundary conditions. To select the TE-modes, this mirror boundary is chosen as even. In the x-y-plane we want to have an infinite array of coupled cavities, which requires the use of periodic Bloch boundary conditions at $x = 0$, $x = n_x$, $y = 0$ and $y = n_y$. To implement the fact that we want to work at the Γ-point we moreover need to define the in plane wavevector as $\vec{k_{||}} = \vec{0}$.

The Yee grid is chosen as $\Delta x = \Delta y = \Delta z = \Delta$ and a subcell method is applied to reduce the influences of discretized material boundaries. Applying the standard units $\Delta \equiv 1$ and $c_0 \equiv 1$ we select a timestep of $\Delta t = 0.55$ to satisfy the Courant stability criterium (2.52):

$$S = \frac{c_0 \Delta t}{\Delta} = 0.55 < \frac{1}{\sqrt{3}} \tag{4.1}$$

The easiest way to collect the data for later analysis of the FDTD results would be to save the calculated field at each point in time, which would allow an analysis in space at every timestep as well as in time over the whole structure. Unfortunately the size of a field file at every timestep tends to be of the order of 100MB, which makes it impractical and with todays storage sizes even impossible to keep a few thousands of them. We instead keep two different types of data for different types of interpretation:

For an analysis in time- and frequency-space we store the field values at a spatial array of $n_{points} \times n_{points}$ points after each timestep $\Delta T = 1.1$. As the field at any non-high-symmetry point should contain at least small components of all oscillating frequencies, we can easily analyze the frequency distribution of the grid, although the intensity values at each frequency of course depend on the points of collection. However, we should always have chosen at least one point inside the cavity to get a signal of higher intensity and thus a better signal to noise ratio in the spectrum. The overall running length of the simulation should then be defined by a value $T = 2^m \Delta T$ where T is an integer m power of 2 multiplied by ΔT to achieve the shortest calculation times of the subsequent *fast Fourier transform (FFT)*.

If instead we want to analyze the spatial distribution of the $\vec{B}$ and $\vec{E}$ fields, we save the full resulting fields after the last timestep. As the latest result adjusted itself most accuratly to the characteristics of the cavity array, this last field is a good basis for the filtering of single modes in step 5 which then allows an analysis in $\vec{k_{||}}$-space.

4. Spectral Analysis of the Time Evolution Results

The spectral analysis is based on the *Fast Fourier Transform (FFT)* algorithm implemented in *MATLAB*®. After importing the data out of the time-evolution files into matrices, each field component is Fourier transformed according to [38]:

$$X(k) = \sum_{n=1}^{N} x(n) e^{-i2\pi \frac{(k-1)(n-1)}{N}} \tag{4.2}$$

Here n and k mark the indices of the field components in time and frequency space, respectively, while N equals the number of calculated timesteps which should be a power of two:

$$N = 2^m \tag{4.3}$$

The properties of the discrete Fourier transform thus yield a frequency resolution of

$$\Delta f = \frac{1}{N\Delta T}. \tag{4.4}$$

Here N equals the number and ΔT equals the width of the timesteps. To minimize the effects of the intensity filtering which we perform by just observing a small number of grid points, we usually sum up all the field components to get a spectrum of an abstract intensity. One of these plots with a frequency resolution of $\Delta_{\frac{a}{\lambda}} \approx 0.0011$ is depicted for example in figure 5.4, the m-file including a method to detect the peaks above a specified threshold is attached in appendix A.4.

5. Filtering Modes of Interest

Possessing a detailed frequency spectrum, we need to identify which two of the several peaks that we observe correspond to the desired dipole modes. Therefore it is necessary to gain the spatial field distribution of the peak of interest, which we can achieve by filtering out any other disturbing temporal frequencies.

Assume we want to identify the field distribution of a mode at frequency ω_{test}. One way to do this would be to source the final broad temporal frequency response field distribution of the examined structure with the specified temporal frequency ω_{test} over a long period of time. As the width of the time window over which we source would determine the frequential width of the source, a long period of sourcing would lead to a stable and amplified mode pattern at ω_{test}, while other mode components can be expected to be several orders of magnitude smaller.

However, in our simulations we want to follow a different approach: The ideal way to visualize the modal pattern at ω_{test} would, of course, be a simple application of a small bandwidth filter in frequency space on the resulting broad temporal frequency response field distribution. An inverse Fourier transform would then directly yield the desired result. However, as described in the previous section, this would require a priori knowledge of the Fourier transform of the whole spatial pattern, which would lead to computational memory demands of $O(n_x \cdot n_y \cdot n_z \cdot N)$, where n_i is the number of grid points of the structure in direction i and N is the number of timesteps of the simulation. Moreover, all of this massive amount of data needs to be processed during the FFT, which would yield considerably elongated computation times.

A way out of this dilemma is the *convolution theorem*, which states that multiplication in Fourier space and convolution in time space are equivalent operations [38]:

$$x_n * y_n \circ\!\!-\!\!\bullet X_k \cdot Y_k \tag{4.5}$$

Therefore, instead of performing a full Fourier transform with subsequent multiplication in Fourier space and final inverse Fourier transform, we here want to apply a frequency selective filter by convoluting with the Fourier transform of the desired filter function in *time* space.

Implementing this convolution as a running calculation algorithm, we can moreover reduce the necessary amount of memory to $O(n_x \cdot n_y \cdot n_z)$: While again performing the simulation from step 3 to achieve the broad temporal frequency response field distribution, we have every field distribution at an arbitrary point in time in the computational memory for a short amount of time. At each of these points, we can use each field distribution to perform all the necessary multiplications and summation with which it contributes to the overall convolution result as

$$x_n * y_n = \sum_{m=0}^{N-1} x_m y_{n-m} \tag{4.6}$$

For implementation in the simulation process, however, a second simulation is necessary as we need the a priori knowledge of ω_{test} before running the filtering convolution.

To achieve a small bandwidth, we of course still need to convolute with a long filter time series. Moreover, by choosing a bandwidth on the order of the frequency resolution Δf, we run the risk of actually filtering

out the mode of interest, as in a discrete spectrum ω_{test} is just an approximation of the real peak frequency. The temporal filter bandwidth is given as

$$\delta_{\frac{a}{\lambda}} = 2^{\zeta-1}. \tag{4.7}$$

where ζ is a parameter of the filter function which we further want to refer to as the *filter level*.

There are now two ways to further improve the accuracy of the resulting field distribution:

First, we can improve the initial field guess and concurrently increase the filter level. By reusing the resulting field of a former finished filtering as an exciting field for a short time evolution and by subsequent refiltering of this evolved field at the same center frequency with a set of filters up to a higher level we achieve an iterative process with increasing quality in the results. A demonstrative example of the application of such iterative filtering is given in chapter 5 where we need a high frequency resolution to distinguish two modes with a low free spectral range. This filtering technique is also the one used for most calculations in this thesis.

However, we could also possibly improve the filter results by achieving better center frequency estimates. As described in [32], knowledge of the mode pattern of an eigenfunction can be used to recalculate the observed eigenstate frequency as

$$\left(\frac{\omega}{c_0}\right)^2 = \frac{\int_{V_{unit}} \frac{1}{\mu_r} \left|\nabla \times \vec{E} - i\vec{k} \times \vec{E}\right|^2 dV}{\int_{V_{unit}} \epsilon_r \left|\vec{E}\right|^2 dV} = \frac{\int_{V_{unit}} \frac{1}{\epsilon_r} \left|\nabla \times \vec{H} - i\vec{k} \times \vec{H}\right|^2 dV}{\int_{V_{unit}} \mu_r \left|\vec{H}\right|^2 dV} \tag{4.8}$$

Reusing this ω as a new center frequency in the above described iterative process allows further improvement of the resulting filtered field distribution. It shall be mentioned that especially the convergence of the second iteration is not guaranteed as for a good new ω-estimate, of course a good initial fields pattern estimate is necessary.

6. Spatial Analysis of the Time Evolution Results

To visualize the filtered field distributions we use a Matlab-script based on a program by Marko Loncar (appendix A.6). This imports the filtered field files into Matlab-matrices and prepares the fields together with the underlying structure for plottting. We can thus easily visualize the spatial distributions of any field component B_x, B_y, B_z, E_x, E_y and E_z or the amplitudes $B_a = |B_x|^2 + |B_y|^2 + |B_z|^2$ and $E_a = |E_x|^2 + |E_y|^2 + |E_z|^2$ in any desired x-y-plane, but usually at the center of the slab $z = 0$.

4.2 Analysis of Different Parameters

The unit cell of a CPCRA slab with a square lattice in the x-y-plane possesses four-fold rotational symmetry with respect to the z-axis in the center of the missing cavity hole. If we preserve this symmetry by working at the Γ-point, i.e., $\vec{k}_{||} = \vec{0}$, we will observe degenerate x- and y-dipole modes, simply because there is no difference at all between the x- and the y-directions (see chapter 2.3). However, we want to break this degeneracy to achieve a frequency splitting of the two dipole modes, which conversely requires the destruction of the four-fold rotational symmetry of the arrangement. The analysis of different methods to achieve this and a proposal for other possible parameters will be given in this chapter.

4.2.1 Shape of the Air Holes

The first parameter which we want to analyze is the shape of the holes. While preserving the basic square lattice array ($a_x = a_y = 20\Delta$) we induce asymmetry by detuning the holes differently in x- and in y-direction. An interesting candidate for such detuning would be an elliptical hole shape. However, although we are able

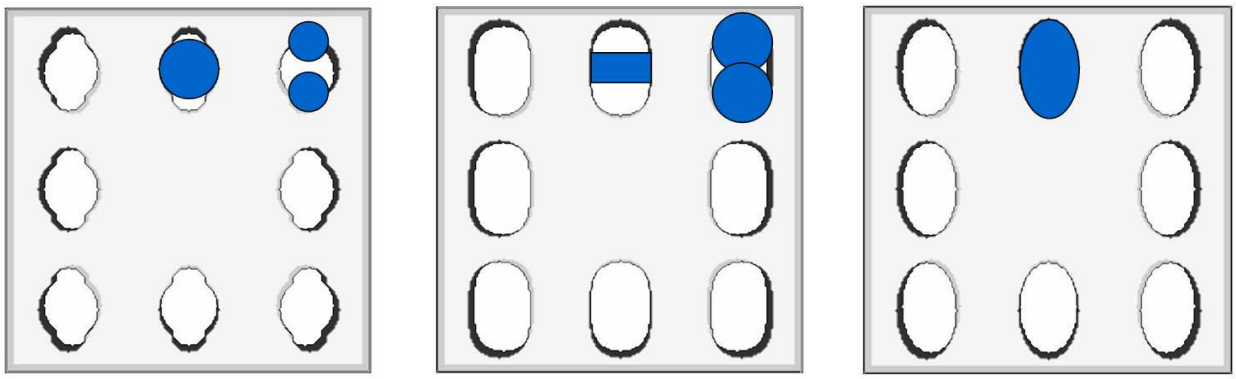

(a) Circle-approximation (b) Stadium-approximation (c) Ellipses

Figure 4.2: *vtk* plots of two lattices of different ellipsis-approximations and a real elliptical lattice, all written with $a = 60\Delta$ and $l_x = l_y = 3$

to write ellipses in silicon, we first had been missing a function to write structure files with elliptical holes, which made some FDTD approximations necessary. Note that this problem was later resolved by adjustment of the used C-source, so the following subsection is not necessary for the understanding of our final results, but of importance for the development of our methods of analysis.

Approximation of Elliptical Holes

There are two ways in which we tried to approximate an elliptical shape:

The first is depicted in figure 4.2(a) and will be referred to as *circle-approximation*. Every hole consist of a centered circle with the radius r_{center} and two surrounding circles. These two additional circles are shifted in the $+y$- and $-y$-directions by a value s_{circle}. To smooth the resulting shape they are also decreased in radius proportional to the amount of shifting:

$$r_{surrounding} = r_{center} - \left\lceil \frac{s_{circle}}{2} \right\rceil \tag{4.9}$$

The second approach can be described as a *stadium-approximation* (figure 4.2(b)): A centered rectangle of the dimensions s_x and s_y is surrounded by two semi circles with a radius $r_{semi} = \frac{s_x}{2}$ which are shifted in the $+y$- and $-y$-directions by $s_{stadium} = \frac{s_y}{2}$, altogether forming an oval of a stadium-like shape. For comparison, a lattice of ideally elliptical holes is depicted in figure 4.2(c), too.

For both lattice approximations we performed the simulation steps of chapter 4.1 with the evolution time $T = 9012$, a number of collection points of $n_{collection} = 9$ and excitation with a Gaussian spatial field distribution. The evolution time T yields a normalized frequency resolution of

$$\Delta_{\frac{a}{\lambda}} = \frac{a\Delta f}{c_0} = \frac{20}{N\Delta T} = \frac{20}{9012} \approx 0.002219 \tag{4.10}$$

for a normalized value of $c_0 = 1$.

The analyzed parameter spectrum for the circle-approximation ranged from the circular $\frac{s_{circle,min}}{a} = 0$ to a maximum value of $\frac{s_{circle,max}}{a} = 0.3$ in steps of $\Delta\frac{s_{circle}}{a} = 0.05$, while the radius of the central circle was kept constant at $\frac{r_{center}}{a} = 0.3$. For the stadium-approximation we varied the shift of the semicircles in the interval $\frac{s_{stadium}}{a} \in [0; 0.2]$ while also using a $\Delta\frac{s_{stadium}}{a} = 0.05$ and keeping $\frac{r_{semi}}{a} = 0.3$ constant. The number

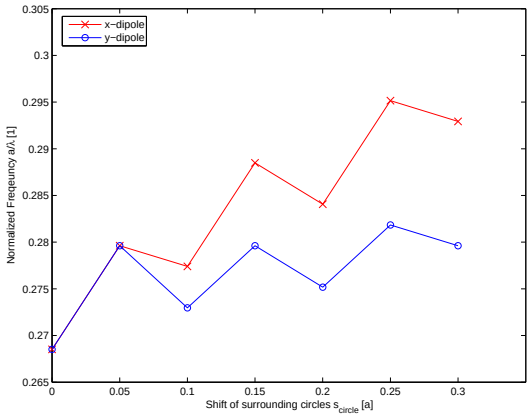

(a) Normalized frequency $\frac{a}{\lambda}$ for circle-approximation

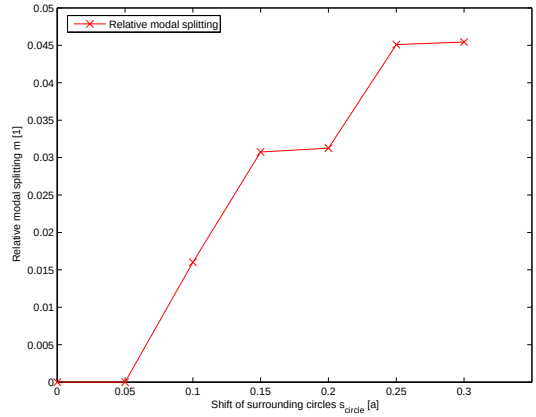

(b) Relative modal splitting m for circle-approximation

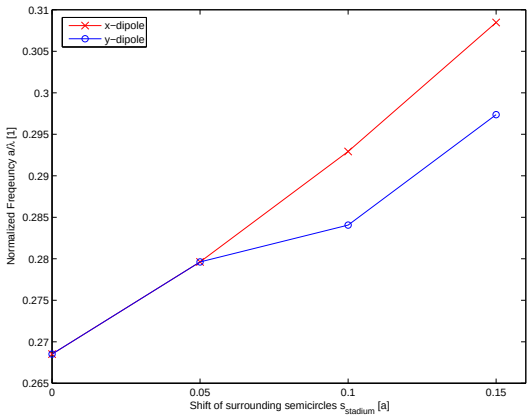

(c) Normalized frequenciy $\frac{a}{\lambda}$ for stadium-approximation

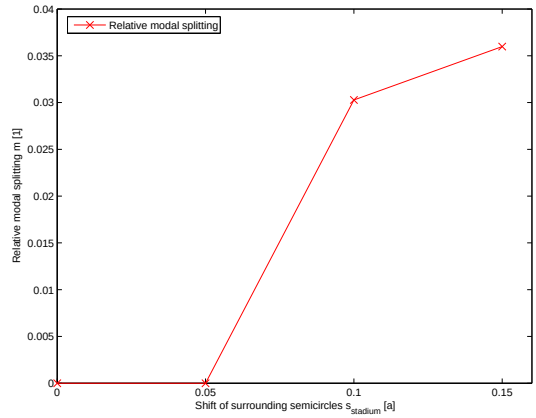

(d) Relative modal splitting m for stadium-approximation

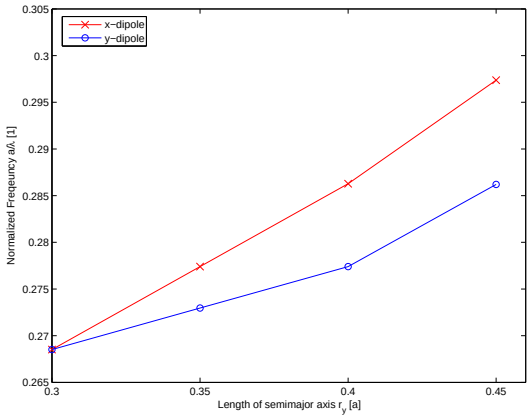

(e) Normalized frequency $\frac{a}{\lambda}$ for elliptical holes with $\frac{r_x}{a} = 0.3$

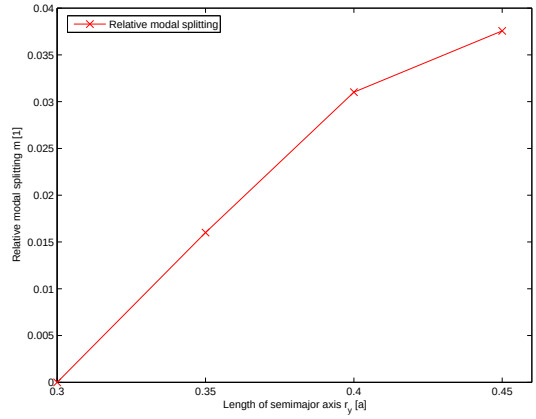

(f) Relative modal splitting m for elliptical holes with $\frac{r_x}{a} = 0.3$

Figure 4.3: Normalized frequencies and relative modal splitting of the x- and y- dipoles versus the eccentricity in a CPCRA with $l_x = l_y = 3$

of layers of the unit cell ranges in both cases from $l_{x,min} = 2$ to $l_{x,max} = 4$ and from $l_{y,min} = 2$ to $l_{y,max} = 4$, respectively.

After we had become able to simulate real elliptical holes we processed the same simulations with an equal parameter setup for the elliptical lattice. The ellipse's semiminor axis has in this case been kept constant at $\frac{r_x}{a} = 0.3$ while the semimajor axis varies from $\frac{r_y,min}{a} = 0.3$ to $\frac{r_y,max}{a} = 0.45$ in steps of $\Delta\frac{r_y}{a} = 0.05$.

The behaviour of the normalized dipole frequencies as well as the reaction of the relative modal splittings m is depicted in figure 4.3 for $l_x = l_y = 3$.

Obviously in all three cases we start with the same four-fold rotational symmetric square lattice of circular holes ($\frac{r}{a} = 0.3$) which exhibit the existence of degenerate dipole modes. By detuning the hole shape, generally both modes are pushed to higher frequencies with increasing hole size, and we moreover observe a trend of the x-dipole mode to be pushed to higher frequencies than the y-dipole. This different intensity of reaction gives rise to a relative modal splitting up to values of $m_{max,circle} = 0.045$, $m_{max,stadium} = 0.036$ and $m_{max,ellipses} = 0.037$ in the cases of circle-approximation, stadium-approximation and the elliptical lattice, respectively. Note that the maximum values of the three different hole shapes are roughly comparable as all of them possess a hole radius in x of $\frac{r_x}{a} = 0.3$ and in y of $\frac{r_y}{a} = 0.45$, where the latter is the maximum multiple of 0.05 which preserves a compound structure of the lattice.

The general increase in oscillation energy of both modes can be easily explained with the perturbation theoretical approach of chapter 2.2.3: as the average amount of air is increased, a higher percentage of the displacement field is forced to stay in volumes of low dielectric, which plausibly explains the existence of a rise in energy and thus also in frequency. However, the difference in reaction intensity of the two dipoles is of fundamental importance for the design of a CPCRA Raman laser and will be discussed in detail with regard to the elliptical lattice in chapter 4.2.1.

Besides these equal characteristics of the different approximations, we can also detect distinctions: While the frequency trend of the circle-approximation shows an odd-even-characteristic which is due to the use of the *ceiling*-function in equation 4.9, the matching of the stadium-approximation with the real elliptical lattice is except for $\frac{s_{stadium}}{a} = 0.05$ pretty good. We also detect a difference not only in the development of the relative splittings, but in its absolute maximum values as mentioned above. Moreover, one should note that the absolute normalized frequency values differ from case to case.

If we had to decide for one of these lattice types we would preferably choose the elliptical lattice because it exhibits the smoothest and therefore most controllable reaction of all the three lattice types, although its maximum achievable splitting is worse than that of the circle-approximation. We would also suspect that because of its most circle-like and smoothest shape it possesses the largest remaining basic band-gap of all the structures, particularly if we tend to use high eccentricities. However, especially the stadium-approximation, but also the circle-approximation would be pretty difficult to fabricate, and because we are actually able to write real elliptical lattices in the real fabrication as well as for FDTD simulations, we will from now on focus exclusively on this hole shape.

Change of the Initial Field Distribution

A major problem with the simulations of 4.2.1 was the fact that because of frequency overlap of different modes the dipole modes were often pretty difficult to identify, which partly led to incomplete and dissatisfactory results. Figure 4.4(a) shows the spectrum of one of the simulations intended to analyze the reaction of the dipole modes to variations of l_x, l_y, $\frac{r_x}{a}$ and $\frac{r_y}{a}$. As we initialize our simulations with a slightly off-centered Gaussian field distribution, almost every possible mode should be excited, which in the case of figure 4.4(a) leads to an overlap of the desired x-dipole with another adjacent mode with an obviously higher intensity. Without a priori knowledge of the normalized frequency of the x-dipole, a detection of that mode becomes rather difficult. Moreover, even without such a modal overlap we still excite a huge amount of modes which would all have to be filtered to detect their modal profile and identify the dipoles.

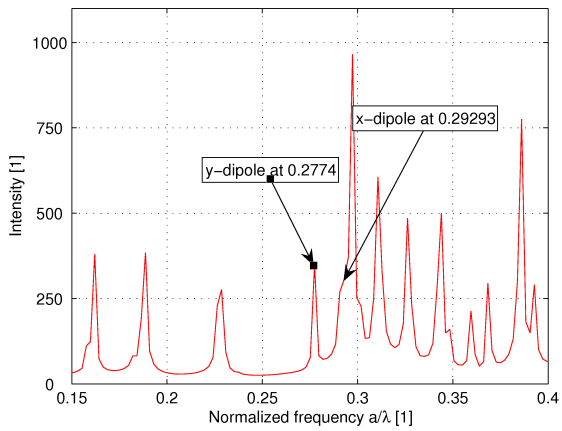

(a) Excitation with Gaussian

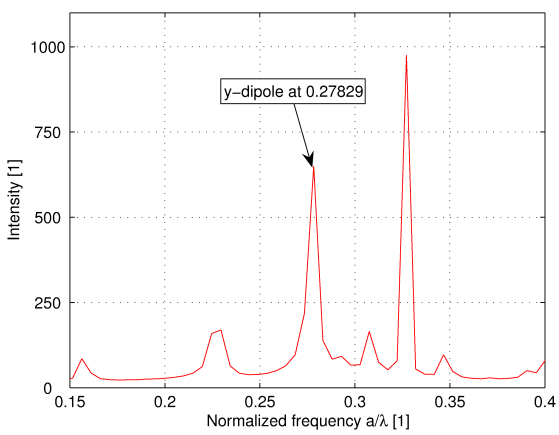

(b) Excitation with y-dipole

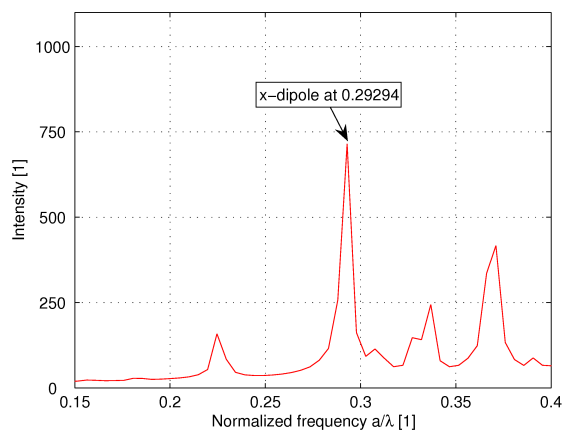

(c) Excitation with x-dipole

Figure 4.4: Spectra of a CPCRA with $l_x = 3$, $l_y = 3$, $\frac{r_x}{a} = 0.25$ and $\frac{r_y}{a} = 0.45$; note that the difference in frequency of the peaks in (a) compared to (b) and (c) is due to different lengths T of the time evolutions

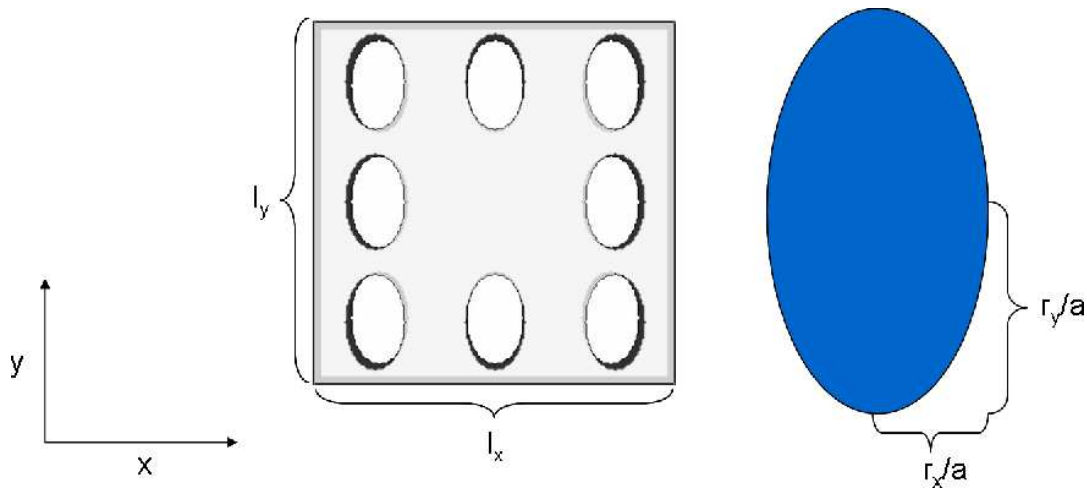

Figure 4.5: Visualization of the terminology preferred by the author: we arbitrarily choose a two-dimensional Cartesian coordinate system of x- and y-directions; the values l_x and l_y describe the numbers of unit cell layers of thickness a in each direction; the parameters $\frac{r_x}{a}$ and $\frac{r_y}{a}$ correspond to the two semiaxes of the elliptical holes

As our first goal is just the examination of the frequency shift of the dipole modes, we can overcome this problem by exciting with a field profile of dipole symmetry. As explained in chapter 4.1, we won't energize any modes orthogonal to the initial field, which should make the identification of the spectral dipole peaks much easier. Figures 4.4(b) and 4.4(c) show the spectra of the same structure simulated in 4.4(a), but this time excited with x- and y-dipole distributions, respectively. Here we achieve a much smaller number of more intense and sharp peaks, of course at the cost of twice the amount of time-evolution, but to the benefit of a crucially reduced amount of necessary filtering.

Note that the difference in the absolute values of normalized frequencies in figure 4.4 results from a reduced time evolution length of the dipole-excited spectra. If not quoted differently, we subsequently evolved the fields for $T = 4096$, resulting in a frequency resolution of

$$\delta_{\frac{a}{\lambda}} = 0.00488. \tag{4.11}$$

Relative Modal Splitting in a CPCRA of Elliptical Holes

After the preliminary examination of different ellipse approximations and initial fields, we finally started to analyze structures with ideal elliptical holes using dipole excitations. For convenience, the used CPCRA terminology is visualized in figure 4.5. Note that we have arbitrarily chosen our coordinate system and we should from now on be careful not to do redundant analysis due to implicit symmetries hidden under the arbitrary choice of x and y.

We would suspect a structure of high eccentricity to possess a strong modal splitting because of a relatively strong perturbation of the former four-fold rotational symmetry. As the primary goal is to engineer a structure of sufficient relative modal splitting, i.e.,

$$m \in [0.0786; 0.0812] \tag{4.12}$$

as proposed in equation 3.6, but the results of chapter 4.2.1 predict a maximum value of $m_{max} = 0.045$, we

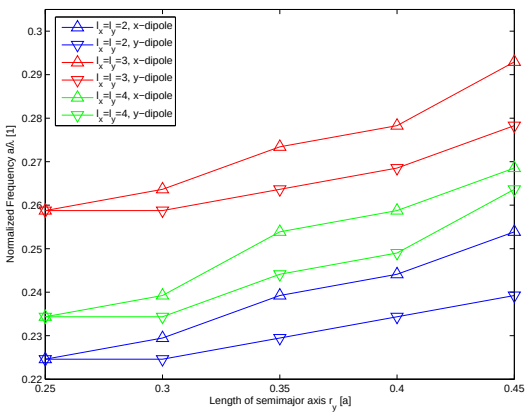

(a) Normalized frequency $\frac{a}{\lambda}$

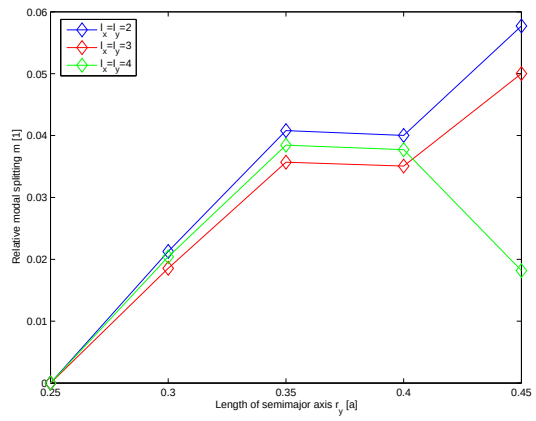

(b) Relative modal splitting m

Figure 4.6: Normalized frequencies and relative modal splitting of the x- and y- dipoles versus the length of the semimajor axis $\frac{r_y}{a}$ in a CPCRA with $\frac{r_x}{a} = 0.25$ and a symmetric arrangement of the cavities, i.e., $l_x = l_y$

will in the following analysis focus on a basic value of $\frac{r_x}{a} = 0.25$, which lets us examine eccentricities up to

$$e_{max} = \sqrt{1 - \frac{\left(\frac{r_{x,max}}{a}\right)^2}{\left(\frac{r_{y,max}}{a}\right)^2}} = \sqrt{1 - \frac{r_{x,max}^2}{r_{y,max}^2}} = 0.8315 \tag{4.13}$$

by varying the semimajor axis up to its maximum value of $\frac{r_{y,max}}{a} = 0.45$.

Performing the FDTD simulation steps described in chapter 4.1 for a square-shaped unit cell, i.e., $l_x = l_y$, yields the dipole mode frequency distribution dependence in figure 4.6(a). The observations of chapter 4.2.1 are basically confirmed: An increase in $\frac{r_{y,max}}{a}$ generally pushes both dipole modes to higher frequencies, but has a much more intense effect on the frequency of the x-dipole. Thus figure 4.6(b) verifies the expectation of an accurately tunable splitting, here in a range of

$$m \in [0; 0.058]\,. \tag{4.14}$$

To understand the origin of the different behaviours of the two dipoles, we need to have a closer look at the spatial mode profiles depicted in figure 4.7. The x- and the y- dipole modes oscillate predominantly in the y- and x-directions, respectively. Moreover, a change in $\frac{r_y}{a}$ primarily affects the structure of the lattice in the y-z-plane, but leaves the structure in the x-z-plane unchanged. Thus, we would expect an increase in $\frac{r_y}{a}$ to primarily shift the frequency of the x-dipole to higher energies. This is exactly the result reported in figure 4.6(a). Note that, of course, both of the modes see an effective increase in the average present amount of air, for example at the coupling antinodes between the cavities, which explains the general energy increase of both of the modes. The difference in frequencies for different l_x and l_y of the cavities is due to the spatial distribution of the nodes and antinodes and will be discussed in chapter 4.2.2.

Unfortunately, although better than our former results, the reported range of relative modal splitting (equation 4.14) is still not sufficient for Raman lasing at telecommunication wavelengths. To step into the desired range of m-values we need to introduce additional asymmetries. One approach is to asymmetrically vary the number of layers between the cavities. Although this also will be discussed in detail in chapter 4.2.2, we here want to qualitatively analyze the interaction of both manipulations.

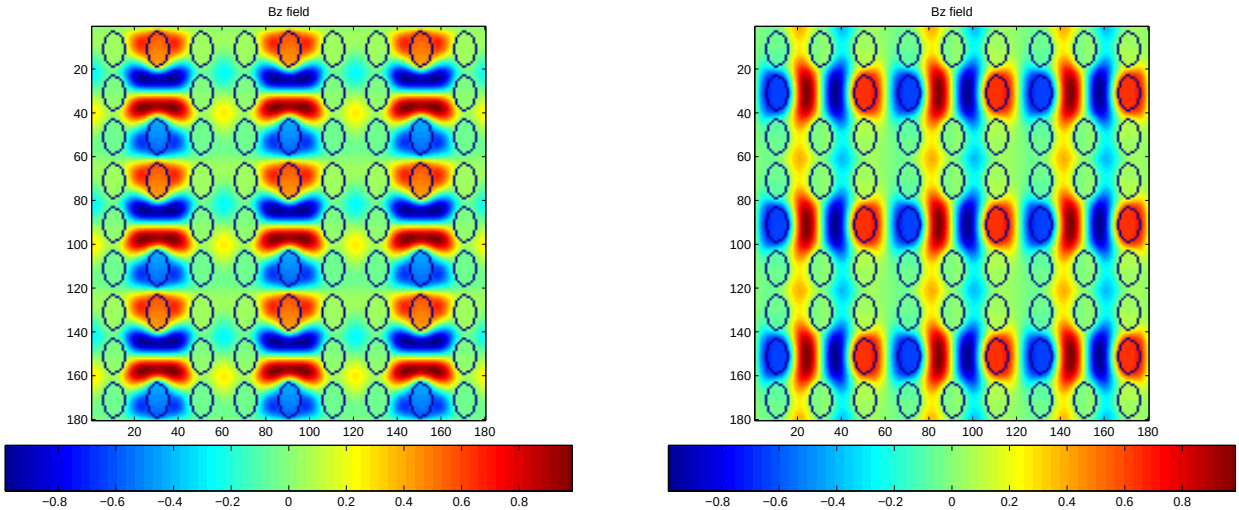

(a) x-dipole (b) y-dipole

Figure 4.7: B_z-fields of the dipole modes for $l_x = l_y = 3$, $\frac{r_x}{a} = 0.25$ and $\frac{r_y}{a} = 0.4$ in normalized units at the center of the photonic crystal slab

Processing the same simulations as before, but this time with differing numbers of layers of the unit cell in x- and y-direction, we achieve a basic difference in the frequencies of the x- and y-dipoles even for a circular CPCRA, referred to as *basic barrier splitting*. We here want to focus on the interaction of the additionally introduced eccentricity of the lattice holes with this basic splitting. One can see in figure 4.8, for example by focusing on the case of $l_x = 2$ and $l_y = 3$ depicted as blue lines in figures 4.8(a) and 4.8(b), that additional eccentricity induces additional relative modal splitting. In this example the x-dipole mode contains higher oscillation energy than the y-dipole mode already in the circular structure, and by increasing $\frac{r_y}{a}$ its frequency is pushed to even higher values, the two types of perturbations interact *constructively*.

However, if we focus on the opposite case of $l_x = 3$ and $l_y = 2$ (red lines), we report a decrease in relative modal splitting due to an increase in $\frac{r_y}{a}$. Of course, this is a result of the inverse exposition of this circular lattice: In the case of $l_x = 3$ and $l_y = 2$ we start with a high-energy y-dipole compared to a low-energy x-dipole. Nevertheless, an increase in $\frac{r_y}{a}$ still affects the x-dipole more than our y-dipole, which leads to a *destructive* interaction of the layer-induced and the eccentricity-induced modal splittings. Note that by using the implicit symmetries, another way to interpret our results is, of course, that in the case of $l_x = 2$ and $l_y = 3$ we could achieve the same destructive behaviour by choosing $\frac{r_x}{a}$ as the semimajor axis instead of $\frac{r_y}{a}$; the absolute labeling of x and y remains artificial. As a rule of thumb we can derive from figure 4.8 that by introducing additional elliptical asymmetry into a lattice of already asymmetric values of l_x and l_y we can detune the basic barrier-splitting in a range of approximately

$$\Delta m_{ellipse} \in [0; 0.05] \tag{4.15}$$

This appears to be a rather important result when we have a closer look at the range of the basic barrier splitting: this splitting increases up to values of $m_{barrier,max} = 0.132$ for $l_y = 2$ and $l_2 = 3$ and circular holes, as one can read from figure 4.8(b). Unfortunately, this splitting values are quantized, i.e., we can just tune l_x and l_x in the integer range $\mathbb{N}\setminus\{1\}$. However, the lengths of the ellipse semiaxes, although here simulated in steps of $\Delta\frac{r_i}{a} = 0.05$, are actually arbitrarily tunable. Now keeping in mind that both m values

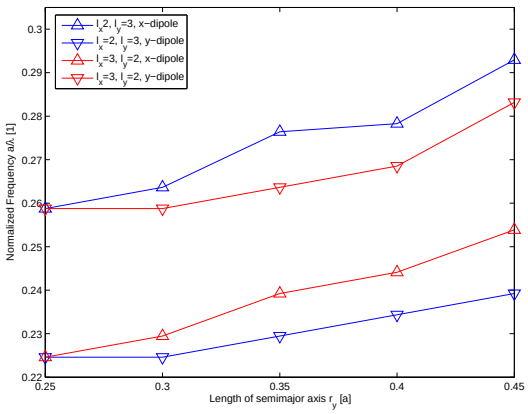

(a) Normalized frequency $\frac{a}{\lambda}$ for $l_1 = 2$ and $l_2 = 3$

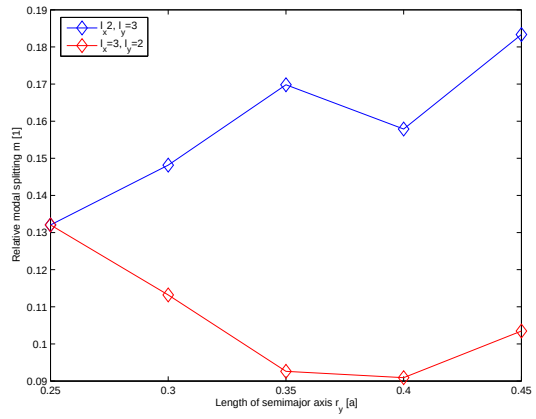

(b) Relative modal splitting m for $l_1 = 2$ and $l_2 = 3$

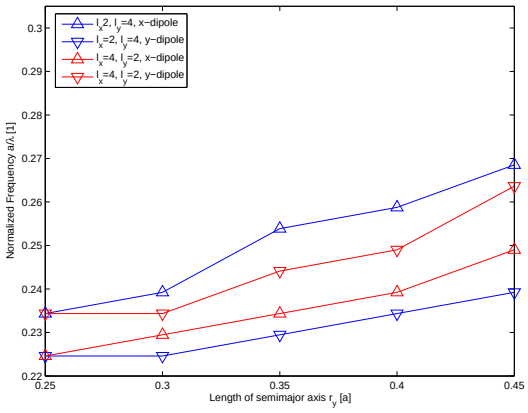

(c) Normalized frequency $\frac{a}{\lambda}$ for $l_1 = 2$ and $l_2 = 4$

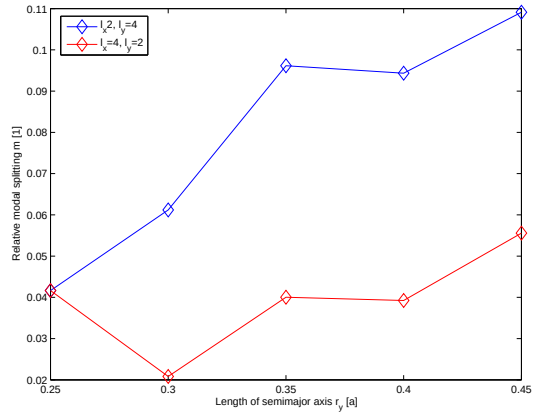

(d) Relative modal splitting m for $l_1 = 2$ and $l_2 = 4$

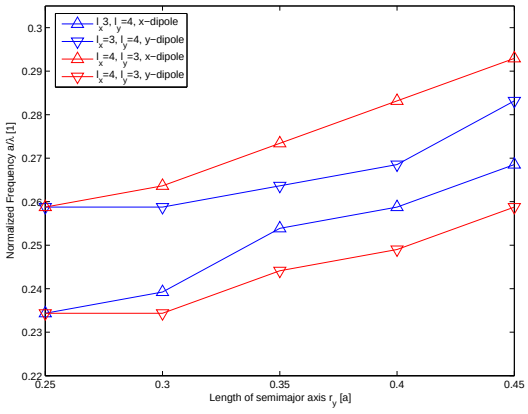

(e) Normalized frequency $\frac{a}{\lambda}$ for $l_1 = 3$ and $l_2 = 4$

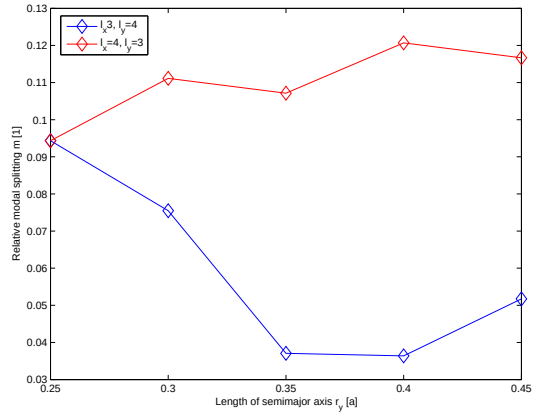

(f) Relative modal splitting m for $l_1 = 3$ and $l_2 = 4$

Figure 4.8: Normalized frequencies and relative modal splitting of the x- and y- dipoles versus the length of the semimajor axis $\frac{r_y}{a}$ in a CPCRA with $\frac{r_x}{a} = 0.25$ and asymmetric arrangements of the cavities, i.e., $l_x \neq l_y$

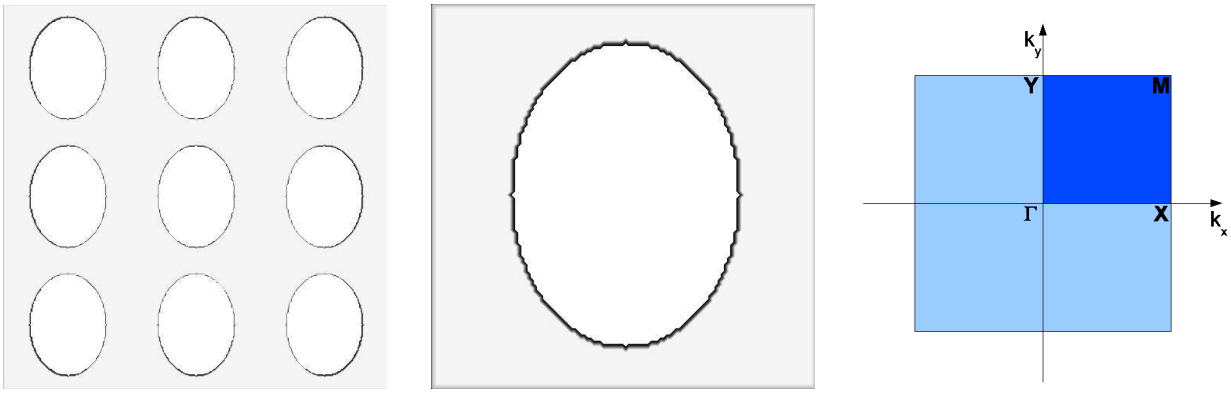

(a) Lattice section (dimensions $3a \times 3a$)

(b) Unit cell (dimensions $a \times a$)

(c) Brillouin zone (light blue) and irreducible Brillouin zone (dark blue)

Figure 4.9: Visualization of the square lattice with elliptical holes, its unit cell and the extended irreducible Brillouin zone due to a reduction from four-fold to two-fold rotational symmetry; Γ, X, Y and M correspond to the wavevectors $\vec{k_{||}} = (0,0)$, $\vec{k_{||}} = \left(\frac{\pi}{a}, 0\right)$, $\vec{k_{||}} = \left(0, \frac{\pi}{a}\right)$ and $\vec{k_{||}} = \left(\frac{\pi}{a}, \frac{\pi}{a}\right)$, respectively

do constructively or destructively interfere, we have become able to achieve almost any desired value of m by combining these two approaches. We could for example already interpolate a desired value of $m \approx 0.08$ in both figures 4.8(d) and 4.8(f).

Bandgap in a Square Lattice of Elliptical Holes

A CPCRA could be interpreted as a completely new type of lattice with its own unique band structure. However, another interpretation is to keep in mind the foundation of an underlying square lattice on which we introduce defects, with the only difference to a single defect that these defects are now periodically induced. Since the unit cell of the CPCRA increases proportional to l_x and l_y, the latter approximation offers an important advantage in simulation time if we want to simulate not only the Γ-point, but the full band-diagram of a structure.

In a usual square lattice of circular holes the TE-bandgap is determined only by the lower bandedge at the M-point and the upper bandedge at the X-point as explained in chapter 2.2.4. However, in the case of elliptical holes the four-fold rotational symmetry of the square lattice is reduced to the two-fold case, which also implies that the irreducible Brillouin zone increases to twice of its four-fold symmetry area as depicted in figure 4.9(c).

To achieve the necessary information about the TE-bandgap we perform a simulation of the band structure of square lattices with different elliptical holes in a range of $\frac{r_{x,min}}{a} = 0.25$ to $\frac{r_{x,max}}{a} = 0.4$ and $\frac{r_{y,min}}{a} = \frac{r_x}{a}$ to $\frac{r_{y,max}}{a} = 0.45$ with $T = 9012$ and with $\vec{k_{||}}$ at the Γ, X, Y, and M points.

Before plotting the resulting data, we need to consider another characteristic arising from our specialization on the dipole modes: as seen in figure 4.7 the x-dipole and the y-dipole mode oscillate primarily in the y- and x-direction, respectively. This conversely indicates that the x-dipole primarily leaks to modes with $\vec{k_{||}}$-vectors along the Γ-Y direction, while the y-dipole primarily leaks to modes with $\vec{k_{||}}$-vectors along the Γ-X direction. As the Γ-X and Γ-Y bandgaps both have their minimum at X and Y, respectively, we have divided our plots into one displaying the X-M and another one displaying the Y-M direction.

The results for the above analyzed case of $\frac{r_x}{a} = 0.25$ are presented in figure 4.10. Obviously there is no bandgap in one of the directions at all. This is due to the fact that the bandgap at X or Y and the bandgap

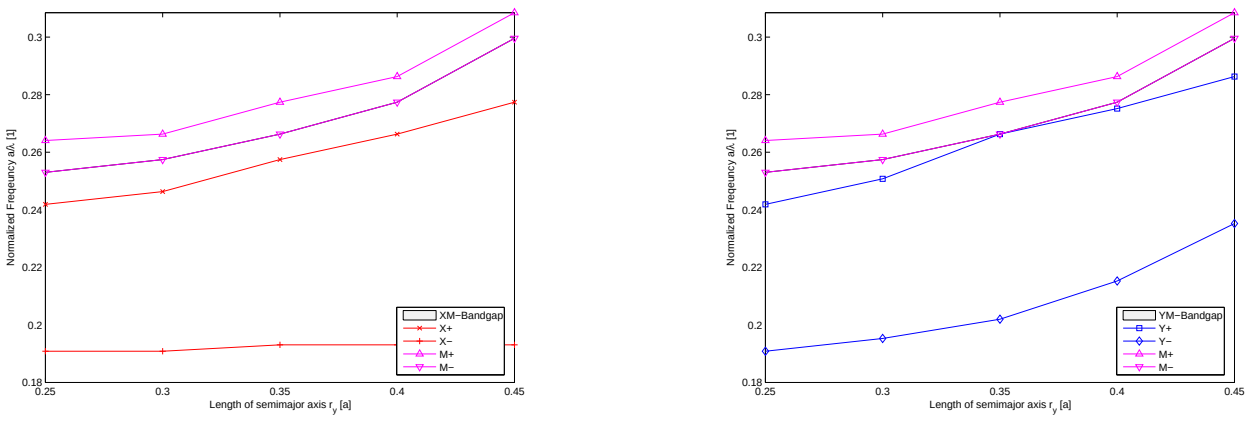

(a) XM-direction for $\frac{r_x}{a} = 0.25$

(b) YM-direction for $\frac{r_x}{a} = 0.25$

Figure 4.10: Upper (+) and lower (-) bandedges at the X and M point and the Y and M point, respectively, with the resulting bandgaps in the different directions. Here we used $\frac{r_x}{a} = 0.25$, $\frac{r_y}{a}$ varies from $\frac{r_y}{a} = 0.25$ to its maximum value of $\frac{r_y}{a} = 0.45$

at M, i.e., the area between the red or blue and the magenta lines do not overlap for any value of $\frac{r_y}{a}$. As we denoted above, this is tolerable as long as we work with dipole modes which are still inside the associated X or Y bandgap, but will nevertheless effectively reduce the achievable in-plane Q-value.

Now let us compare these results to other lengths of the semiminor axis $\frac{r_x}{a}$ illustrated in figure 4.11. In contrast to the $\frac{r_x}{a} = 0.25$-case we here generally do observe a bandgap. This gap has its maximum for all $\frac{r_x}{a}$ values somewhere between $\frac{r_y}{a} = 0.35$ and $\frac{r_x}{a} = 0.4$, a result we would have expected taking into account the known distribution of the bandgap in a circular Silicon square lattice reported for example in [39]. We moreover observe that the lower bandedge at X is more or less independent from variations in $\frac{r_y}{a}$, while the same mode at the Y-point obviously strongly senses this variation. This difference is at first sight not so obvious for the upper bandedge at the same points, but by having a closer look for example at figures 4.11(a) and 4.11(b) we observe a larger bandgap in Y-M than in X-M. Both of course is due to the fact that a mode at Y, i.e., a mode possessing $\vec{k_{||}} = \left(0, \frac{\pi}{a}\right)$ needs to sense a change in $\frac{r_y}{a}$ much more strongly than a mode with an in plane wavevector of $\vec{k_{||}} = \left(\frac{\pi}{a}, 0\right)$. Note that the larger full bandgap in Y-M is achieved to the cost of a much smaller bandgap in Γ-Y due to the differing intensity of the frequency shifts of $Y+$ and $Y-$.

As a result, we observed basically different band-structures in the X-M and Y-M directions for a square lattice of elliptical holes. Moreover, our goal for the design of two dipole modes with high quality factors should be to have at least each, the x-dipole in the Γ-Y and the y-dipole in the Γ-X-bandgaps. Even better $Q_{||}$-factors could be expected for having the x- and y-dipoles in the Y-M and X-M gaps, respectively. Of course the ideal, but because of desired modal splitting less probable case would be having both modes in the full overlapping gap of X-M and Y-M. However, even modes outside of the CPCRA bandgap can be confined almost perfectly in-plane by enclosing the resonator array in a different photonic crystal lattice which is designed especially to confine the CPCRA modes of interest in its ideally full bandgap. This method offers us the possibility to arbitrarily improve the in-plane confinement which will also play a role in the later analysis of the in-plane quality factors of the analyzed CPCRA.

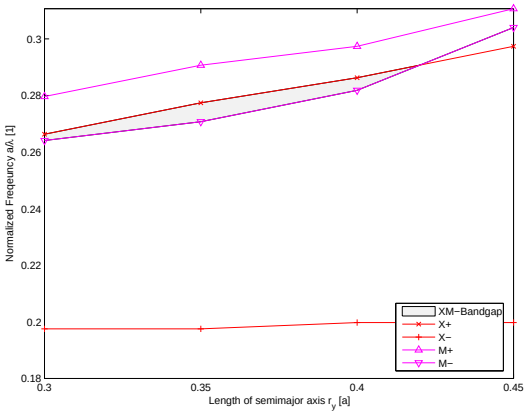

(a) XM-direction for $\frac{r_x}{a} = 0.3$

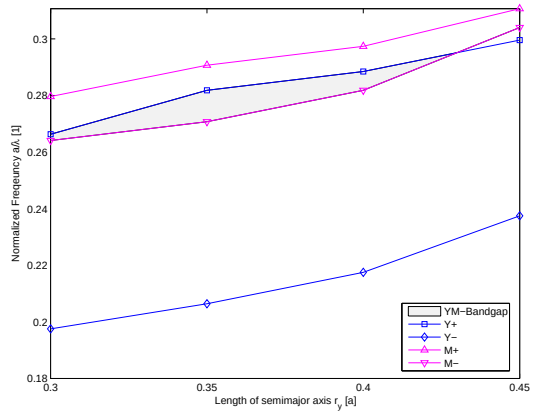

(b) YM-direction for $\frac{r_x}{a} = 0.3$

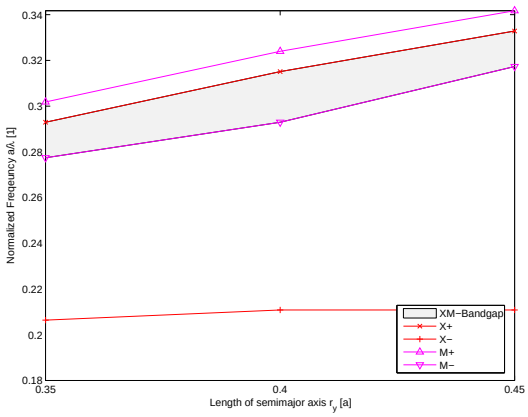

(c) XM-direction for $\frac{r_x}{a} = 0.35$

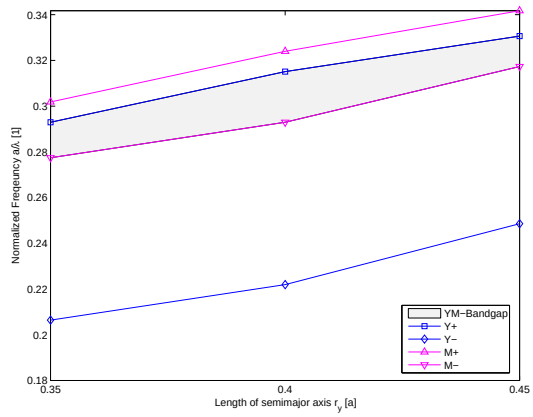

(d) YM-direction for $\frac{r_x}{a} = 0.35$

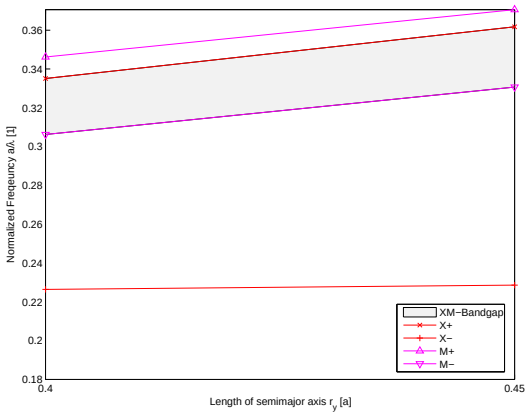

(e) XM-direction for $\frac{r_x}{a} = 0.4$

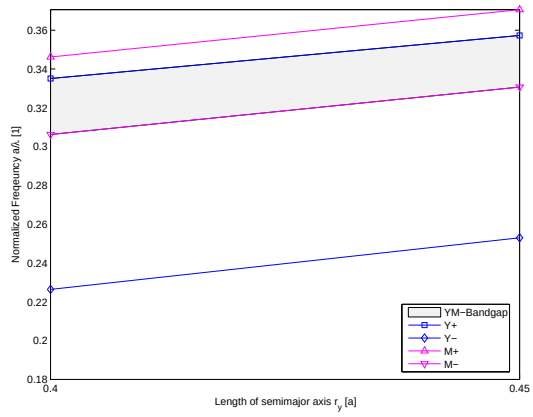

(f) YM-direction for $\frac{r_x}{a} = 0.4$

Figure 4.11: Upper (+) and lower (-) bandedges at the X and M point and the Y and M point, respectively, with the resulting bandgaps in the different directions. While the bandgaps are plotted for each different value $\frac{r_x}{a}$, inside each plot $\frac{r_y}{a}$ varies from the specific $\frac{r_y}{a} = \frac{r_x}{a}$ to its maximum value of $\frac{r_y}{a} = 0.45$

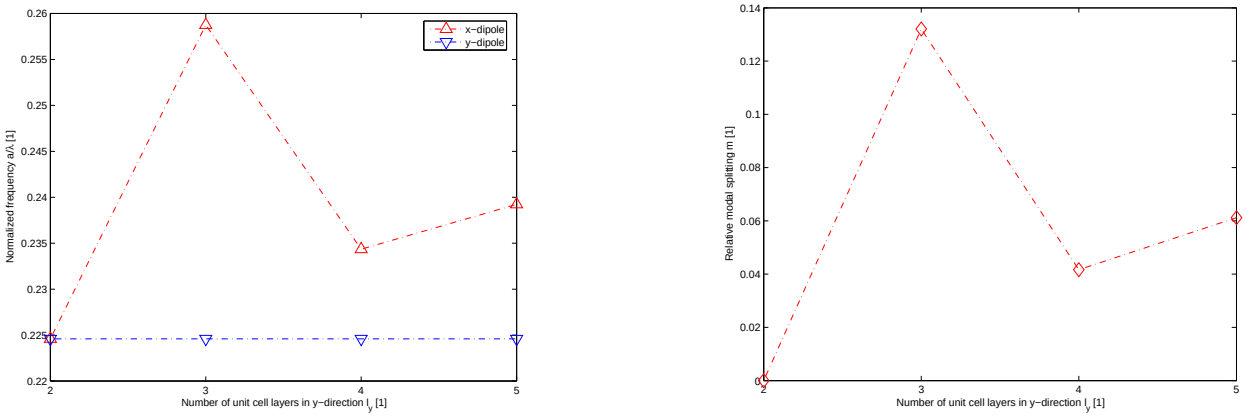

(a) Normalized frequency $\frac{a}{\lambda}$

(b) Relative modal splitting m

Figure 4.12: Normalized frequencies and relative modal splitting of the x- and y- dipoles versus the length of the unit cell in y-direction l_y in a CPCRA with $\frac{r_x}{a} = 0.25$ and $l_x = 2$

4.2.2 Thickness of the Inter-Cavity Barrier

As seen in the previous chapter, an asymmetric variation in the numbers of layers l_x and l_y of the unit cell, i.e., a variation of the thickness of the photonic crystal barrier between two holes, causes a basic relative modal splitting even for circular holes, the so called *basic barrier splitting*. This basic splitting can interfere constructively or destructively with the splitting due to ellipse induced asymmetry as seen in figure 4.8. These results, especially because of the much broader range of m-values, will be discussed and extended in this chapter.

To be able to reuse the values of section 4.2.1 we first again choose a value of $\frac{r_x}{a} = 0.25$. As we already analyzed the interaction between the ellipse induced asymmetry and the layer induced asymmetry, we will in the following examination focus on circular holes, i.e., $\frac{r_y}{a} = 0.25$. Different hole radii and the interaction between the hole size and the basic barrier splitting will be discussed in chapter 4.2.3.

In a first approach we extended the range of l_i-values to $l_x, l_y \in [2; 6]$. However, the intensity of for example the y-dipole mode for $l_y = 6$ was extremely weak and sometimes undetectable, so that we will restrict our analysis to values of $l_x, l_y \in [2; 5]$. Performing the same simulation steps as in 4.2.1 for $l_x \in [2; 4]$ and $l_y = 5$ and including the old values for $l_x \in [2; 4]$ and $l_y \in [2; 4]$ we achieve the results plotted in figures 4.12 and 4.15.

To understand the observed modal splittings, we first focus on the case $l_x = 2$ depicted in figure 4.12.

For a fourfold rotational symmetric lattice, i.e., $l_x = l_y = 2$, we of course achieve degenerate dipole modes at $\frac{a}{\lambda} = 0.22459$ and thus a relative modal splitting of $m = 0$. However, an increase of l_y while keeping $l_x = 2$ constant leads to a variation of the x-dipole mode frequency, while the y-dipole seems unaffected. Moreover, we observe a huge increase of the x-dipole frequency to $\frac{a}{\lambda} = 0.25876$ for $l_y = 3$. For $l_y = 4$, however, instead of further increase the experiments show a drop of the x-dipole energy.

To understand the origin of these different reactions, we need to discuss the spatial field distribution of the two dipole modes for different barrier sizes. As we enforced TE-like modes, the field component of interest at the center of the photonic crystal slab is B_z. For the moment, we want to concentrate on the y-dipole fields for $l_y \in [2; 4]$ which are depicted in figure 4.13.

As expected, the y-dipole couples almost exclusively in the x-direction of the lattice. However, the manipulation in the width of the cavity barrier we performed here affected almost exclusively just the off-cavity

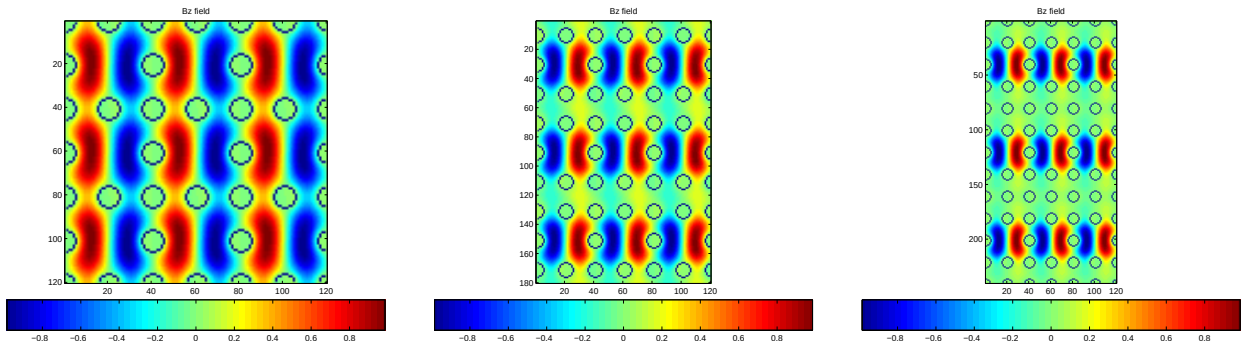

(a) $l_y = 2$ (b) $l_y = 3$ (c) $l_y = 4$

Figure 4.13: B_z-fields of the y-dipole modes for $\frac{r_x}{a} = \frac{r_y}{a} = 0.25$, $l_x = 2$ and varying l_y in normalized units at the center of the photonic crystal slab

space in y-direction, which therefore does neither affect the modal pattern of the y-dipole nor its frequency.

For the x-dipoles we again try to explain the sudden rise in frequency for $l_y = 3$ by means of the B_z fields depicted in figures 4.14((a)-(c)). Although not directly obvious because we have just one layer of holes between the cavities, we expect again an exclusive coupling of the x-dipole in the direction perpendicular to its axis. Between the cavities, we here detect for $l_x > 2$ the appearance of a smaller leaking inter-cavity intensity peak which exhibits the same symmetry as the original intra-cavity dipole. For reasons of the distance of the cavities and the numbers of holes between them, in the case of $l_y = 3$ this inter-cavity intensity peak is overlapping with two air holes, while for $l_y = 4$ this overlap is effectively reduced as the intensity peaks have the possibility to squeeze between two holes.

To explain the observed jump in frequency for $l_y = 3$ one could be tempted to follow the common explanation of an increased amount of field in air, which increases energy and thus also the frequency. However, compared for example to an increase in the hole radius, one has to be more careful in this case. We are examining small spatial structures, and we here are not interested in the qualitative general increase in frequency for an effective increase in air volume. Instead, we need to recall equation 2.34 which describes the electromagnetic energy functional. It states that the energy is minimized when the displacement field $\vec{D}$ is concentrated in high dielectric. However, rewriting the same equation in terms of E leads to

$$E_f\left(\vec{H}\right) = \frac{1}{2\left(\vec{H},\vec{H}\right)} \int d\vec{r}\epsilon \left|\frac{\omega}{c_0}\vec{E}\right|^2 \tag{4.16}$$

which implies that effectively a *small* fraction of $\vec{E}$ in a high dielectric minimizes the energy functional. If we therefore analyze the $|\vec{E}|^2$ distribution in figure 4.14((d)-(f)), we observe an effective $|\vec{E}|^2$-peak in the inter-cavity air holes for $l_y \neq 3$, while for $l_y = 3$ $|\vec{E}|^2$ is almost ideally confined in silicon. Necessarily, we would expect an appropriate increase in energy for $l_y = 3$, which corresponds pretty well to the results of the FDTD simulations.

For the sake of completeness we also added the results for $l_x = 3$ and $l_x = 4$ depicted in figure 4.15. From the results for $l_x = 2$ one could assume that the frequencies of the y-dipole is always almost immune against variations of l_y, and moreover that it shows the same reaction to variations of l_x as the x-dipole shows to variations of l_y as seen above. Both is exactly verified by the experimental results:

As the blue curve remains always parallel to the x-axis, an increase in l_y again does not affect the y-dipole, which proves our first assumption. Comparing the absolute values of the $((\frac{a}{\lambda})_{x-dipole,l_y})$ and $((\frac{a}{\lambda})_{y-dipole,l_x})$

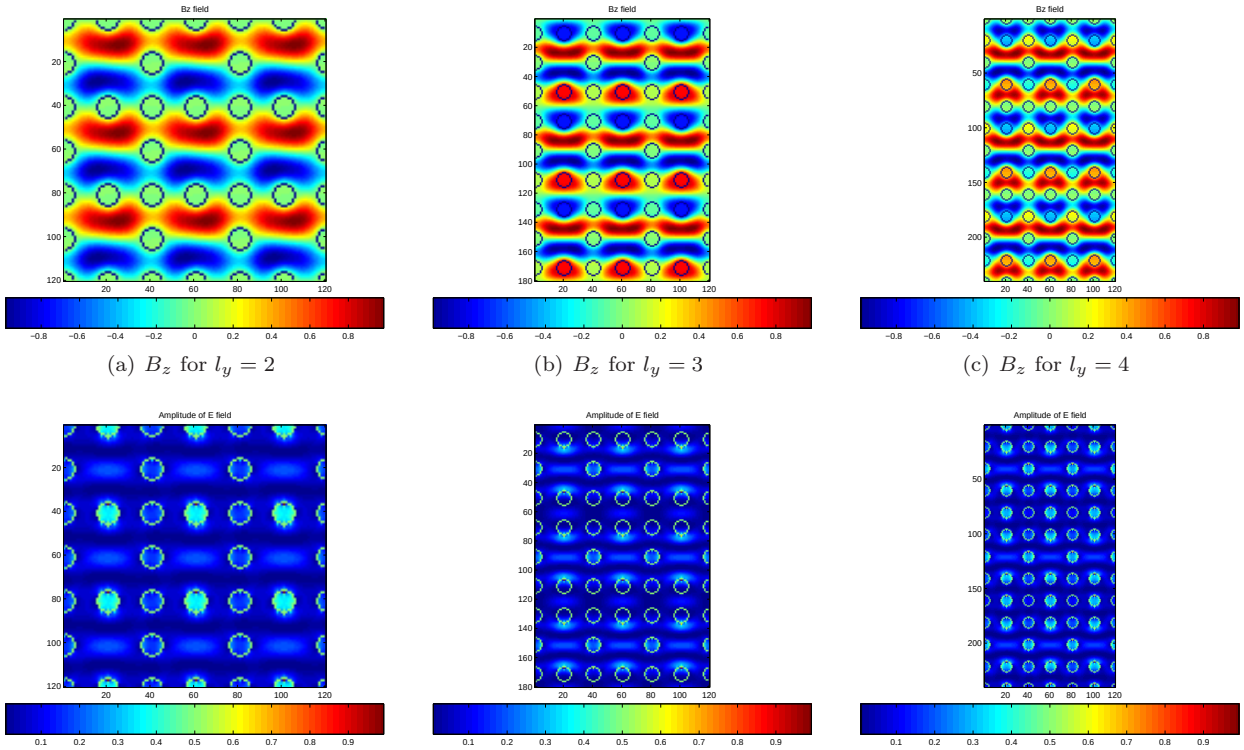

(a) B_z for $l_y = 2$ (b) B_z for $l_y = 3$ (c) B_z for $l_y = 4$

(d) E_a for $l_y = 2$ (e) E_a for $l_y = 3$ (f) E_a for $l_y = 4$

Figure 4.14: B_z and $|\vec{E}|^2$ of the x-dipole modes for $\frac{r_x}{a} = \frac{r_y}{a} = 0.25$, $l_x = 2$ and varying l_y in normalized units at the center of the photonic crystal slab

between the figures also verifies our second assumption, as for example $l_x = 3$ causes the y-dipole to oscillate at $\frac{a}{\lambda} = 0.25876$, while $l_y = 3$ equally forces the x-dipole to appear at the same normalized frequency.

Keeping in mind the primary direction of oscillation of the two dipoles and the explanation for the basic barrier splitting for the (l_x=2)-case, this is the expected result. However, it is in this precision not completely self-evident as in the modal profiles we indeed observe a primary direction of oscillation, but nevertheless also recognize a small amount of coupling in the perpendicular direction.

Note that the dashed lines in figures 4.12 and 4.15 are just plotted to guide the eye. l_x and l_y are physically restricted to be integers in the range $\mathbb{N}\setminus\{1\}$ which causes any interpolation between the splitting values to be meaningless. However, a different approach to nevertheless try to approximate non-integer numbers of layers could be achieved by a switch to a rectangular lattice as proposed in section 4.3.2.

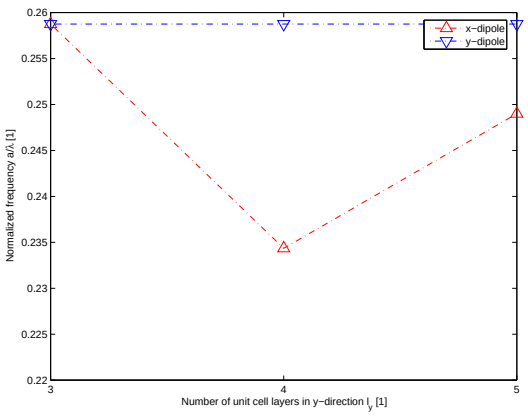

(a) Normalized frequency $\frac{a}{\lambda}$ for $l_x = 3$

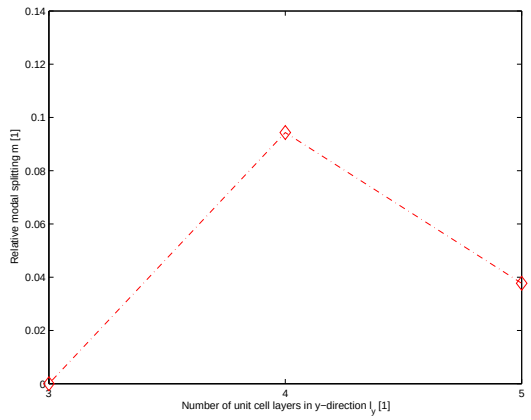

(b) Relative modal splitting m for $l_x = 3$

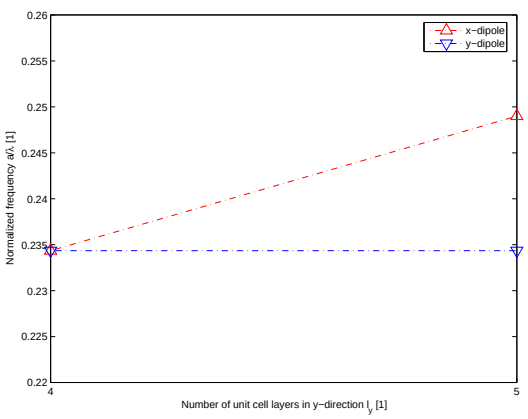

(c) Normalized frequency $\frac{a}{\lambda}$ for $l_x = 4$

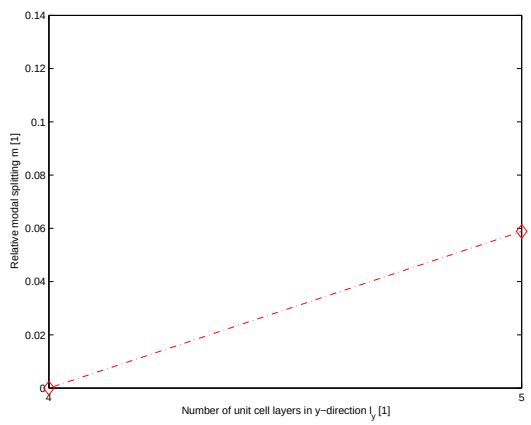

(d) Relative modal splitting m for $l_x = 4$

Figure 4.15: Normalized frequencies and relative modal splitting of the x- and y- dipoles versus the length of the unit cell in y-direction l_y in a CPCRA with $\frac{r_x}{a} = 0.25$ and a constant l_x

4.2.3 Radius of Circular Holes

The results of the previous sections have all been achieved for a basic radius $\frac{r_x}{a} = 0.25$, which for circular holes means $\frac{r}{a} = 0.25$. Yet we have seen in chapter 4.2.1 that there is no full bandgap for this case, which suggest the examination of larger radii. An interesting object of investigation would therefore be the influence of the hole radius on the basic barrier splitting. We could generally assume a tunability of the dipole modes by stretching the holes to ellipses even for bigger basic radii, although the range of achievable relative modal splitting would be smaller according to the reduced eccentricity. This assumption allows us to reduce our examination to the case of circular holes with varying hole radii and also varying numbers of layers in the different lattice directions.

The FDTD setup and simulation steps are again the same as in the previous chapters, this time with a parameter range of

$$\frac{r_x}{a} = \frac{r_y}{a} = \frac{r}{a} \in [0.25; 0.4] \text{ and } l_x, l_y \in [2; 5] \tag{4.17}$$

The resulting normalized frequencies for all twofold rotational symmetric (l_x;l_y)-combinations are presented in figure 4.16. As one would expect, an increase in the hole radius causes a general decrease in the effective refractive index of the photonic crystal slab and thus a shift of all modes to higher frequencies. However, while for example in the case of $l_x = 3$ and $l_y = 4$ the y-dipole frequency seems to posses an approximately constant slope with regards to $\frac{r}{a}$, the slope of the x-dipole frequency is clearly increasing. These different intensities of reaction lead to a variation of the Δf distance between each pair of curves. Keeping in mind that we defined the relative modal splitting as

$$m = \frac{\Delta f}{f_p}, \tag{4.18}$$

and moreover assuming an approximately constant f_p, this variation in Δf would also originate a variation in the figure of merit m.

However, we not only observe this slight variation in Δf, but also the above mentioned change in the reference pump frequency f_p, which in the case of Stokes beam collection is always the mode at higher frequency. Consequently the reaction of m suffers a typical tradeoff, which generates either maxima or minima in the relevant m-$\frac{r}{a}$-curves depicted in figure 4.17.

The region of figure 4.17 which is shaded in gray corresponds to the range of desired modal frequency splitting as deducted in chapter 3.1. Obviously there are already four arrangements of l_x, l_y and $\frac{r}{a}$ which would exhibit the desired values of relative modal splitting.

To estimate the possible confinement of the analyzed modes, we should again discuss the different bandgaps of the underlying photonic crystal square lattices. As the necessary FDTD simulations have already been done in section 4.2.1, we here just extract the corresponding values to figure 4.18 for convenience. As known for example from [39], the maximum bandgap for two-dimensional photonic crystal slab is achieved around $\frac{r}{a} = 0.4$. For the application of the modes examined in this chapter on the design of a CPCRA Raman laser in chapter 5, we could expect a generally broader range of confined modes for large radii, and should be careful to find x- and y-dipole modes which both are located inside the photonic bandgap, with the possible improvement of a half-full or full bandgap as mentioned in section 4.2.1.

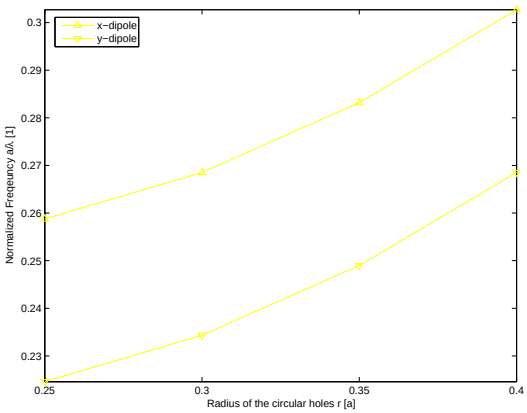

(a) Normalized frequency $\frac{a}{\lambda}$ for $l_x = 2$ and $l_y = 3$

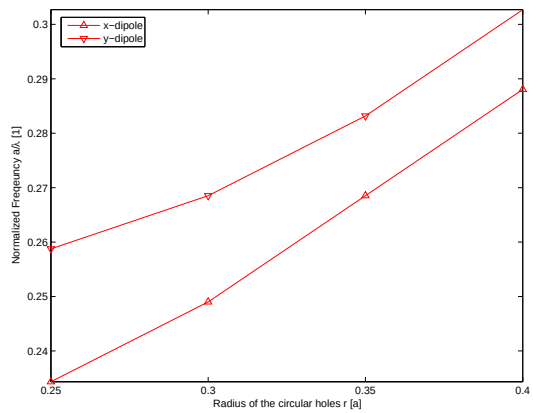

(b) Normalized frequency $\frac{a}{\lambda}$ for $l_x = 3$ and $l_y = 4$

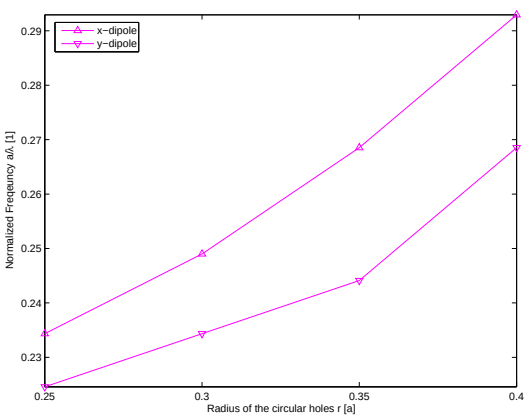

(c) Normalized frequency $\frac{a}{\lambda}$ for $l_x = 2$ and $l_y = 4$

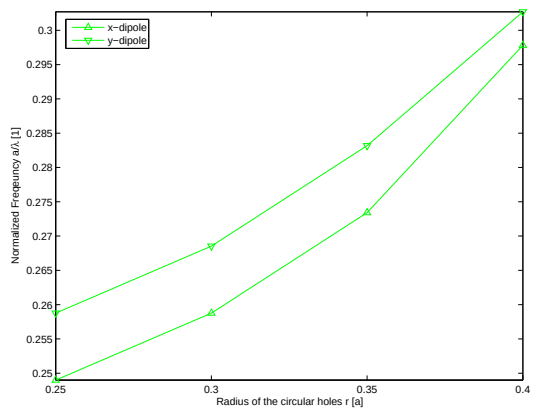

(d) Normalized frequency $\frac{a}{\lambda}$ for $l_x = 3$ and $l_y = 5$

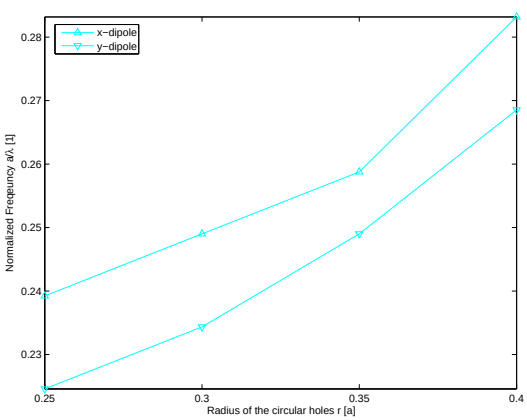

(e) Normalized frequency $\frac{a}{\lambda}$ for $l_x = 2$ and $l_y = 5$

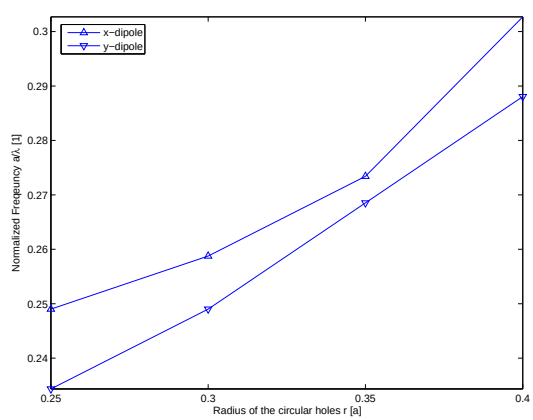

(f) Normalized frequency $\frac{a}{\lambda}$ for $l_x = 4$ and $l_y = 5$

Figure 4.16: Normalized frequencies of the x- and y- dipoles versus the radius of the circular holes $\frac{r}{a}$ in a CPCRA with asymmetric arrangements of the cavities, i.e., $l_x \neq l_y$

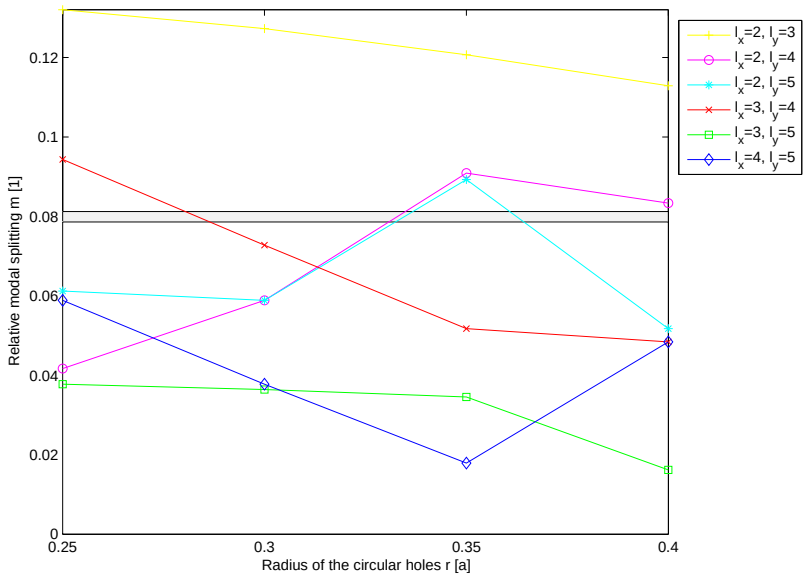

Figure 4.17: Relative modal splitting m of the x- and y- dipoles versus the radius of the circular holes $\frac{r}{a}$ in a CPCRA with asymmetric arrangements of the cavities, i.e., $l_x \neq l_y$

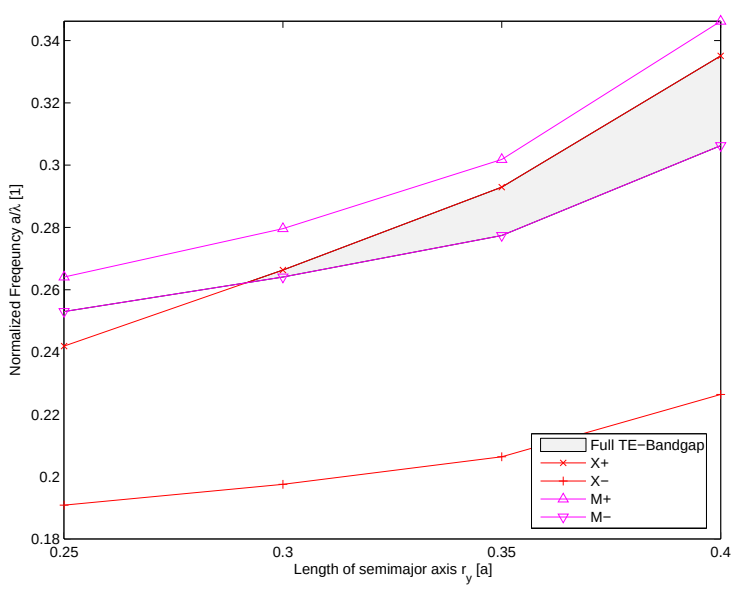

Figure 4.18: Upper (+) and lower (-) bandedges at the X and M point with the resulting full bandgap versus varying $\frac{r}{a}$ for the underlying square lattice

4.3 Results and Discussion

In this chapter we analyzed different parameters of a two-dimensional CPCRA slab and their influence on the frequencies of the x- and y-dipole modes. The general idea behind all performed manipulations was to break the fourfold rotational symmetry of the standard CPCRA and therefore lift the degeneracy of the dipole modes to achieve a relative modal splitting in a range of:

$$m_{desired} \in [0.0786; 0.0812] \tag{4.19}$$

After the preparation of a tailored FDTD simulation setup we examined the influences of different approximations of a twofold rotational symmetric air hole shape, the eccentricity of elliptical holes, the thickness of the inter-cavity barrier, the radius of the air holes and the interactions of all of these parameters.

The achievable splitting via ellipse eccentricity was reported to be arbitrarily variable in a range of

$$m_{eccentricity} \in [0; 0.05]\,. \tag{4.20}$$

Via introducing different numbers of barrier layers between the cavities, we achieve discrete values of the basic barrier splitting, all in the interval

$$m_{barrier,\frac{r}{a}=0.25} \in [0.038; 0.132]\,. \tag{4.21}$$

These discrete values were either tunable by simple variation of the radius of circular holes, which should basically enable us to fabricate any m value in

$$m_{barrier,\frac{r}{a}\in[0.25;0.4]} \in [0.017; 0.09] \cup [0.113; 0.132] \tag{4.22}$$

or by combining the basic barrier splitting and hole eccentricity, which extends the range of arbitrarily achievable relative modal splittings to approximately:

$$m_{barrier,eccentricity} \in [0; 0.18]\,, \tag{4.23}$$

Note that, although m is for sure the most important condition we need to fulfill, for the achievement of stimulated Raman scattering in a silicon CPCRA we furthermore need to optimize other properties of the structure like the quality factors of the modes or the modal overlap. These will be discussed in chapter 5.

4.3.1 Error Analysis

It was alluded above to the fact that the frequency resolution for all experiments except for the analysis of the different hole shapes was chosen as

$$\delta_{\frac{a}{\lambda}} = 0.00488. \tag{4.24}$$

We can expect the numerical errors to be uniformly distributed, which decreases the standard deviation to:

$$\sigma_f = \frac{1}{4}\delta_{\frac{a}{\lambda}} = 0.00122 \tag{4.25}$$

Assuming the errors in f_p and f_s to be statistically independent we can calculate the standard deviation of the measured m values by applying Gauss' error propagation law:

$$\sigma_{m(f_i)} = \sqrt{\sum_i \left(\frac{\partial m}{\partial f_i}\right)^2 \sigma_{f_i}^2} \tag{4.26}$$

For the case of

$$m\left(f_p, f_s\right) = \frac{f_p - f_s}{f_p} \tag{4.27}$$

this leads to:

$$\sigma_{m(f_p,f_s)} = \sqrt{\left(\frac{\partial m}{\partial f_p}\right)^2 \sigma_{f_p}^2 + \left(\frac{\partial m}{\partial f_s}\right)^2 \sigma_{f_s}^2} = \sqrt{\left(\frac{f_s}{f_p^2}\right)^2 \sigma_{f_p}^2 + \left(-\frac{1}{f_p}\right)^2 \sigma_{f_s}^2} \tag{4.28}$$

As we can assume $\sigma_{f_p} = \sigma_{f_s}$, the standard deviation of the measured m values equals:

$$\sigma_{m(f_p,f_s)} = \sqrt{\frac{f_s^2 + f_p^2}{f_p^4}\sigma_f^2} = \frac{\sqrt{f_s^2 + f_p^2}}{f_p^2}\sigma_f \tag{4.29}$$

Keeping in mind that $f_p > f_s$, this error is minimized for huge f_p and small f_s values, i.e., for large relative modal splittings. However, we here almost exclusively deal with values of $\Delta f << f_p$, so we can approximate the error in m as

$$\sigma_{m(f_p,f_s)} \overset{f_s \approx f_p}{\rightarrow} \sqrt{2}\frac{\sigma_f}{f} = \sqrt{2}\frac{\sigma_{\frac{a}{\lambda}}}{\frac{a}{\lambda}} \tag{4.30}$$

Assuming $\frac{a}{\lambda} \approx 0.25$ and $\sigma_{\frac{a}{\lambda}} = 0.00122$ we achieve

$$\sigma_m \approx 0.007 \tag{4.31}$$

which equals an undesirable high relative error of $\sigma_{\frac{a}{\lambda},relative} \approx 10\%$ with respect to the absolute range of m. However, we here assumed the worst case of $f_s = f_p$ and moreover did not take into account statistical improvements of the results. Fitting any achieved curves and therefore using all available N data points thus could reduce the error in m by another factor of $\frac{1}{\sqrt{N}}$.

4.3.2 Other Possible Parameters

We want to conclude this chapter with a proposal of other parameters, which unfortunately need to remain unexamined in this thesis. Possible further manipulations of CPCRA structures to achieve Raman lasing could include the following:

- The focus of the analysis could be laid on *different defect modes*. Although we already explained the advantages of the dipole modes, for example higher quality factors could motivate further examination of the quadrupole mode.
- The rotatable stage of the optical setup proposed in chapter 3.2 allows pump and collection at *different angles*, which lifts the restriction to the Γ point. Therefore the dependence of the analyzed and possible other dipole mode properties on different in-plane wavevectors $\vec{k}_{||}$ would be another interesting object of examination.
- CPCRAs could moreover be integrated in different underlying lattice types such as the *rectangular lattice* or the *triangular lattice*. While the latter would make a completely new analysis necessary, the first could also be interpreted as a small perturbation on the already examined square lattice, which therefore would give us another degree of freedom to disturb the fourfold rotational symmetry and achieve systematically and precisely tunable dipole splitting.
- In addition, we could vary the *type of the introduced cavities*. While a switch to other modes in the same structure as analyzed would eventually allow us to vary the central cavity hole, other cavity defects such as for example linear defects would exhibit a completely different behavior.

- Another parameter which has not been analyzed yet with respect to high-Q modes in CPCRA structures is the photonic crystal *slab thickness d*. As especially the out-of-plane quality factors, but also the variety and frequencies of possible defect modes strongly depends on this parameter, a better understanding of its impact on possible CPCRA lasing modes would be of fundamental importance for industrial application and optimization of a CPCRA Raman laser.
- One universal tool for the optimization of the already achieved results could be the application of *small perturbations* in the structure which for example would enable us to manipulate the inter-cavity $\vec{E}$-field peaks to hit or pass special air holes, or, even more important with respect to the lasing threshold, optimize the quality factors to their maximum applicable values.

Of course, such a list of proposals is always incomplete. Therefore the suggested solution and also the following design and analysis should not be understood as a final engineering result, but rather as a basic study of one possible solution, based not in general, but partly also on some arbitrary and intuitive, but necessary decisions.

5 Analysis of a Two-Dimensional CPCRA Raman Laser Design

Following the general analysis of the influence of different parameters on the dipole modes in a silicon CPCRA, we in this section want to apply these results on one possible design of a Raman laser. The properties of the proposed laser design are determined and compared to recent other approaches in the field.

5.1 Decision for one Basic Barrier Splitting

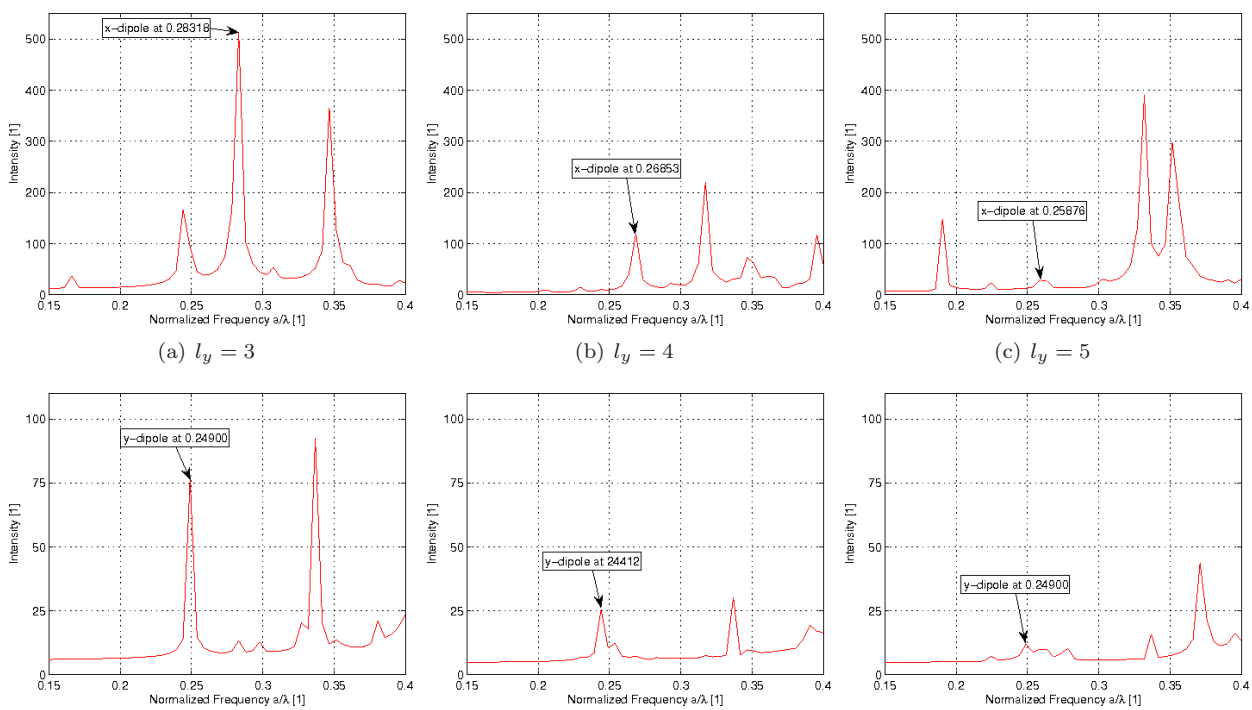

(a) $l_y = 3$ (b) $l_y = 4$ (c) $l_y = 5$

(d) $l_y = 3$ (e) $l_y = 4$ (f) $l_y = 5$

Figure 5.1: Spectra of CPCRAs with $l_x = 2$ and y-dipole excitation; $\frac{r}{a}$ is chosen as $\frac{r}{a} = 0.35$ due to m values closest to the range of desired relative modal splitting (see figure 4.17)

In the results of the previous chapter we already mentioned that for stimulated Raman scattering we generally need to assure a correct relative modal splitting m. A review of section 4.3 discloses that this is only achievable by the means of the basic barrier splitting, i.e., we need to choose a lattice with different barrier thicknesses in different lattice directions. To later adjust the basic barrier splitting to the desired range, we

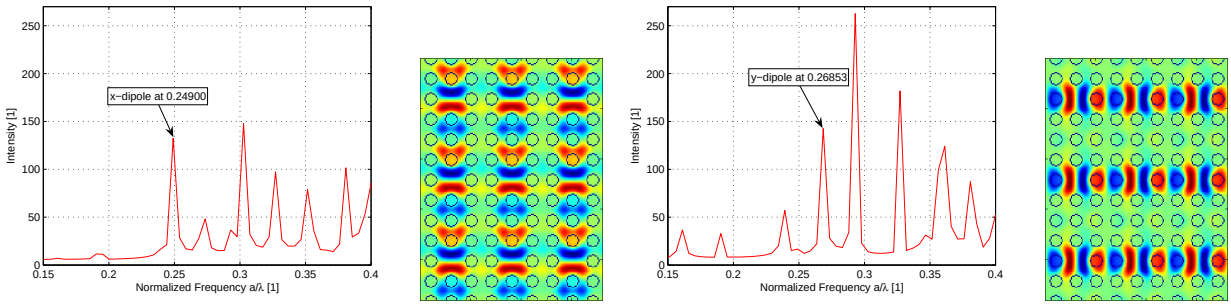

(a) Spectrum for x-dipole excitation (b) B_z-field of the x-dipole mode (c) Spectrum for y-dipole excitation (d) B_z-field of the y-dipole mode

Figure 5.2: Spectra and B_z-fields of a CPCRA with $l_x = 3$ and $l_y = 4$; $\frac{r}{a}$ is this time chosen as $\frac{r}{a} = 0.30$ due to m values closest to the range of desired relative modal splitting (see figure 4.17)

need to further manipulate the structure by either adjustment of the hole diameter or the introduction of elliptical holes.

Reinvestigating figure 4.17 and expecting a maximum additional ellipses induced splitting of $m_{max,ell} \approx 0.05$, which is of course only achievable for high eccentricities, we expect only the $(l_x; l_y)$-tuples $(2; 4)$, $(2; 5)$ and $(3; 4)$ to be promising candidates. To make a decision for one of them, we need to further estimate and compare other properties of the CPCRAs like the quality factors Q and the intensity overlap ξ of the modes.

We first want to focus on the tuples $(2; 4)$ and $(2; 5)$. Again consulting figure 4.17 we recognize two possible intervals of circular hole size for both structures which would possess the desired m values. To get a rough overview over the possible quality factors, we have a look at the spectra of the structures in figure 5.1, where for the sake of comparison also the spectrum for $(l_x; l_y) = (2; 3)$ is added. Although the intensity scale is partially arbitrary as the observed intensity values are just the summarized field intensities at a defined set of collection points, they nevertheless become meaningful in comparison with spectra of identical experimental setup for different structures. We performed the same experiments with various different collection point and achieved qualitatively the same following results: Although excited with the corresponding dipole fields distributed over the cavity unit cell, the intensities which are confined in the x-dipole and y-dipole mode drop dramatically with increasing barrier size in y-direction. These very weak peaks reveal proportionally small quality factors, which cause the CPCRAs to be hardly applicable in a Raman laser design, especially as the even weaker y-dipole mode in this case would be the lasing Stokes mode.

Second, we performed an equivalent spectrum analysis for $(l_x; l_y) = (3; 4)$ which's results can be found in figures 5.2(a) and 5.2(c). Although we examined a larger structure excited with the same field energy, the achieved peak intensities of the Stokes mode are roughly increased by one order of magnitude, which discloses significantly lower losses and thus higher quality factors than in the previously analyzed CPCRAs. To moreover get a first impression of the modal confinement in this structure, we also plotted the B_z field distributions in figures 5.2(b) and 5.2(d). Comparing the analysis from 4.2.2 one observes the expected patterns which exhibit a relatively good field confinement inside the cavities. This is necessary for the design of a good modal overlap, small mode volumes and thus a low lasing threshold. We therefore will subsequently focus our design proposal on this CPCRA structure.

5.2 Optimization of Eccentricity

After having found the basic barrier setting $(l_x; l_y) = (3; 4)$ as a promising candidate, we still need to precisely tune the relative modal splitting by hole size variation to achieve a value in the desired m range. Although figure 4.17 suggest possible designs of structures with circular holes around $\frac{r}{a} \approx 0.275$, we decided not to focus on these structures. The dispersion diagram analysis in chapter 4.2.1 prospects the defect modes of these lattices to possess weak confinement because the full band gap disappears around this hole size. Instead, we ran similar simulations as before for elliptical holes in the range of

$$\frac{r_x}{a} \in [0.3; 0.45] \text{ and } \frac{r_y}{a} \in [0.3; 0.4]\,. \tag{5.1}$$

As the basic barrier splitting in this range of circular hole radii is generally below the desired range, we need to increase the basic m value, i.e., we need to choose eccentricities which interact constructively with the basic barrier splitting of $(l_x; l_y) = (3; 4)$. A comparison with section 4.2.1 leads to the conclusion that it is sufficient to examine designs for which

$$\frac{r_x}{a} \geq \frac{r_y}{a} \tag{5.2}$$

holds.

For the design of a laser array, we should moreover achieve a detailed knowledge of the whole frequency spectrum of the analyzed structures. As with the previous results we are able to roughly estimate the expected x- and y-dipole frequencies, we can thus switch back to Gaussian excitation. To decrease the errors in frequency and in m we also change the experimental setup to a time evolution period of $T = 1.1 \cdot 2^{14} \approx 18022$, implying a frequency resolution of

$$\delta_{\frac{a}{\lambda}} = 0.001110 \tag{5.3}$$

and thus an error in m of

$$\sigma_m \approx 0.0016. \tag{5.4}$$

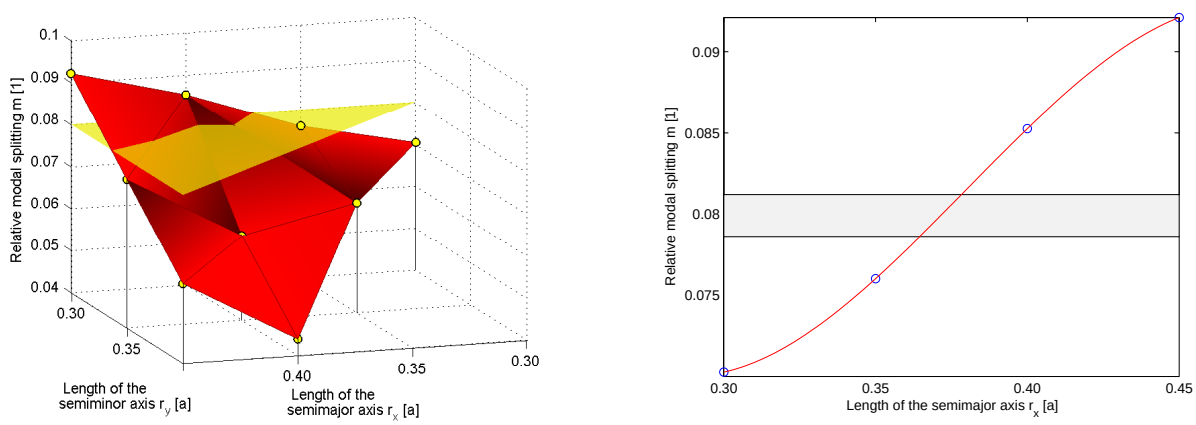

(a) Linear interpolation of the relative modal frequency splitting m in the parameter range $(\frac{r_x}{a}; \frac{r_y}{a}) \in (0.3..0.45; 0.3..0.4)$; the center of the interval of desired m values is depicted in yellow

(b) 3rd order interpolation of the relative modal frequency splitting m for $\frac{r_y}{a} = 0.3$ and $\frac{r_x}{a} \in (0.3..0.45)$; the interval of desired relative modal splitting is shaded in grey

Figure 5.3: Optimization of the hole eccentricity in a CPCRA with $(l_x; l_y) = (3; 4)$

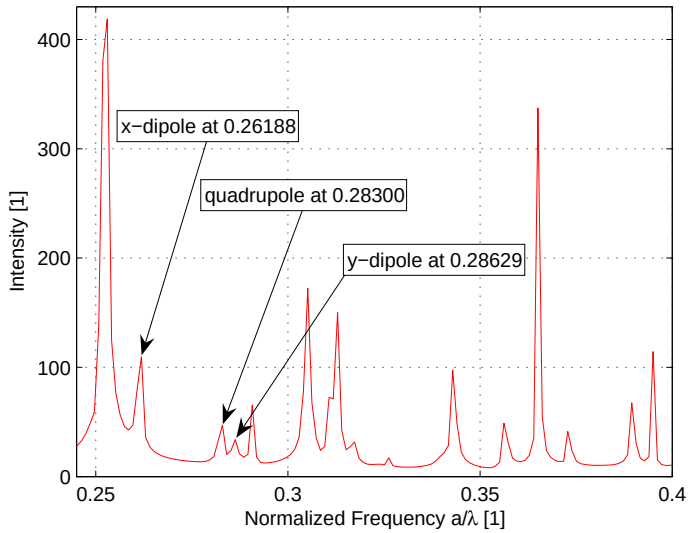

Figure 5.4: Detailed spectrum of a CPCRA with $l_x = 3$, $l_y = 4$, $\frac{r_x}{a} = 0.4$, $\frac{r_y}{a} = 0.3$ and a time evolution period of $T = 18022$ timesteps

The general reaction and range of the dipole frequencies is well known from the previous chapter, so as we here are interested in m optimization, we can skip a detailed frequency analysis of all structures and concentrate on the relative modal splitting. The resulting values for the simulated range of hole radii is depicted in a three dimensional plot in figure 5.3(a). The exact results are visualized as yellow dots, while the space between these results is interpolated linearly. For orientation, the central frequency of the desired modal splittings interval is visualized as a transparent yellow plane. The intersection of the two planes defines, as a good approximation, a curve of an infinite number of possible solutions. We should note that this curve is, assuming the whole range of desired m values, actually a band. The $\frac{r_y}{a} = 0.3$ plane of this plot is projected to figure 5.3(b) and here interpolated with the following, numerically achieved polynomial:

$$m\left(\frac{r_x}{a}\right) = -7.8552\left(\frac{r_x}{a}\right)^3 + 8.9456\left(\frac{r_x}{a}\right)^2 - 3.2056\frac{r_x}{a} + 0.4389 \tag{5.5}$$

Evaluating the inverse function of this polynomial on the edges of the desired m interval, the range of possible lengths of the semimajor axis $\frac{r_x}{a}$ for the parameters $\frac{r_y}{a} = 0.3$, $l_x = 3$ and $l_y = 4$ results to:

$$\frac{r_x}{a} \in [0.3645; 0.3785] \tag{5.6}$$

However, in this approximative design proposal we want to hold on to multiples of 0.05 for $\frac{r_x}{a}$, which leaves us the decision between $\frac{r_{x,1}}{a} = 0.35$ and $\frac{r_{x,1}}{a} = 0.4$, both actually outside of the desired range. As we intend to do rather a worst case analysis for the lasing threshold, we pick the larger value, which also induces a higher eccentricity and thus probably a slightly smaller Q-value.

A detailed spectrum of this structure achieved with the above mentioned simulation parameters is depicted in figure 5.4. As expected, we excited a much broader variety of modes. The x- and y-dipole modes seem to be sufficiently isolated, sharp and intense, which we hope will result in proper quality factors. The calculation

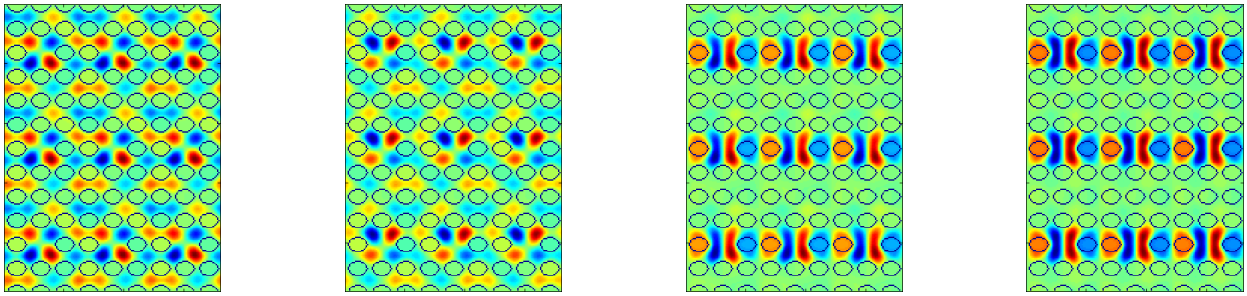

(a) Filter level 6 (b) Filter level 7 (c) Filter level 8 (d) Filter level 9

Figure 5.5: B_z fields of the y-dipole for $\frac{r_x}{a} = 0.4$, $\frac{r_y}{a} = 0.3$ and varying filter depth

of these will be performed in section 5.3. The found exact mode frequencies from figure 5.4 are

$$\frac{a}{\lambda_p} = 0.28629 \text{ and } \frac{a}{\lambda_s} = 0.26188 \tag{5.7}$$

where the mode with the higher frequency, in this case the y-dipole mode, represents the pump-mode and the x-dipole mode at $\frac{a}{\lambda_s} = 0.26188$ represents the lasing Stokes mode.

We can now also convert the unified and scalable FDTD units into real dimensions, as

$$\Delta f = 15.6THz \text{ and } \Delta_{\frac{a}{\lambda}} = \frac{a}{\lambda_p} - \frac{a}{\lambda_s} \tag{5.8}$$

unambiguously defines

$$a = \frac{c_0}{\Delta f}\Delta_{\frac{a}{\lambda}} = 472.12nm \tag{5.9}$$

and therefore

$$\lambda_p = 1.69\mu m \text{ and } \lambda_s = 1.80\mu m \tag{5.10}$$

Note that these values slightly exceed the preliminary experimental boundaries which we discussed in chapter 3.1. This is due to the fact that for the analysis of one design we restricted ourselves to $\frac{r_i}{a}$ values which are multiples of 0.05 and thus chose a too large $\frac{r_x}{a} = 0.4$ above. However, this does not dramatically affect the following Q-factor and lasing threshold analysis which should represent a worst case analysis, and does not affect later experiments either as they can in fact be realized for the ideal $\frac{r_x}{a}$ value calculated in equation 5.6. For the sake of completeness we here also want to mention the resulting absolute values of the remaining slab parameters, namely

$$r_x = 188.85nm, r_y = 141.64nm \text{ and } d = 354.09nm. \tag{5.11}$$

An interesting corollary of the simulations of the analyzed structure is an effective visualization of the filter effectiveness. For usual dipole excitation a frequency filtering up to a level of $m_{max,filter} = 7$, corresponding to a frequency window width of $w_{\frac{a}{\lambda},filter,7} = 0.0156$ was usually sufficient. However, the density of modes is significantly increased, which in the case of the chosen structure leads to a quadrupole and dipole mode in very close neighborhood. In figure 5.5 we depicted the corresponding B_z fields after each filtering step. Up to level $m_{filter} = 7$, the window, although centered at the y-dipole frequency, still contains a significant amount of field components of the quadrupole mode. The dipole pattern appears not until we filter up to higher levels and in the end is more or less undisturbed at $m_{max} = 9$, which corresponds to a frequency resolution of

$$w_{\frac{a}{\lambda},filter,9} = 0.0039 \tag{5.12}$$

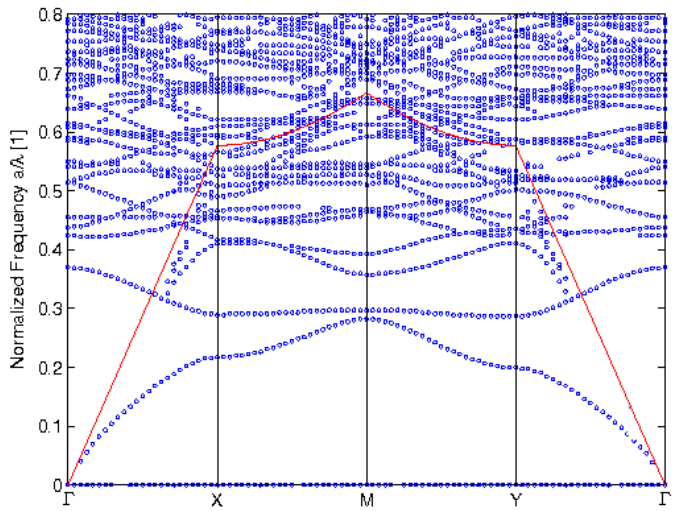

Figure 5.6: Band diagram of a square lattice with $\frac{r_x}{a} = 0.4$ and $\frac{r_y}{a} = 0.3$ along the high symmetry axes of the crystal

Comparing the frequency difference of the quadrupole and the y-dipole mode,

$$\Delta_{\frac{a}{\lambda},modes} = 0.00329, \tag{5.13}$$

we find it in the order of magnitude of the filter width. As the filter is also suppressing spectral components at its edges, the necessity for at least this order of filtering is the expected result.

Before concentrating on the actual quality factor calculation, we afore want to add the full band diagram of a defectless photonic crystal slab with the discussed parameters $\frac{d}{a} = 0.75$, $\frac{r_x}{a} = 0.4$ and $\frac{r_y}{a} = 0.3$. The dispersion diagram is calculated by variation of the applied Bloch boundary $\vec{k}_{||}$ value along the high symmetry axes of the Brillouin zone, which in this case because of the twofold rotational symmetry are ΓX, XM, MY and $Y\Gamma$. The therefore achieved multitude of spectra is subsequently scanned for peaks exceeding a defined threshold. The band diagram itself is depicted in figure 5.6.

5.3 Cavity Quality Factors in a CPCRA Raman Laser

In a resonator array we ideally cope with an infinite array of cavities in the x-y-plane, and even a real structure would be composed of several hundreds of cavities. For a photon leaking out of one cavity, this implies that the probability to leak right into a neighboring cavity is much higher than for leakage out of the array. Moreover, we would be able to implement this array in a surrounding lattice which possesses a full bandgap for exactly the two frequencies supported by our laser array. Both of these facts lead to the conclusion that the effective in-plane quality factor $Q_{||}$ is almost arbitrarily improvable. Therefore in the following quantitative calculation we still want to mention the achieved in-plane quality factors, but nevertheless as a good approximation assume that for the effective total quality factor the in-plane losses and therefore $Q_{||}$ are negligible:

$$Q_{total} \approx Q_{\perp} \tag{5.14}$$

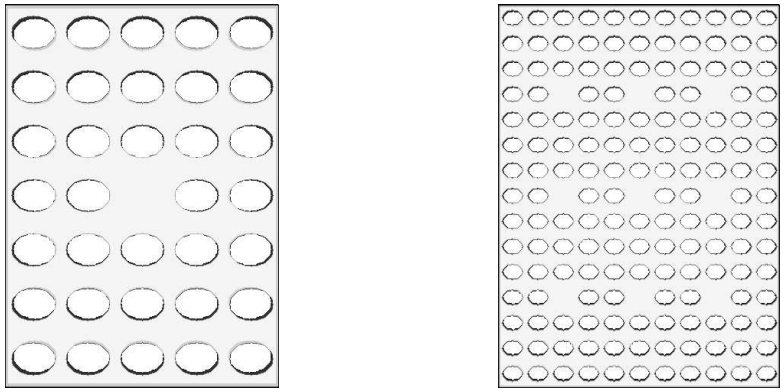

(a) Finite array of a single cavity

(b) Finite array of 3×3 cavities

Figure 5.7: Visualization of two finite two-dimensional CPCRA structures with $l_x = 3$, $l_y = 4$, $\frac{r_x}{a} = 0.4$ and $\frac{r_y}{a} = 0.3$ which we used for the approximation of larger arrays

5.3.1 Approximation of a CPCRA in a Finite Array

As the energy-decay as well as the spatial loss Q-calculation methods from chapter 2.4.3 are both only implemented in the C code of FDTD algorithms with absorbing boundary conditions, we will first approximate an infinite CPCRA with finite arrays of both a single cavity as well as an array of 3×3 resonators, both confined in a surrounding photonic crystal lattice which is equivalent to the distance to the adjacent cavities as depicted in figure 5.7.

The spectra of the single cavity for x- and y-dipole excitation are depicted in figures 5.8(a) and 5.8(c). The central peaks correspond to the single cavity dipole modes of the analyzed structure. Their B_z-fields can been taken from figures 5.8(b) and 5.8(d). Direct analysis of the cavity spectra using

$$Q_{total,1\times1,spectrum} = \left(Q^{-1}_{\perp,1\times1,spectrum} + Q^{-1}_{||,1\times1,spectrum}\right)^{-1} = \frac{\omega_0}{\Delta_\omega} = \frac{\frac{a}{\lambda}}{\Delta_{\frac{a}{\lambda}}}, \tag{5.15}$$

provides the values

$$Q_{total,x,1\times1,spectrum} \approx 38,3 \text{ and } Q_{total,y,1\times1,spectrum} \approx 20.4. \tag{5.16}$$

To improve this estimate, we measure the energy decay in the analyzed finite structure. As plotted for the x-dipole in figure 2.11, we subsequently extract the time constant τ_{norm} from this exponential. Applying

$$Q = \omega_0 \tau = \frac{2\pi c_0}{a}\frac{a}{\lambda_0}\tau = \frac{2\pi}{20}\frac{a}{\lambda_0}\tau_{norm} \tag{5.17}$$

leads to the values

$$Q_{total,x,1\times1,energy} \approx 74.8 \text{ and } Q_{total,y,1\times1,energy} \approx 93.56. \tag{5.18}$$

The best estimate for this single cavity approximation is achieved using the Poynting theorem to measure the loss in real space. Following the steps explained in section 2.4.3 yields the estimates

$$Q_{total,x,1\times1,Poynting} \approx 79.1 \text{ and } Q_{total,y,1\times1,Poynting} \approx 98.6, \tag{5.19}$$

which match pretty well with the estimates achieved by calculation of the energy decay. However, the Poynting-method allows us to separate these total quality factors into in-plane quality factors,

$$Q_{||,x,1\times1,Poynting} \approx 102.8 \text{ and } Q_{||,y,1\times1,Poynting} \approx 123.0, \tag{5.20}$$

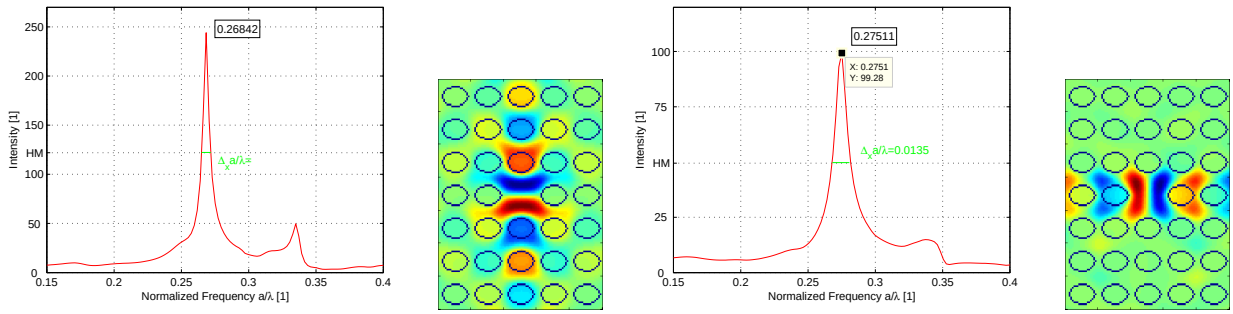

(a) Spectrum x-dipole (b) B_z x-dipole (c) Spectrum y-dipole (d) B_z y-dipole

Figure 5.8: Spectra and B_z-fields of the x- and y-dipole modes in the single-cavity approximation of a CPCRA with $l_x = 3$, $l_y = 4$, $\frac{r_x}{a} = 0.4$ and $\frac{r_y}{a} = 0.3$

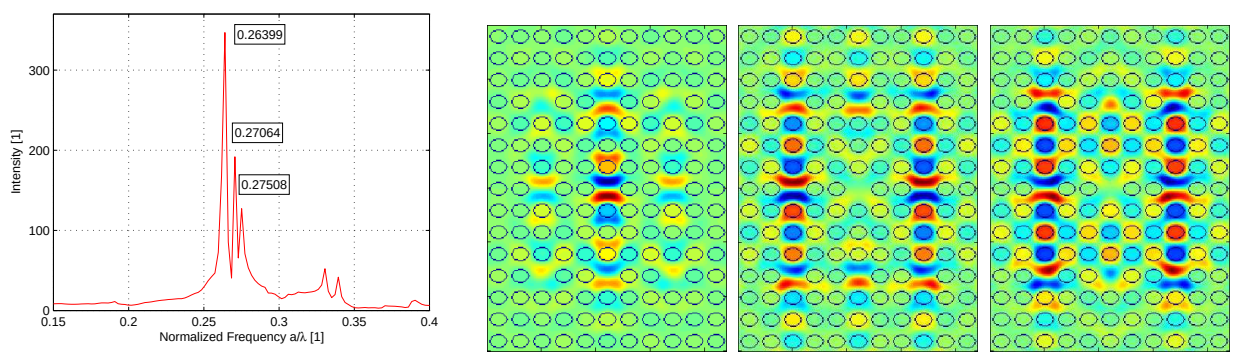

(a) Spectrum (b) B_z at $\frac{a}{\lambda} = 0.26399$ (c) B_z at $\frac{a}{\lambda} = 0.27064$ (d) B_z at $\frac{a}{\lambda} = 0.27508$

Figure 5.9: Spectra and B_z-fields of the x-dipole mode in the single-cavity approximation of a CPCRA with $l_x = 3$, $l_y = 4$, $\frac{r_x}{a} = 0.4$ and $\frac{r_y}{a} = 0.3$

and out-of-plane quality factors,

$$Q_{\perp,x,1\times1,Poynting} \approx 343.2 \text{ and } Q_{\perp,y,1\times1,Poynting} \approx 496.5. \tag{5.21}$$

If we again have a look at the mode profiles depicted in figures 5.8(b) and 5.8(d) we can easily guess the reason for the high in-plane losses: The number of surrounding photonic crystal layers is just not sufficiently large to confine the dipole fields inside the cavity. As an increase in the number of surrounding photonic crystal layers should arbitrarily improve the measured in-plane quality factor, the best estimate for the ideally achievable quality factor with $Q_\perp \approx Q_{total}$ in this single cavity approximation is given by the values in equation 5.21. Note, however, that this estimate is a little too optimistic, as for the calculation of $Q_\perp$ we just take into account losses directly through the top surface of the computational domain. Of course, out-of-plane losses could also possibly occur in an angle which is too flat to hit the top surface inside our computational domain and is thus misinterpreted as in-plane-loss dissipating through the sidewalls.

However, the calculation above is basically just the simulation of a single cavity in an elliptic square lattice. To further focus our estimate on the properties of a CPCRA, but still remain in a computational domain

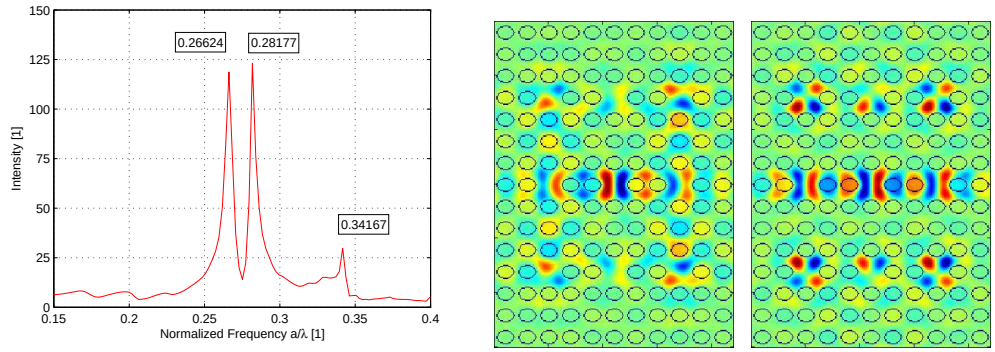

(a) Spectrum (b) B_z at $\frac{a}{\lambda} = 0.26624$ (c) B_z at $\frac{a}{\lambda} = 0.28177$

Figure 5.10: Spectra and B_z-fields of the y-dipole mode in the single-cavity approximation of a CPCRA with $l_x = 3$, $l_y = 4$, $\frac{r_x}{a} = 0.4$ and $\frac{r_y}{a} = 0.3$

surrounded by absorbing boundaries, we increase the number of cavities to the maximum possible square of 3×3. Further increase would cause a computational domain which would be to large to be handled by the applied FDTD and hardware configuration. The spectra and B_z-fields for x- and y-dipole excitation are depicted in figures 5.9 and 5.10, respectively.

Different to the experiment above, and also to experiments with periodic boundary conditions, we here achieve a variety of x- and y-dipole modes. Having a more detailed look at the resulting mode patterns, we observe that this is due to different $\vec{k}_{||}$-values of the observed fields. Still, every cavity supports a dipole mode, but as we just sourced the central cavity with a field of dipole symmetry and did not apply Bloch-boundary conditions, the nine cavities do not oscillate all in phase, but instead posses for example for the x-dipole either a phase difference of π just in x-direction (figure 5.9(b)), just in y-direction (figure 5.9(c)) or in both directions (figure 5.9(d)). For the y-dipole we even observe off-center cavities which seem to be excited at the quadrupole mode.

Note that we actually do not simulate the in-phase case $\vec{k}_{||}=\vec{0}$ we are interested in. Nevertheless, the order of magnitude of the achieved quality factors should still give us an idea of the expected range of Q, so we at least want to mention the achieved results.

Measuring the energy decay yields the total quality factors

$$Q_{total,x,3\times3,energy} \approx (283.3; 275.6; 277.2) \text{ and } Q_{total,y,3\times3,energy} \approx (107.4; 301.6), \tag{5.22}$$

while for the Poynting method the resulting values are

$$Q_{total,x,3\times3,Poynting} \approx (287.4; 283.0; 283.4) \text{ and } Q_{total,y,3\times3,Poynting} \approx (110.4; 306.4). \tag{5.23}$$

The latter can again be separated into the in-plane quality factors,

$$Q_{||,x,3\times3,Poynting} \approx (629.4; 459.7; 438.2) \text{ and } Q_{||,y,3\times3,Poynting} \approx (200.6; 386.4), \tag{5.24}$$

and the out-of-plane quality factors,

$$Q_{\perp,x,3\times3,Poynting} \approx (528.9; 736.4; 802.2) \text{ and } Q_{\perp,y,3\times3,Poynting} \approx (245.2; 1479.2). \tag{5.25}$$

Here the values in each tuple correspond to the modes at

$$\frac{a}{\lambda_x} = (0.26399; 0.27064; 0.27508) \text{ and } \frac{a}{\lambda_y} = (0.26624; 0.28177) \tag{5.26}$$

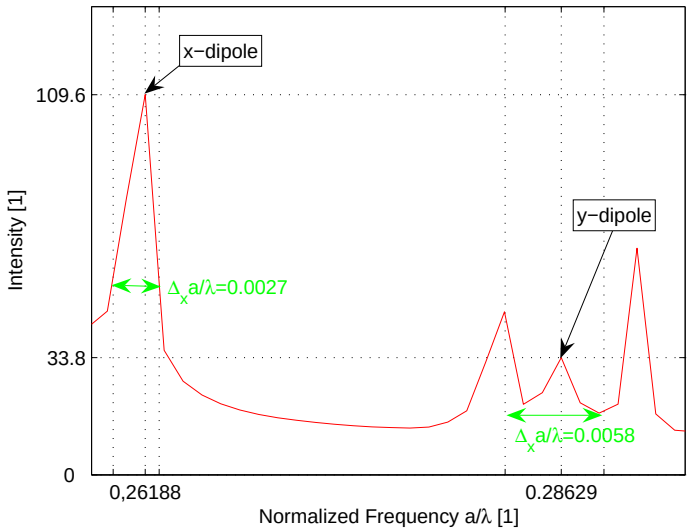

Figure 5.11: Quality factor calculation by measurement of the spectral FWHM of the modes of interest

for the x- and y-dipole modes, respectively.

Note that we generally could enforce the cavities in this 3×3-array to oscillate in phase by application of dipole-like sources in each cavity which are oscillating in phase. However, this excitation scheme is at the moment not supported by the used FDTD code, and as more precise results can be achieved by momentum space analysis of periodic boundary FDTD simulations, we rather want to keep the above estimates as examples for the applied Q-calculation schemes.

5.3.2 Direct Calculation in a CPCRA Simulation with Periodic Boundary Conditions

As we are in fact only interested in the out-of-plane losses, we can also directly perform the quality factor calculation in a simulation with periodic boundary conditions. Here power is only leaking through the top surface of the computational domain. Furthermore we can enforce the desired condition $\vec{k}_{||} = \vec{0}$, which enforces in-phase oscillation of the analyzed resonators. A first rough estimate can again be achieved by analysis of the cavity frequency spectrum. The one discussed here is the same which was depicted in figure 5.4, an enlarged view of the spectrum with focus on the two peaks of interest is depicted in figure 5.11. Using the calculation scheme from equation 5.15 provides the total quality factors

$$Q_{total,x,CPCRA,Spectrum} \approx \frac{0.26188}{0.0027} \approx 97.0 \text{ and } Q_{total,y,CPCRA,Spectrum} \approx \frac{0.28629}{0.0058} \approx 49.4, \tag{5.27}$$

which in this case of periodic boundaries of course equal the out-of-plane quality factors. Note that here especially the FWHM value of the pump-mode, i.e., of the y-dipole, can just be treated as a rough estimate as the dipole peak itself notedly overlaps with the quadrupole peak as discussed in the previous section.

To get a better estimate for the actual Q-factors, we need to change the method of calculation. As mentioned in the previous section, the energy-decay and also the Poynting method as implemented in the available FDTD code are not compatible with the use of periodic boundary conditions. However, loss calculation in momentum space in this case provides the far most accurate method, as it exactly calculates just the out of plane losses and is moreover applied directly on the modes of interest, i.e., the x- and y-dipole

modes of a CPCRA at $\vec{k}_{||} = \vec{0}$. By combining the power calculation scheme from equation 2.77 with the Q calculation from 2.65 and using the energy calculation formula 2.68 we achieve the following values:

$$Q_{total,x,CPCRA,momentum} \approx 752.7 \text{ and } Q_{total,y,CPCRA,momentum} \approx 441.2, \tag{5.28}$$

These results are approximately one order of magnitude higher than the ones achieved via spectral analysis of the same structure. However, they match roughly with the results achieved by measuring the energy decay and the loss in a finite array as described in the previous section. Moreover, the values of equation 5.28 contain no rough approximations, they really analyze the exact mode of interest as we applied periodic boundary conditions and they are composed of just the out-of-plane losses, i.e., the losses due to field components inside the light cone.

Thus we want to keep

$$Q_{total,x} \approx 752.7 \text{ and } Q_{total,y} \approx 441.2, \tag{5.29}$$

as the final quality factor estimates of the analyzed modes and we will use these values for the subsequent calculation of the lasing threshold of the examined CPCRA Raman laser design.

5.4 The Effective Modal Volume

The lasing threshold equation 2.24 contains the factor ξ, which we introduced as the modal intensity overlap. The process of stimulated Raman scattering has been described as a gain of the Stokes intensity dependent on the incident and in the cavity accumulated pump intensity. However, the physical process of Raman scattering is, of course, spatially dependent on an overlap of the pump- and Stokes modes. However, the threshold equation also contains the factor V_m, the modal volume. Instead of calculating both values separately, we rather integrate the overlap over the two involved intensity patterns and normalize it by the separate intensity integrals of both modes, yielding an expression for the desired quotient $\frac{\xi}{V_m}$. This quotient defines the *effective modal volume* V_{eff} [14]:

$$V_{eff}^{-1} = \frac{\xi}{V_m} = \frac{\int \alpha(\vec{r}) \left|\vec{E}_s(\vec{r})\right|^2 \left|\vec{E}_p(\vec{r})\right|^2 dV}{\int \left|\vec{E}_s(\vec{r})\right|^2 dV \int \left|\vec{E}_p(\vec{r})\right|^2 dV} \tag{5.30}$$

Here we assumed the overlap outside of one cavity to vanish, so the overall integral equals the former approximated modal volume of equation 2.19, $V_m = d \cdot A$. The factor α takes the two values

$$\alpha|_{air} = 0 \text{ and } \alpha|_{Si} = 1 \tag{5.31}$$

and represents the fact that Raman scattering can only occur inside the gain medium, which in this case is silicon.

Performing this calculation over the volume of the slab for the modal patterns of the x- and y-dipole modes of the Raman laser design over one unit cell yields the result

$$V_{eff,unitcell}^{-1} = \frac{1}{2} 3.063 \cdot 10^{-5} \frac{1}{(\Delta x)^3} \tag{5.32}$$

and thus an effective modal volume of

$$V_{eff,unitcell} = 0.859 \mu m^3 \tag{5.33}$$

where $\Delta x = \frac{a}{20} = 23.6nm$ and the factor $\frac{1}{2}$ represents the fact that we are only integrating over the upper half of the CPCRA unit cell.

The effective modal volume volume of a real CPCRA structure, however, increases with the number of cavities in the finite coupled photonic crystal resonator array laser N_c as

$$V_{eff,CPCRA} = N_c \cdot V_{eff,unitcell}. \tag{5.34}$$

5.5 Influence of Free Carriers from Two-Photon Absorption

For the derivation of the lasing threshold equation in a single cavity as given in chapter 2.1 we assumed that all other absorption processes besides the unavoidable cavity loss are negligible. Before continuing with the threshold equation for a CPCRA Raman laser, we first want to justify this assumption with respect to free carrier absorption. Along an interaction length r the loss of the pump intensity can be described as [11]

$$\frac{dI_p(z)}{dz} = -(\alpha_{lin} + \alpha_{rad} + g_R + \alpha_{FCA})I_p(z) - \beta_{TPA}I_p^2(z). \tag{5.35}$$

While we want to neglect the linear losses, represented by α_{lin}, as well as the radiation losses α_{rad} and desired losses due to Raman scattering, described by g_R, we need to have a closer look at the losses due to free carrier absorption (FCA) and two-photon absorption (TPA), represented by α_{FCA} and β_{TPA}, respectively. The TPA-coefficient of silicon has a value of $\beta_{TPA} \approx 0.5\frac{cm}{GW}$ [4], which causes the amount of loss due to the two-photon absorption itself to be sufficiently small at moderate pump intensities. However, the induced carriers lead to additional loss owing to the free carrier plasma dispersion effect, known as free carrier absorption. In a steady state, the FCA absorption coefficient is proportional to the total TPA-absorbed optical power on the one hand, but on the other hand also to the free carrier lifetime in the cavity [11]:

$$\alpha_{FCA} \propto \tau_{eh}P_{TPA} \tag{5.36}$$

As reported recently, possible output powers of SOI waveguide Raman amplifiers are significantly reduced for input powers of $P_{in} \approx 1W$ and free carrier lifetimes higher than $\tau_{eh} = 1ns$ [9]. However, the carrier lifetime in a 2D photonic crystal slab is supposed to be sufficiently low because of fast surface recombination due to the roughly etched hole sidewalls. We first want to neglect possible influences of defects to estimate the carrier lifetime in an undisturbed photonic crystal slab as [40]

$$\frac{1}{\tau_{eh,PhC}} = v_s R \tag{5.37}$$

with the *surface recombination velocity* v_s and the *surface area density* $R = \frac{surface}{volume}$. The value of the surface recombination velocity depends strongly on the material, which in our case is silicon, as well as on the density of surface states, which in the case of a photonic crystal slab is expected to be much higher at the rough etched hole sidewalls than at the top and bottom of the photonic crystal slab. Thus equation 5.37 can be rewritten as

$$\frac{1}{\tau_{eh,PhC}} = v_{s0,slab}R_{slab} + v_{s,holes}R_{holes} = v_{s,slab}\frac{1}{d} + v_{s,holes}\frac{\pi(3(r_x + r_y) - \sqrt{(3r_x + r_y)(r_x + 3r_y)})}{a^2} \tag{5.38}$$

where we used the Ramanujan approximation

$$c_{ell} = \pi(3(r_x + r_y) - \sqrt{(3r_x + r_y)(r_x + 3r_y)}) \tag{5.39}$$

to calculate the circumfence c_{ell} of the elliptical holes. Typical values of v_s for silicon can be found in a range of [41]:

$$v_s \in [10^2; 8 \cdot 10^4]\frac{cm}{s} \tag{5.40}$$

As reported in [40], the etched sidewall surface recombination velocity in photonic crystals actually almost reaches its material maximum due to the rough sidewalls. Using values of $v_{s,slab} = 10^3\frac{cm}{s}$ and $v_{s,holes} = 5 \cdot 10^4\frac{cm}{s}$ for the surface recombination velocities and the slab parameters from section 5.2 we estimate a surface carrier recombination rate of

$$\frac{1}{\tau_{eh,PhC}} = 28.24 \cdot 10^6\frac{1}{s} + 2.34 \cdot 10^9\frac{1}{s} \approx 2.37 \cdot 10^9\frac{1}{s} \tag{5.41}$$

which implies a carrier lifetime due to surface recombination of

$$\tau_{eh,PhC} = 0.42ns. \tag{5.42}$$

This lifetime, calculated for an undisturbed photonic crystal slab using the parameters of our CPCRA laser design changes due to two effects by introducing the cavity defects in a CPCRA structure:

First of all the overall hole surface density reduces to

$$R_{holes,CPCRA} = \frac{N_{CPCRA}}{N_{PhC}} = \frac{11}{12} \tag{5.43}$$

where N_i is the number of holes per unit cell of each structure. Including this correction term yields:

$$\tau_{eh,CPCRA} = 0.46ns \tag{5.44}$$

Second, carriers are not all generated directly at the surface. However, assuming the maximal way of a carrier to the next surface as $L_{surf} \approx \frac{a}{2}$ results in a diffusion time to the surface of:

$$\tau_{Diff} = \frac{L_{Surf}^2}{6D_{Si}} = \frac{L_{Surf}^2}{6\frac{k_B T \mu}{q}} = 9.3ps \tag{5.45}$$

Here we assumed an average carrier mobility in silicon of $\mu = 400\frac{cm^2}{Vs}$ and a value of $\frac{k_B T}{e} \approx 25mV$ at room temperature. As this value is almost two orders of magnitude smaller than the estimate for $\tau_{eh,CPCRA}$, we can effectively neglect the contributions of diffusion to the carrier lifetime.

The rather small carrier lifetime of less than half a nanosecond is sufficiently small to keep free carrier absorption negligibly small up to pump power levels of several watts as can be extrapolated from [9] and [10]. However, if the effective local pump power per cavity significantly exceeds this value, TPA induced FCA could become important. Therefore a more detailed analysis needs to be achieved by later experimental realization of the proposed CPCRA laser design.

5.6 Results and Discussion

In chapter 2.1.3 we derived the Raman lasing threshold equation 2.24 for a single cavity, which shall be repeated here for the sake of convenience:

$$P_{p,threshold} = \frac{(2\pi n_c)^2 V_m}{\xi g_s \lambda_s \lambda_p Q_s Q_p} \tag{5.46}$$

Using the concept of the effective modal volume from section 5.4, we can rewrite this equation for the unit cell of a CPCRA as

$$P_{p,threshold,unitcell} = \frac{(2\pi n_c)^2 V_{eff,unitcell}}{g_s \lambda_s \lambda_p Q_s Q_p} \tag{5.47}$$

With the determined parameters of $n_c = 11.5$, $V_{eff,unitcell} = 0.859\mu m^3$, $g_s = 50\frac{cm}{GW}$, $\lambda_p = 1.69\mu m$, $\lambda_s = 1.80\mu m$, $Q_s = 752.7$ and $Q_p = 441.2$ we achieve an estimate value of the lasing threshold in a CPCRA unit cell of

$$P_{p,threshold,unitcell} \approx 8.88W \tag{5.48}$$

Because of the expected increase of the effective mode volume, this value is supposed to rise even further in a resonator array with N_c cavities as

$$P_{p,threshold,CPCRA} \approx N_c P_{p,threshold,unitcell}. \tag{5.49}$$

However, while the lasing power threshold increases with the number of resonant cavities, the intensity threshold remains constant:

$$I_{p,threshold,CPCRA} = \frac{P_{p,threshold,CPCRA}}{A_{eff,CPCRA}} = \frac{N_c P_{p,threshold,unitcell}}{N_c A_{eff,unitcell}} = I_{p,threshold,unitcell} = 332 \frac{MW}{cm^2} \quad (5.50)$$

In the experimental realization of the analyzed CPCRA laser design, even the effectively higher power threshold of the resonator array will be partly compensated by the fact that the larger x-y-area of the CPCRA is much more efficiently pumpable at these power levels than the x-y-area cross section of a single cavity or the small cross-section of a sub-micron SOI-waveguide.

Nevertheless, the resulting threshold values, even for a single unit cell, are roughly two order of magnitude larger than the ones projected in [15], which is mainly due to the significantly reduced out-of-plane quality factor in the analyzed CPCRA structure. If no significant improve of the structure's quality factors is possible, we will have to come to the conclusion that Raman scattering offers a too low optical gain to be applied on a CPCRA laser structure design at telecommunication wavelengths.

6 Conclusions

The afore presented work investigated the possibilities of achieving an all-silicon Raman laser realized in a two-dimensional coupled photonic crystal microcavity array.

We gave a detailed analysis of the frequential tunability of the dipole modes in a CPCRA structure by means of the inter-cavity barrier, the hole radius and the hole eccentricity and moreover of the interaction of these three parameters. Besides the mode frequencies, possible quality factors of those modes have as well been addressed as the effective modal volumes.

More general, and independent of any focus on a special type of modes, we additionally examined the properties and especially the band structure of a square lattice of elliptical air holes in a silicon photonic crystal slab.

As a second corollary, a theoretic analysis of possible free-carrier absorption due to free carriers from two-photon absorption in a silicon photonic crystal has been given. The results have been directly applied on a CPCRA structure and the free-carrier lifetime moreover been interpreted in terms of its influence on the lasing threshold in a CPCRA laser design.

Being the actual core of this thesis, we have finally also derived a lasing threshold equation for a CPCRA Raman laser and have estimated the lasing threshold of one possible laser design. However, the achieved lasing threshold results have been unsatisfactory. It turned out that the achievable quality factors in the examined CPCRA structure are generally too low to be applied on a lasing process with such as low gain coefficients as stimulated Raman scattering.

To enhance the proposed structure design, further improvement of the modal quality factors would be essential. Besides by analysis of different defect modes, a variable angle of incidence, the switch to another lattice type like the triangular or rectangular lattice, a change of the introduced cavity type or a variable slab thickness as proposed in chapter 4.3.2, a direct optimization of the quality factors would be possible either by introduction of small hole perturbations and subsequent analysis of the quality factors, or more systematically by quality factor optmization in momentum space as proposed in [29].

Nevertheless, all the above mentioned results, except the ones directly concerning stimulated Raman scattering, remain applicable on any other implementable gain process. As for example a CPCRA laser in InP has been achieved recently [19], the here reported results could soon become important for the development of other CPCRA lasers. As the CPCRA structure provides a large area and number of actually lasing cavities, it seems especially be usefull for high power applications as for example frequency converters for industrial welding lasers rather than for relatively low power applications at telecommunication wavelengths.

A FDTD Simulation Files

To control the simulation process and to finally achieve the computer simulated results which we have discussed throuout this thesis, a couple of script files have been used. The sourec code of these script files is presented here for the sake of completeness.

A.1 Creation of the Structure Files

The following TCL source has been used to create the data files which represented the properties of the simulated structure as explained in section 4.1(1):

```
# Load a TCL source which itself loads the C++ sources
source ./fab3d_start.tcl

# Define material Parameters
set PI 3.1415926
set n_air 1.0
set ep_air [expr pow($n_air,2)]
set sg_air 0
set n_Si 3.4
set ep_Si [expr pow($n_Si,2)]
set sg_Si 0

# Set structure parameters
set a 20; # the number of points per a, to choose even, odd not tested
set r 6; # radius of a hole
set core_half_thick 6;
set air_top_th 81

# Set numbers of layers of the unit cell in x and y
set layersx 2
set layersy 3

# Set the size of the Ellipses
set radius2 2

# Allow transfer of parameters from the command line
foreach {arg val} $argv {
set temp $arg
set $temp $val
}

set nx [expr $a*$layersx]
set ny [expr $a*$layersy]
```

```
set nz [expr $air_top_th+$core_half_thick]
set structure [fabAllocateStructure $nx $ny $nz]

# Set the background to air
fabSelectAll $structure
fabSetEpsilon $structure $ep_air
fabSetSigma $structure $sg_air
fabSetMetal $structure 1
fabClearSelection $structure

## CREATE THE UNIT CELL

#  Create the slab
set x 0
set y 0
set z 0
set width $nx
set depth $ny
set height [expr $core_half_thick];
fabSelectRectangle 1 $structure $x $y $z $width $depth $height
fabSetEpsilon $structure $ep_Si
fabSetSigma $structure $sg_Si
fabClearSelection $structure

# Create the holes in the slab
set z 0
set radius [expr $r]
set centerx $nx/2
set centery $ny/2

# Select the lines
for {set vert [expr round(ceil($layersy/2))]} {$vert+1} {incr vert -1} {

# Select the holes in each line
    for {set horiz [expr round(ceil($layersx/2))]} {$horiz+1} {incr horiz
       -1} {

        # Right part
        set x [expr $centerx+$horiz*$a]
        # Ellipse hole
        set y [expr $centery+$vert*$a]
        fabSelectEllipse 1 $structure $x $y $z 0 0 1 $radius $radius2
        set y [expr $centery-$vert*$a]
        fabSelectEllipse 1 $structure $x $y $z 0 0 1 $radius $radius2

        # Left part
        set x [expr $centerx-$horiz*$a]
        # Ellipse hole
```

```
        set y [expr $centery+$vert*$a]
        fabSelectEllipse 1 $structure $x $y $z 0 0 1 $radius $radius2
        set y [expr $centery-$vert*$a]
        fabSelectEllipse 1 $structure $x $y $z 0 0 1 $radius $radius2
    }
}

# Deselect the cavity-hole
set x [expr $centerx]
set y [expr $centery]
fabSelectEllipse 0 $structure $x $y $z 0 0 1 $radius $radius2

# Create the holes
fabSetEpsilon $structure $ep_air
fabSetSigma $structure $sg_air
fabClearSelection $structure

# Save the structure
set structure_name [format "./PBG_CCav_square_lx%d_ly%d_rx%d_ry%d.crystal"
    $layersx $layersy $radius $radius2]
fabSaveStructure $structure $structure_name
set structure_vtk_name [format "./PBG_CCav_square_vtk_lx%d_ly%d_rx%d_ry%
   d.crystal" $layersx $layersy $radius $radius2]
fabSaveStructureVtk $structure $structure_vtk_name $ep_air

# Free up allocated memory
fabFreeStructure $structure

# Define and save the incident field
set field [fabAllocateField $nx $ny $nz]
set pos_x [expr $centerx-2];
set pos_y [expr $centery-1];
fabGaussianField $field $pos_x $pos_y 0 1 1 1 0 0 0 [expr $a/2] [expr $a
   /2] $core_half_thick 0 0 0 1 1 1;
set field_name [format "./I_PBG_CCav_square_lx%d_ly%d_rx%d_ry%d.crystal"
   $layersx $layersy $radius $radius2]
fabSaveField $field $field_name
fabSaveMagneticFieldVtk $field [format "./B_PBG_CCav_square_lx%d_ly%d_rx%
   d_ry%d.vtk" $layersx $layersy $radius $radius2]
fabFreeField $field
```

A.2 Three-dimensional Plotting of the Fabricated Structures

For the purpose of three-dimensional plotting of the structures as discussed in chapter 4.1(2), this TCL source has been used:

```
#!/usr/bin/vtk
# Load in plotting library and initialize
```

```
source /usr/local/bin/FDTD/plotbin/VTK_plots.tcl
vtkMakeRenderer ren renWin iren

# Load in data files
set struct_file PBG_structure_vtk.crystal
vtkLoadData $struct_file struct_data

set field_file B.vtk
vtkLoadData $field_file field_data

# Make the plots
set threshold .4
set scale_factor 5
vtkMakeVectorPlot field_data $threshold $scale_factor ren

set ep_contour 2
set color $white_smoke
set opacity .8
vtkMakeStructurePlot struct_data $ep_contour $color $opacity ren

set outline_color $black
vtkMakeOutline struct_data $outline_color ren

# Render the image
set background_color $white
set window_height 400
set window_width 400
vtkRenderImage ren renWin iren $background_color $window_height
   $window_width
```

A.3 FDTD Time Evolution

Here the TCL source which has been used to control the properties of the FDTD time evolution from chapter 4.1(3) is presented:

```
#!/usr/bin/tclsh
source ./ffdtd3d_start.tcl

# Parameters of the structure
set pi 3.1415926;
set a 20;
set core_half_thick 6;
set air_top_th 81;
set layersx 3;
set layersy 4;
set nx [expr $a*$layersx]
set ny [expr $a*$layersy]
set nz [expr $air_top_th+$core_half_thick]
```

```
# Set the boundary conditions
set type_xn 3; # Bloch
set type_xp 3; # Bloch
set type_yn 3; # Bloch
set type_yp 3; # Bloch
set type_zn 2; # Mirror
set type_zp 4; # Mur
set Xn 1;  # doesn't matter
set Xp 1;
set Yn 1;
set Yp 1;
set Zn 1;  #to select EVEN modes - mirror is in the center of the slab
set Zp -1; #always this value - supercell approx.
set kx 0
set ky 0
set kz 0

# Parameters for the time evolution
set dt .55;
set dT 1.1;
set T [expr 18023]; #gives 2^14 points in time (dT=1.1)
set numpoints 2; # (numpoints x numpoints) array of points saved at each
   time step
set x [expr ceil(0.9*$nx)]; # width of point region saved at each time
   step
set y [expr ceil(0.9*$nx)];
set z [expr ceil(0.5*$core_half_thick)];

# File names
set structure_name structure.crystal #simulated structure file
set name time_evolution.dat #time evolution file
set field_evolved field_evolved.dat #resulting field at the end of the
   evolution

# Create solution structure and allocate memory
set solution [fdtNewSolution]

# Intitialize the boundary conditions
fdtInitializeBoundaries $solution $type_xn $type_xp $type_yn $type_yp
   $type_zn $type_zp $Xn $Xp $Yn $Yp $Zn $Zp $kx $ky $kz

# Load in the dielectric structure
fdtLoadStructure $solution $structure_name

# Load field
set field_name I.test
fdtLoadField $solution $field_name $dt
```

```
# Evolve the solution over time and save time series
fdtSaveTimeEvolution3 $solution $name $dt $dT $T $x $y $z $numpoints
   $numpoints 1;

# Save the resulting field distribution
fdtSaveField $solution $field_evolved;

#Free allocated memory
fdtFreeSolution $solution
```

A.4 Spectral Analysis of the Time Evolution Results

The spectral analysis of the modes of interest has been performed using MATLAB® as described in chapter 4.1(4):

```
% Reset Matlab
clear all;
close all;

% Parameters of the structure
layersx=3;
layersy=4;
npoints_a=20;

% Parameters of the time evolution
numpoints=4; %(numpoints=numpoints_fdtd)^2

% Parameters for the plots
freqrange=0.5; % Frequency range to search in normalized units

% Import of the time-evolution file and creation of equivalent matrices
fid=fopen(sprintf('time_evolution.dat'),'r+');
[P1,C]=fscanf(fid,'%f',[numpoints*3,inf]);
P=transpose(P1); % The time evolution values
C=size(P,1)-1; % Number of plotable points
fclose(fid);

% Discrete Fourier Transform (DFT) of our time evolution data
fftP=abs(fft(P,C));
fft_sum_amplitude=sum(fftP,2);
peak=max(max(fft_sum_amplitude(10:C,1:))); % Search maximum value for axes
    scales

% Create matrix for the frequency axis
f_normal=(npoints_a/1.1/C*linspace(0,C-1,C))';

%% PLOTTING OF THE SPECTRUM
```

```
% Create plot
h=figure;
hold on;
plot(f_normal,fft_sum_amplitude);
title(sprintf('Figure␣lx%d␣ly%d␣rx%d', layersx, layersy));

% Prepare peaks detection
diffybaby=diff(fft_sum_amplitude);
prag=20; % Threshold value for peaks

% Detect and label the peaks
for i=1:(C-2)
        if (sign(diffybaby(i,1))>0 & sign(diffybaby(i+1,1))<=0 &
           fft_sum_amplitude(i+1,1)>prag & (f_normal(i+1,1)<freqrange))
        text(f_normal(i+1,1),fft_sum_amplitude(i+1,1)+30,num2str(f_normal(
           i+1,1)));
        end;
end;

% Scale and label the axes
axis ([0.12 (freqrange) 0 1.3*peak]);
xlabel ('a/\lambda');
ylabel ('Intensity');
grid;

% Save the figures
saveas(h, sprintf('Figure_ydip_lx%d_ly%d.eps', layersx, layersy), 'eps');
saveas(h, sprintf('Figure_ydip_lx%d_ly%d.jpg', layersx, layersy), 'jpg');
saveas(h, sprintf('Figure_ydip_lx%d_ly%d.fig', layersx, layersy), 'fig');
```

A.5 Filtering at Modes of Interest

Subsequent bandpass filtering of the modes was achieved using again a TCL script as explained in section 4.1(5):

```
#!/usr/bin/tclsh
source ./ffdtd3d_start.tcl

# Parameters of the structure
set pi 3.1415926
set a 20

# Set the boundary conditions
set type_xn 3; # Bloch
set type_xp 3; # Bloch
set type_yn 3; # Bloch
set type_yp 3; # Bloch
set type_zn 2; # Mirror
```

```
set type_zp 4; # Mur
set Xn 1; #doesn't matter
set Xp 1;
set Yn 1
set Yp 1
set Zn 1; # to select EVEN modes - mirror is in the center of the slab
set Zp -1; # always this value - supercell approx.
set ky 0
set kx 0
set kz 0

# Parameters of the filtering process
set normf 0.3329
set W [expr 2*$pi/$a*$normf]
set filters {1 1 2 3 4 5 6)
set filters_at_W 7
set dt .55

# File names
set initial_field field_evolved.dat
set struct_name structure.crystal
set field_filtered field_filtered.dat

# Create solution structure and allocate memory
set solution [fdtNewSolution]
fdtInitializeBoundaries $solution $type_xn $type_xp $type_yn $type_yp
   $type_zn $type_zp $Xn $Xp $Yn $Yp $Zn $Zp $kx $ky $kz

# Load in the dielectric structure
fdtLoadStructure $solution $struct_name

# Load field
fdtLoadField $solution $initial_field $dt

# Frequency filtering by convolution in time-space
fdtFilterSet $solution $filters $W $filters_at_W $dt

# Save the resulting field distribution
fdtSaveField $solution $field_filtered

# Free allocated memory
fdtFreeSolution $solution
```

A.6 Spatial Analysis of the Time Evolution Results

For two-dimensional spatial visualization of the modes of interest as discussed in chapter 4.1(6) the following MATLAB® source has been used:

```
% Written by Marko Loncar

% Reset Matlab
clear all;
close all;

a=20;
z=1; % x-y-plane at the center of the slab
number_of_copies_X=3; % number of plotted unit cells in x-direction
number_of_copies_Y=3; % number of plotted unit cells in y-direction

mirror=1; % even mirror boundary at z=0

% X POINT!
x=pi/a

%Gamma-Point
kx=0
ky=0

%%%%%%%%%%%%%%%%%%%%%%% MANIPULATE THE FIELD %%%%%%%%%%%%%%%%%%%%
% Load the Field File
fid=fopen((sprintf('./field_filtered.dat')),'r+');
tmp=fscanf(fid,'%s',1);
dimensions=fscanf(fid,'%f',3)
tmp=fscanf(fid,'%s',19);
disp('loading␣field...');
[P C]=fscanf(fid,'%f',[18,inf]);
fclose(fid);

% Form complex E and B fields
P=P(1:6,:)+i*P(10:15,:);

% Take the slice @ z=?
slice_size=dimensions(1)*dimensions(2); % x*y
startz=(z-1)*slice_size;

P=P(:,startz+1:startz+slice_size);

matrica=[];
for j=1:dimensions(2),
  matrica=[matrica; P(:,(j-1)*dimensions(1)+1:j*dimensions(1))];
end;

% First in x direction
phase_x=exp(i*kx*a);
phase_y=exp(i*ky*a);
```

```
temp=[];
for j=1:number_of_copies_X,
   temp=[temp matrica*phase_x^(j-1)];
end;

matrica=temp;

temp=[];
for j=1:number_of_copies_Y,
   temp=[temp; matrica*phase_y^(j-1)];
end;

matrica=temp;

% Form matrices for components of E and B fields
matrica_Ex=[];
matrica_Ey=[];
matrica_Ez=[];
matrica_Bx=[];
matrica_By=[];
matrica_Bz=[];
for j=1:dimensions(2)*number_of_copies_Y,
  matrica_Ex=[matrica_Ex; real(matrica(6*(j-1)+1,:))];
  matrica_Ey=[matrica_Ey; real(matrica(6*(j-1)+2,:))];
  matrica_Ez=[matrica_Ez; real(matrica(6*(j-1)+3,:))];
  matrica_Bx=[matrica_Bx; real(matrica(6*(j-1)+4,:))];
  matrica_By=[matrica_By; real(matrica(6*(j-1)+5,:))];
  matrica_Bz=[matrica_Bz; real(matrica(6*(j-1)+6,:))];
end;

matrica_Eampl=matrica_Ex.^2+matrica_Ey.^2+matrica_Ez.^2;
matrica_Bampl=matrica_Bx.^2+matrica_By.^2+matrica_Bz.^2;

matrica_Eampl=matrica_Eampl/max(max(abs(matrica_Eampl)));
matrica_Bampl=matrica_Bampl/max(max(abs(matrica_Bampl)));

max_E=max([max(max(abs(matrica_Ex))) max(max(abs(matrica_Ey))) max(max(abs
   (matrica_Ez)))])
max_B=max([max(max(abs(matrica_Bx))) max(max(abs(matrica_By))) max(max(abs
   (matrica_Bz)))])

matrica_Ex=matrica_Ex/max_E;
matrica_Ey=matrica_Ey/max_E;
matrica_Ez=matrica_Ez/max_E;
matrica_Bx=matrica_Bx/max_B;
matrica_By=matrica_By/max_B;
matrica_Bz=matrica_Bz/max_B;
```

```
%%%%%%%%%%%%%%%%%%%%%%%%%%%%%%% END OF THE FIELD MANIPULATION %%%%%%%%%%

%%%%%%%%%%%%%%%%%%%%%%%%%%%%%% STRUCTURE MANIPULATION %%%%%%%%%%%%%%%%%

% Load the structure
disp('loading structure...');
fid=fopen(sprintf('./structure.crystal'),'r+');
tmp=fscanf(fid,'%s',12);
dimensions2=fscanf(fid,'%f',3)
tmp=fscanf(fid,'%s',15);
disp('loading structure...');
[P C]=fscanf(fid,'%f',[1,inf]);
fclose(fid);

disp('calculating...');

slice_size=dimensions2(1)*dimensions2(2); % x*y
startz=z*slice_size;   % since structure is bigger than the field (due to
   added boundary points)

P=P(startz+1:startz+slice_size);

structure=[];
  for j=2:dimensions2(2)-1,
    structure=[structure; P((j-1)*dimensions2(1)+2:j*dimensions2(1)-1)];
  end;

temp=[];

for j=1:number_of_copies_X,
   temp=[temp structure];
end;

structure=temp;
temp=[];
for j=1:number_of_copies_Y,
   temp=[temp; structure];
end;
structure=temp;

ivice=edge(structure,'canny');
s=size(ivice);
for j=1:s(1),
  for i=1:s(2),
     if ivice(j,i)==1,
       matrica_Ex(j,i)=-1;
       matrica_Ey(j,i)=-1;
       matrica_Ez(j,i)=-1;
```

```
        matrica_Eampl(j,i)=0.5;
        matrica_Bx(j,i)=-1;
        matrica_By(j,i)=-1;
        matrica_Bz(j,i)=-1;
        matrica_Bampl(j,i)=0.5;
      end;
  end;
end;

range=[-1,1];

% Plot fields and structures
figure;
for loop=1:3,
  subplot(3,1,loop);
  if loop == 1, imagesc(matrica_Ex,range), title('Ex␣field');end;
  if loop == 2, imagesc(matrica_Ey,range), title('Ey␣field');end;
  if loop == 3, imagesc(matrica_Ez,range), title('Ez␣field');end;
  axis equal;
  axis tight;
end;
colorbar('horis');
print -depsc E_fields.eps
print -djpeg E_fields.jpg

figure;
imagesc(matrica_Eampl,[0 1]);
title('Amplitude␣of␣E␣field');
axis equal;
axis tight;
colorbar('horis');
print -depsc E_amplitude.eps
print -djpeg E_amplitude.jpg

figure;
for loop=1:3,
  subplot(3,1,loop);
  if loop == 1, imagesc(matrica_Bx,range), title('Bx␣field');end;
  if loop == 2, imagesc(matrica_By,range), title('By␣field');end;
  if loop == 3, imagesc(matrica_Bz,range), title('Bz␣field');end;
  axis equal;
  axis tight;
end;
colorbar('horis');
print -depsc B_fields.eps
print -djpeg B_fields.jpg

figure;
```

```
imagesc(matrica_Bampl,[0 1]);
title('Amplitude␣of␣B␣field');
axis equal;
axis tight;
colorbar('horis');
print -depsc B_amplitude.eps
print -djpeg B_amplitude.jpg

figure;
imagesc(matrica_Bz,range);
title('Bz␣field');
axis equal;
axis tight;
colorbar('horis');
print -depsc Bz.eps
print -djpeg Bz.jpg
```

Bibliography

[1] Archimedes. Wikiquote. Retrieved December 30, 2005, http://de.wikiquote.org/wiki/Archimedes.

[2] V. R. Almeida, C. A. Barrios, R.R. Panepucci, and M. Lipson. All-optical Control of Light on a Silicon Chip. *Nature*, 431:1081 – 1084, Oct 2004.

[3] O. Boyraz and B. Jalali. Demonstration of a Silicon Raman Laser. *Optics Express*, 12(21):5269 – 5273, Oct 2004.

[4] R. Claps, D. Dimitropoulos, V. Raghunathan, Y. Han, and B. Jalali. Observation of stimulated raman amplification in silicon waveguides. *Optics Express*, 11(15):1731 – 1739, July 2003.

[5] R. Claps, D. Dimitropoulos, Y. Han, and B. Jalali. Observation of raman emission in silicon waveguides at 1.54 mm. *Optics Express*, 10(22):1305 – 1313, November 2002.

[6] D. Dimitropoulos, B. Houshmand, R. Claps, and B. Jalali. Coupled-mode theory of the raman effect in silicon-on-insulator waveguides. *Optics Letters*, 28(20):1954 – 6, Oct 2003.

[7] D. Dimitropoulos, R. Claps, Y. Han, and B. Jalali. Nonlinear optics in silicon waveguides: Stimulated raman scattering and two-photon absorption. In *Proceedings of the SPIE - The International Society for Optical Engineering*, volume 4987, pages 140 – 8, 2003.

[8] R. L. Espinola, J. I. Dadap, R. M. Osgood Jr., S. J. McNab, and Y. A. Vlasov. Raman Amplification in Ultrasmall Silicon-on-insulator Wire Waveguides. *Optics Express*, 12(16):3713–3718, Aug 2004.

[9] R. Jones, H. Rong, A. Liu, A. Fang, M. Paniccia, D. Hak, and O. Cohen. Net Continuous Wave Optical Gain in a Low Loss Silicon-on-insulator Waveguide by Stimulated Raman s Scattering. *Optics Express*, 13:519 – 525, Jan 2005.

[10] H. Rong, A. Liu, R. Jones, O. Cohen, D. Hak, R. Nicolaescu, A. Fang, and M. Paniccia. An All-silicon Raman Laser. *Nature*, 433:292 – 294, Jan 2005.

[11] T. K. Liang and H. K. Tsang. Role of Free Carriers from Two-photon Absorption in Raman Amplification in Silicon-on-insulator Waveguides. *Applied Physics Letters*, 84(15):2745 – 2747, April 2004.

[12] J. F. McMillan, X. Yang, N. C. Panoiu, R. M. Osgood, and C. W. Wong. Enhanced Stimulated Raman Scattering in Slow-Light Photonic Crystal Waveguides. submitted, Nov 2005.

[13] S. M. Spillane, T. J. Kippenberg, and K. J. Vahala. Ultralow-threshold Raman Laser Using a Spherical Dielectric Microcavity. *Nature*, 415:621 – 623, Feb 2002.

[14] T. J. Kippenberg. *Nonlinear Optics in Ultra-high-Q Whispering Gallery Mode Microcavities*. PhD thesis, California Institute of Technology, May 2004.

[15] X. Yang and C. W. Wong. Design of Photonic Band Gap Nanocavities for Stimulated Raman Amplification and Lasing in Monolithic Silicon. *Opt. Express*, 13:4723–4730, 2005.

[16] H. Altug and J. Vučković. Two-dimensional Coupled Photonic Crystal Resonator Arrays. *Applied Physics Letters*, 84:161–163, 2004.

[17] H. Altug and J. Vučković. Experimental Demonstration of the Low Group Velocity of Light in Two-dimensional Coupled Photonic Crystal Microcavity Arrays. *Applied Physics Letters*, 86(111102), 2005.

[18] H. Altug and J. Vučković. Polarization Control and Sensing with Two-dimensional Coupled Photonic Crystal Microcavity Arrays. *Optics Letters*, 30:982–984, 2005.

[19] H. Altug and J. Vučković. Photonic Crystal Nanocavity Array Laser. *Optics express*, 13(22), October 2005.

[20] A. Yariv. *Quantum Electronics*. J. Wiley & Sons, Inc., 3 edition, 1988.

[21] J. Vučković. Advanced Topics in Optics and Quantum Optics - Optical Microcavities. Lecture slides, Lecture EE340, Stanford University, 2005.

[22] R. Claps, V. Raghunathan, D. Dimitropoulos, and B. Jalali. *Raman Emission in Silicon Waveguides: Prospects for a Silicon Amplifier and Laser.*, page 2211. Washington, DC, USA : Optical Soc. of America, 2003.

[23] J. D. Jackson. *Classical Electrodynamics*. J. Wiley & Sons, Inc., 3 edition, 2001.

[24] J. Vučković. Advanced Topics in Optics and Quantum Optics - Optical Microcavities. Lecture notes, Lecture EE340, Stanford University, 2005.

[25] S. G. Johnson and J. D. Joannopoulos. Introduction to Photonic Crystals. Unpublished supplementary material, MIT, 2003.

[26] J. D. Joannopoulos, R. D. Meade, and J. N Winn. *Photonic Crystals - Molding the Flow of Light*. Princeton University Press, 1 edition, 1995.

[27] S. G. Johnson. Photonic Crystals: Periodic Surprises in Electromagnetism. Lecture notes, MIT, May 2004.

[28] S. G. Johnson, M. Ibanescu, M. A. Skorobogatiy, O. Weisberg, J. D. Joannopoulos, and Y. Fink. Perturbation Theory for Maxwell's Equations with Shifting Material Boundaries. *Physical Review E*, 65(066611), June 2002.

[29] D. Englund, I. Fushman, and J. Vučković. General Recipe for Designing Photonic Crystal Cavities. *Optics Express*, 13(16):5961–5975, Jul 2005.

[30] FDTD. Wikipedia, the Free Encyclopedia. Retrieved November 20, 2005, from http://en.wikipedia.org/wiki/FDTD,.

[31] K.S. Yee. Numerical Solution of Initial Boundary Value Problems Involving Maxwell's Equations in Isotropic Media. *IEEE Transactions on Antennas and Propagation*, 14(3):302 – 307, 1966.

[32] A. Taflove and S. C. Hagness. *Computational Electrodynamics: The Finite-Difference Time-Domain Method*. Artech House, Inc., 3 edition, 2005.

[33] J. P. Berenger. A Perfectly Matched Layer for the Absorption of Electromagnetic Waves. *Journal of Computational Physics*, 114:185 – 200, 1994.

[34] S. Ramo, J. R. Whinnery, and T. van Duzer. *Fields and Waves in Communication Electronics*. Wiley, 3 edition, 1994.

[35] J. Vučković, M. Lončar, H. Mabuchi, and A. Scherer. Optimization of the Q Factor in Photonic Crystal Microcavities. *IEEE Journal of Quantum Electronics*, 38(7):850–856, July 2002.

[36] G. W. Burr. FDTD as a Nanophotonics Design Optimization Tool. *International Symposium on Photonic and Electromagnetic Crystals*, Poster P-Mo49, March 2004.

[37] W. Schroeder. *The Visualization Toolkit*. Kitware Inc., 3 edition, 2004.

[38] U. Kiecke. *Signale und Systeme*. Oldenbourg-Verlag, 3 edition, 2005.

[39] H.-Y. Ryu, S.-H. Kim, H.-G. Park, J.-K. Hwang, and Y.-H. Lee. Square-lattice Photonic Band-gap Single-cell Laser Operating in the Lowest-order Whispering Gallery Mode. *Applied Physics Letters*, 80(21):3883–3885, May 2002.

[40] J. F. Holzmann and P. Strasser and R. Wüest and D. Erni and H. Jäckel. Picosecond Free-carrier Recombinations in Indium Phosphide Photonic Crystals. In *17th International Conference on Indium Phosphide and Related Materials*, number TuP-24, Glasgow, Scotland, May 2005.

[41] Ioffe Physico-Technical Institute. New Semiconductor Materials: Characteristics and Properties. Retrieved November 30, 2005, from http://www.ioffe.rssi.ru/SVA/NSM/.